

# Report on the groundwater and transport flow model application to the to the Italian field site

Deliverable D\_3.4.3

Contributing partners:

LP – UNIPD DICEA

PP1 – CNR IGG

## TABLE OF CONTENTS

<b>1. INTRODUCTION</b>	<b>3</b>
<b>2. CONCEPTUAL MODEL</b>	<b>4</b>
2.1 Study area	4
2.2 Hydro-stratigraphic model of the pilot area	6
2.3 Groundwater dynamics model of the pilot area	9
2.4 Sedimentological constraints to the fresh-saltwater dynamics in the phreatic aquifer	15
2.5 Conclusive remarks	20
2.6 References	21
<b>3. APPENDIX: THREE-DIMENSIONAL FINITE ELEMENT MODEL</b>	<b>22</b>

## 1. INTRODUCTION

MoST 3.4 Action (Numerical Modelling), which is part of the WP 3 (Studying), aims to develop groundwater models for the computation of the saltwater evolution and the simulation of measures specifically planned for the mitigation of the salinization.

This report consists in the project deliverable “Report on the groundwater and transport flow model application to the to the Italian field site” (D\_3.4.3). The deliverable is composed of two main sections: the first one is focused to develop the conceptual model of the study site, the second provides all the activities carried out to develop, set-up and run a numerical three-dimensional density-dependent groundwater flow and salt transport model for the study area. All the activities and outcomes related to the second part has been collected is a MSc thesis in Environmental Engineering developed at the University of Padova.

## 2. CONCEPTUAL MODEL

Data interpretation of the salinity degree of the waters was based on the Electrical Conductivity (EC) and the limit between freshwater and saltwater values is in relation to tolerance bounds for crop growth and irrigation practice. Specifically, the following classification of the water was used in order to allow a comparison between past and new measurements (Carbognin and Tosi (2003).

- 1) Salty: EC exceeds 5 mS/cm;
- 2) Brackish: EC ranges between 2 and 5mS/cm with salt concentration higher than 1 g/L;
- 3) Fresh: EC is less than 2 mS/cm and the water is suitable for irrigation purposes.

Also the electrical resistivity measured by geophysical methods (vertical electrical sounding, electrical tomography, airborne electromagnetic, etc.) we used for detecting the presence of fresh- and saltwater in the subsoil assuming electrical resistivity  $<5 \Omega \cdot m$  and  $>10 \Omega \cdot m$  as the upper value for saltwater and the lower value for freshwater, respectively (Carbognin and Tosi, 2003; de Franco et al., 2009; Teatini et al., 2011).

New insights on the influence of the stratigraphic architecture on the fresh-saltwater dynamics, especially in the phreatic aquifer, have been obtained through the comparison between sedimentological sections (DOC n. MoST-CNR 3.2-005) and the EC log recorded in the monitoring network (DOC n. MoST-CNR 3.1-010) during the course of the project.

### 2.1 Study area

The study area encompasses the territory between the southern Venice lagoon margin and the final part of the Adige River. Specifically, the pilot test area is located in a low-lying farmland just south of the Brenta and Bacchiglione rivers (Fig. 1).



*Fig. 1 - Location of the MoST pilot site.*

Over the historical time, river diversions, channeling, and land reclamation progressively changed the hydraulic setting of the study area, and, presently, most of this coastal plain sector lays up to 3 m below the mean sea level (e.g., Gasparetto-Stori et al., 2012). Therefore, a complex network of ditches and pumping stations, that discharge the drainage water into the Venice Lagoon or the Adriatic Sea, regulates the depth of the water table.

The artificially controlled groundwater and surface water flows combined with sea level rise and land subsidence have enhanced the saltwater intrusion and the related soil salinization with serious environmental and socio-economic consequences (Carbognin et al., 2006). In particular, saltwater intrusion threatens drinking water quality, enhances the risk of soil desertification, compromises the agricultural practices, and decreases freshwater storage capacity (Carbognin and Tosi, 2003).

Understanding saltwater intrusion in the aquifer system and agricultural soil in this peculiar transitional coastal environment is a challenge, since it is characterized by (1) very high heterogeneity of the subsoil and (2) surface water - groundwater interaction anthropogenically controlled.

## 2.2 Hydro-stratigraphic model of the pilot area

In the pilot area, the subsoil is formed by alternating sandy-silty, clayey-silty and clayey layers of sediments representing alluvial, lagoon, deltaic, and littoral units (Tosi et al., 2007). The representative hydro-stratigraphic setting is shown in Fig. 2).

Three main aquifers are present down to 50 m:

- phreatic aquifer (A1) in the shallower 9-14 m thick unit,
- locally-confined aquifer (A2) between 18 and 38 m depth,
- confined aquifer (A3) down to the bottom.

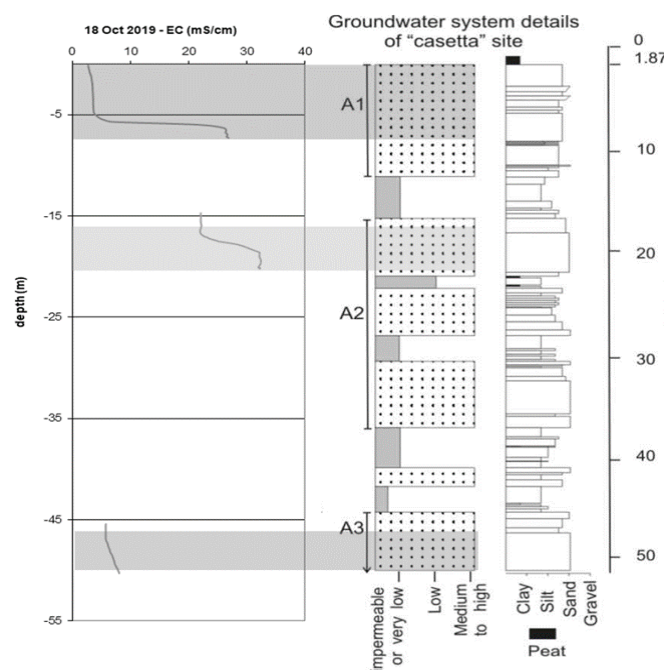


Fig. 2 - Hydro-stratigraphic setting of the pilot test area.

Aquifer A1 is mainly developed in sandy littoral deposits locally presenting at the top sandy paleo-channel bodies, where thin lenses of fresh- to brackish- waters are present, with variable extent depending on their recharge. The presence of an over-consolidated clay between 14 and 18 m depth, i.e. the Caranto paleosoil (Donnici et al., 2011), exhibits an important hydrogeologic function and often precludes the downward propagation of seawaters. Hence, the salinity degree generally reduces below 20 m depth, at least in some portions of the study area, even if brackish waters are present also below 50 m depth.

The hydro-stratigraphic setting is variable because of the deepening of the geological units in the SE direction and the presence of buried geomorphological structures, which occur locally, characterized by high variability in the grain size.

Fig. 3 shows the model of the hydro-stratigraphic setting of the pilot area, highlighting the variability of lithology, permeability and salinity.

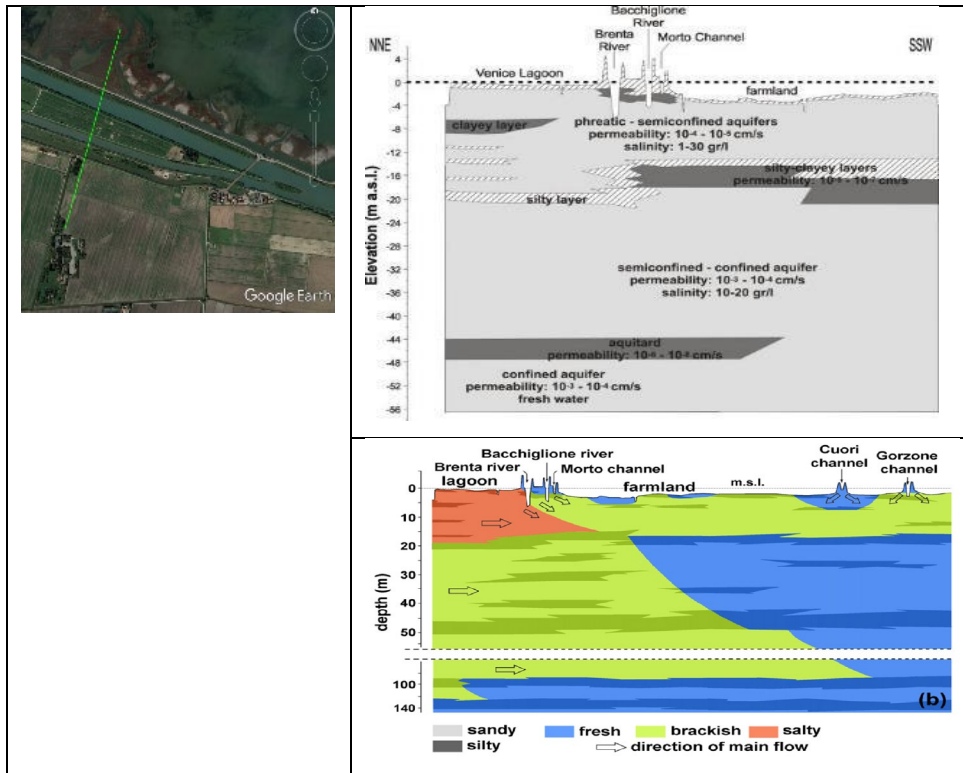


Fig. 3 - Conceptualization of the hydro-stratigraphic setting of the Italian pilot area. Range of permeability and salinity and main water flow direction in the subsoil layers is also shown.

Exchanges between lagoon water and groundwater are shown in (Fig. 3). Groundwater moves preferentially from the lagoon sub-bottom towards the farmland because of (i) the higher density of the saltwater, (ii) the inland piezometric head lower than the surface water level, due to a land elevation well below the mean sea level and (iii) a widespread use of pumping stations to keep low-lying lands drained.

The pilot test area is characterized by seasonally and short-term saltwater fluctuations. Seasonally, i.e. saltwater front intrudes landward during the autumn–winter season and moves back seaward in spring–summer (de Franco et al., 2009). Water quality is significantly improved by local rainfalls that rapidly supply freshwater, which is then stored in sandy paleo-ridge systems. Indeed, the latter ones

are capable of containing groundwater with lower salinity than that occurring in the lateral silty deposits, at least in the shallow part.

Important recharge factors are the fresh-water releases for irrigation purposes and riverbed seepage. The latter is influenced by the tide dynamics, which, together with river discharge, control the seawater encroachment along the river mouths.

Focusing on the pilot site where mitigation measure through a sub-irrigations pipe was planned and considering only the shallower units, which is the target of the MoST project, a more detailed hydro-stratigraphic model was obtained combining the analysis of the sediment cores and the EC profiles. The hydrogeological model is sketched along a roughly NNE-SSW section crossing the pilot test site selected for the implementation of the mitigation measure to reduce salinity in the farmland (Fig. 4).



*Fig. 4 - Position of wells used for sketching the hydro-stratigraphic model of the pilot site used for testing mitigation measures.*

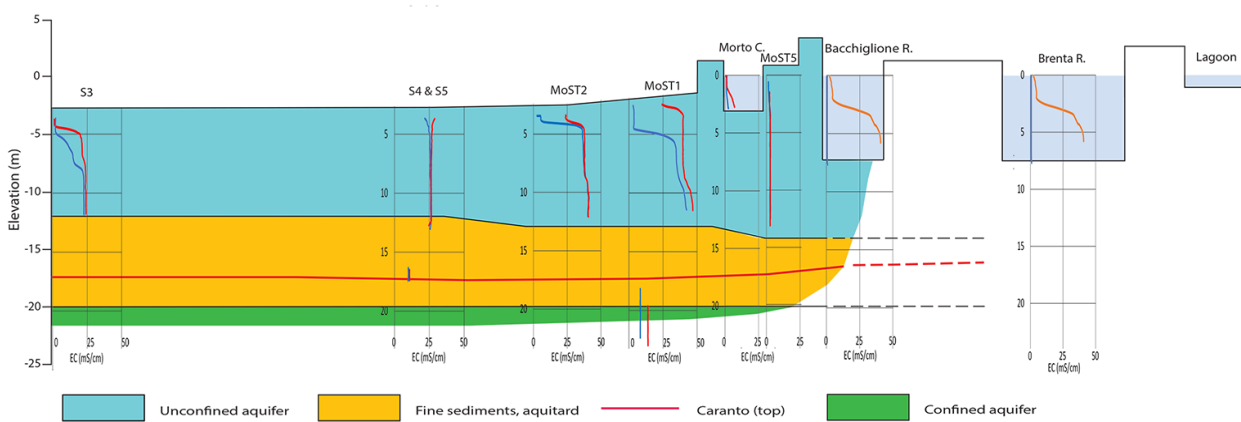
Along this section the subsoil is formed by three main units, in turn corresponding to: the phreatic aquifer, composed by sandy deposits, including the paleo-channel system, the aquitard, mostly formed by silty sand and silty clay layers, including the caranto paleo-soil, and the confined aquifer, composed by Pleistocene alluvial deposits. The over-consolidated clay known as caranto lies at about 17 m below msl. This is the uppermost Pleistocene alluvial sedimentation and, above it, the Holocene units are formed by marine-lagoon and back barrier deposits.

EC vertical profiles recorded along the same cross section show a high spatial variability of the saltwater presence in the shallow aquifer system A1 (0-8 m) while it is almost similar in the confined



aquifer A2 (15-20 m) (Fig. 5). The phreatic is generally highly salty contaminated with background values of EC spanning from 20 to 50 mS/cm, despite brackish water is discontinuously present in the shallower parts. Specifically, fresh-brackish water occurs in the sandy paleo-channel systems when it is recharged by rainfalls and seepage from the Morto Channel. Lower salinity affects the confined aquifer and EC is around 12 mS/cm.

Although the continuity of the sandy geomorphological body toward the lagoon basin is not yet proved, on the basis of the water levels of the Morto channel, Bacchiglione and Brenta rivers, the subsoil setting and the ground elevation of the farmlands and riverbeds, the aquifer contained in the sandy body is expected to be influenced by the watercourses.



*Fig. 5 - Hydro-stratigraphic sketch along a NNE-SSW direction in the pilot test site. See Fig. 4 for the location of the section EC profiles show approximately maximum and minimum values recorded in the wells, Morto Channel, Bacchiglione River and Brenta River.*

### 2.3 Groundwater dynamics model of the pilot area

The analysis of the continuous logged time series of piezometers allowed a detailed description of the behavior of the shallow groundwater dynamics during summer and fall seasons. Indeed, by combining data simultaneously recorded in piezometers, watercourses and sea, together with precipitations, the surface water – groundwater exchanges have been dynamically highlighted.

The water table of the phreatic aquifer decreases southwards and from north to south with a difference of about 1 m, which is approximately the same difference in the ground elevation of the farmlands. The aquifer shows background values of EC decreasing southward from 38 to 28 mS cm<sup>-1</sup> at the top

and from 40 to 33 mS cm<sup>-1</sup> at the bottom, according to the increasing distance from the lagoon. In dry conditions, a clear EC stratification is shown only in the site MoST3, while it is quite homogeneous in MoST1b and MoST2 (Fig. 6).

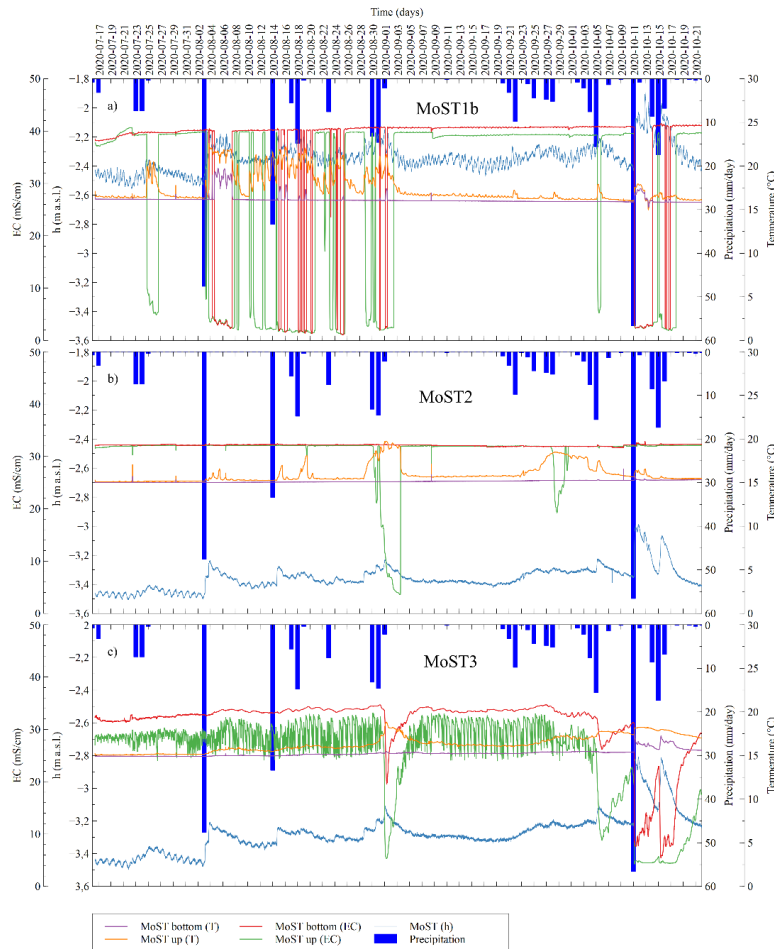


Fig. 6 - Time series recorded from July 2020 to October 2021 in piezometers MoST1b, MoST2 and MoST3. The parameters recorded are: temperature, EC and water level at the top and at the bottom of each well. The precipitation recorded at Sant'Anna meteorological station is also reported.

The collected data are related to the occurrence, often simultaneous, of several forcing factors such as atmospheric precipitations, tide encroachment and water management from pumping station all contributing to the complexity of the system response (Fig. 7).

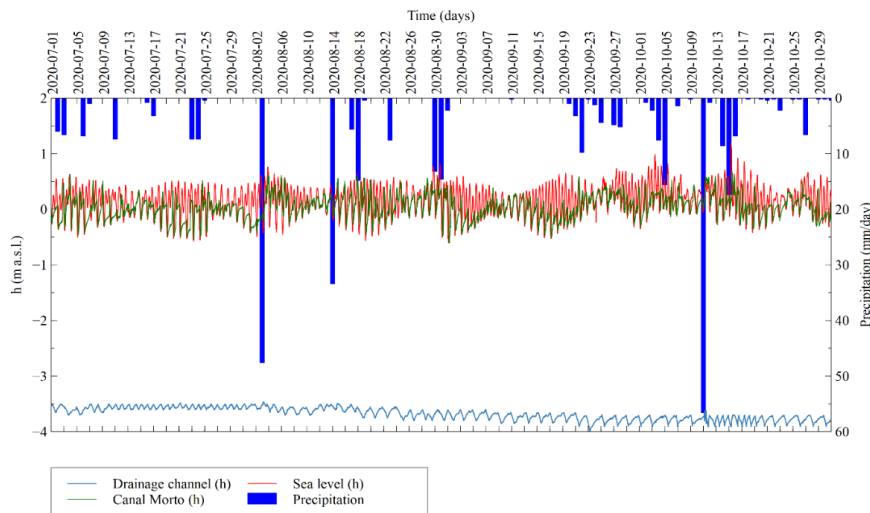


Fig. 7- Time series from July 2020 to October 2021 of Drainage channel level, Canal Morto layer, and Sea Level. The precipitation recorded at the Sant’anna meteorological station is also reported.

Cross-correlation analyses carried out on EC and water level of the 3 wells in respect of the levels of Canal Morto, the sea and the pumping station, supports the following conclusions, synthesized in the graphic model of Fig. 8 (Lovrinović et al. 2021).

Major water table rises are concomitant to precipitations, which lead to significant EC decreases in the uppermost layer and sometimes in the whole aquifer thickness. The heavier the events the longer the decrease in groundwater EC, also with the contribution of the freshwater dispersions from the Brenta and Bacchiglione riverbeds. The increase of water table during rainfall events is generally rapid, often instantaneous, while the decrease in EC is differentiated from the northern and the southern sides of the studied area. The return to the normal conditions is generally quick in the northern part of the aquifer and slower in the southern ones ( Fig. 6 and Fig. 8).

EC and h values in the northern sector (MoST1b) are clearly driven by the tide at sea (in phase and delayed, 3 hours and 4 hours 40 minutes, respectively, with respect to the tidal signal), while they do not show significant correlation in the southern sector (MoST2 and MoST3 sites), at least for short-term intervals (daily). This different behavior between the northern and the southern part of the aquifer should be explained taking in consideration their distance from the Venice lagoon and the Brenta and Bacchiglione rivers, whose terminal section, next to the river mouths, could be easily affected by salt wedge.

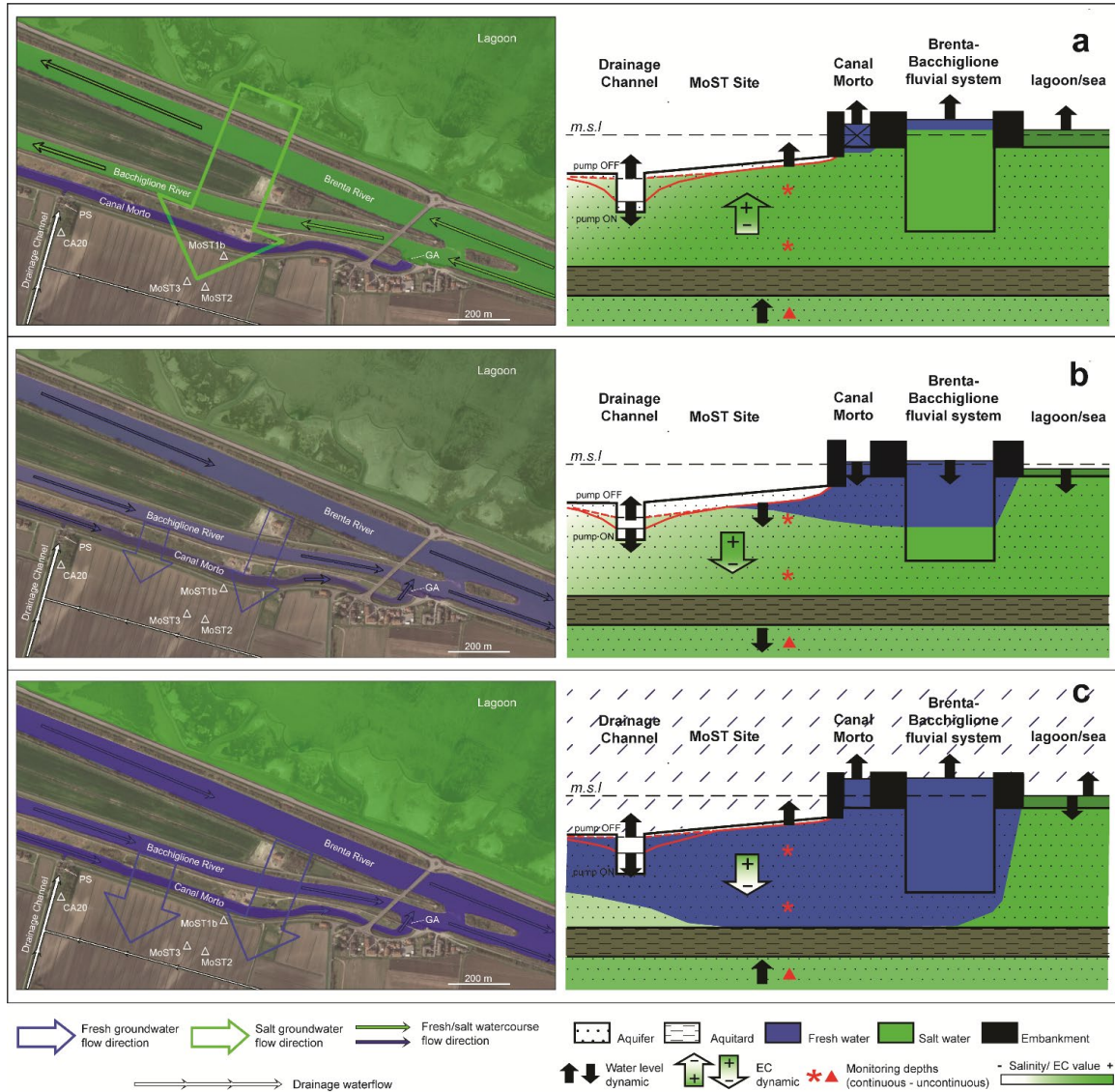


Fig. 8 - Schematic representation of the saltwater intrusion and fresh water pathways, obtained over the monitoring period July - October 2020, in three different scenarios: (a) dry periods with high tide and Morto Channel (MC) gate closed; (b) dry periods with low tide and Morto Channel (MC) gate opened and (c) wet periods with heavy precipitations (regardless of high or low tide and gate closed or opened).

A correlation between the  $h$  of the aquifer and the water level of the Morto Channel has been observed. The  $h$  value is in phase with no delay next to the watercourse and in phase (4 hours delay) in the farthest sector. The EC values in the aquifer correlate in phase with 4h early with the Morto Channel water level both in the north and south sites (MoST1b, MoST2 and MoST3). This

support that mobile gates prevent the seawater from entering the Morto Channel just at the beginning of the tidal rise.

The drainage channel levels (pumping station inflow) drives the phreatic aquifer levels in MoST2, while at MoST1b and MoST3 the aquifer anticipates in phase the water level of the drainage channel respect to the aquifer level but shows different behaviors. Specifically, the results of cross correlation analysis indicate that the drainage channel reaches maximum values after 8 hours 20 minutes of the maximum h in the northern site (aquifer drives the drainage). Conversely, the drainage channel levels anticipate in phase h of about 3 hours 40 minutes at MoST2 (drainage drives the aquifer). At the MoST3 site the h changes in phase with the drainage channel level and exhibits a max correlation with 2 hours 20 minutes early (aquifer drives drainage). The time difference between north and south sectors is related to the distance between the piezometers and the drainage channel. The Drainage Channel level is inversely correlated with the EC in the aquifer. In the northern site (MoST1b site), the EC lead the channel level but maximum correlation is not reached within 12 hours. In the south the correlation shows different behavior, at MoST2 site EC is 4 hours 30 minutes delayed and at MoST3 site EC is 10 hours in advance. This is quite surprising, given the proximity of the two sites; we hypothesize that such difference is likely depending on the local variability of the subsoil architecture. Therefore, the pumping station drives the phreatic aquifer levels in MoST2, while at MoST1b and MoST3 sites the driver is the aquifer. The lowering of the drainage level, by the operation of the pumping station causes an increase of the EC in the aquifer with different timing.

The EC changes in the aquifer during the examined dry period, even though in the range of a few mS cm<sup>-1</sup>, are significant. Being approximately with the same delay of the tide, it is reasonable to suppose that increasing EC values are influenced by the seawater intrusion from the lagoon basin and from the seawater encroachment along the Brenta and Bacchiglione rivers. Decreasing values, vice versa, are driven by the leakages from the watercourse beds when freshwater replaces the marine water towards the mouth at low tide. The contribution from the Morto Channel is excluded, or at least negligible and limited to the proximity of the embankment in the very shallow subsoil. The regulation gates at the Morto Channel mouth contrast the seawater propagation along the channel, maintaining freshwater in the upstream sections. During the closure of the gates, the water level in the Morto Channel rises, because of the fresh water accumulation upstream, but slower than the tide. After the opening of the gates, the levels of Morto Channel decreases following tide with almost the same timing. The leakage from the Morto Channel bed seems negligible as it should be of freshwater and

the EC of the aquifer does not show any significant decrease when the regulation gates are closed. The  $h$  and EC in the northern part of the aquifer (MoST1b) are not directly linked with levels of the Morto Channel, despite the significant cross correlation. When EC rises there is the concurrence of the following events: tidal rising and saltwater accumulation in the aquifer, GA closure and freshwater accumulation in CM. When tide lowers and gates open, EC decreases because of the Brenta – Bacchiglione system leaks freshwater in the aquifer. Hence, the groundwater freshening is definitely not due to the influence of the Morto Channel.

In conclusion, the EC background of the phreatic aquifer is given by the seawater intrusion from the lagoon and the river mouths and is modulated by the exchanges with Brenta and Bacchiglione river beds especially during the ebb tide phase, while the leakage from Morto Channel is negligible.

Regarding the shallow confined aquifer, daily and fortnightly periods of sea level changes control the groundwater level, while they do not affect the salinity. Daily changes of aquifer pressure are in phase with the tidal cycle exhibiting a delay of 2 hours 30 minutes. Maximum pressure generally occurs during spring tides (syzygy). Piezometer CA20 also follows in counterphase the level of the Drainage Channel with a delay of 6 hours 20 minutes (cross correlation equals to 0.51). Regarding the precipitation and  $h$  changes relationship, local precipitation leads the rise of the groundwater level with maximum correlation in the same day, despite significant correlation up to the previous 5-6 days occurs. This suggests that the recharge zone of this aquifer is not far from the study area and in the order of 10 km.

In conclusion, the groundwater dynamics of the phreatic and confined aquifers can be summarized in the following.

- a) Dry periods with high tide and gate closed: the salt-water flow from the lagoon and through the river mouths into the aquifers; the water levels of the rivers and of the aquifers rises. The Canal Morto water, due to the activation of the gates, rest fresh, but the leakage is negligible.
- b) Dry periods with low tide and gate opened: Brenta and Bacchiglione rivers fresh-water leakages into the aquifer, mitigating the salinity of the north-easternmost sector of the test area. Water table of the rivers and of the aquifers decreases.
- c) Wet periods with intense precipitations (high/low tide; gate opened/closed): Intense precipitations lead to significant EC decreases in the uppermost layer and sometimes in the whole aquifer thickness, but the mitigation dos not lasted more than few days. The confined aquifer is not influenced by precipitation. Water table of rivers and aquifers rises.

#### *2.4 Sedimentological constraints to the fresh-saltwater dynamics in the phreatic aquifer*

During the course of the project, numerous EC water profiles were acquired from wells of the MoST monitoring network located at the Chioggia pilot site. The monthly cadence of the measurements allowed to describe the relationships between fresh and salt water in the groundwater aquifer in the various seasons and hydrological conditions since 2020. Analysis of the EC data, assumed as representative of the groundwater salinity, well revealed similarities and differences in the behaviour of freshwater-saltwater density stratification in different wells of the groundwater aquifer under similar hydrologic conditions. This observation revealed the need to test for the presence of other factors driving these behaviours, which seems to be unrelated to weather-climate events and the hydraulic regime imposed by drainage. Therefore, the stratigraphic data obtained from the sedimentological analysis of the sedimentary cores sampled during the installation of the wells were carefully reviewed in order to highlight the presence of subsoil structures capable of influencing the stratification of fresh-salt water, generally controlled by differences in water density in groundwater. Specifically, these structures should correspond to stratigraphic-lithological discontinuities that give the aquifer differences in permeability without entailing the confinement of the aquifer itself. For instance, the presence of fine-grained layers (i.e. less permeable) inside a sandy aquifer could keep separate less dense water (i.e. fresher water) in the upper part, leading the formation of surficial fresher water lenses. These sedimentological structures that constrain the fresh-saltwater dynamics in the phreatic aquifers have been recognized for each site through the comparison between EC vertical profiles and stratigraphic sections. As explained in the previous chapter, the aquifer of the study area is highly salinized. The saltwater laterally flowed from the lagoon into the aquifer. Fresh water, coming from lateral leakages or from precipitation events, mitigates the aquifer.

Representative EC profiles, selected from the dataset recorded between summer 2020 and winter 2021, were chosen to represent the worst, better and intermediate conditions, in terms of saltwater contamination of the aquifer. The depths of the major changes in EC values, including the freshwater-saltwater interface, have been compared with those of the stratigraphic discontinuities observed in the subsoil (reported in the stratigraphic section on the right of each figure).

In MoST1 and MoST2 wells (Fig. 9a,b) the stratigraphic architecture of the surficial aquifer shows a major discontinuity at about 4 m below msl, where a fine-grained layer of silty clay separates the surficial lenticular sand body, in green colour (see Doc MoST-CNR 3.2-005), from the littoral aquifer,

in yellow. At around 8 m below msl another discontinuity is present inside the sandy littoral aquifer, presenting fine-grained layers of silt and peaty clay.

The EC vertical profiles recorded in these wells present a strong vertical variation between 4 and 45 mS/cm. The major variation is located at 4 m below msl, in correspondence of the main stratigraphic discontinuity: at this level the EC rapidly increases with a sharp change. Another small variation in the EC is shown at about 8 m, in correspondence of the silt layer inside the littoral sand (in yellow). In the other portion (i.e. where the stratigraphy is homogeneous) the EC profiles are vertical or slightly inclined, with the progressive increase of EC with depth.

Also in MoST3 (Fig. 9c) the major stratigraphic discontinuity, a fine-grained layer at about 5.5 m that separates the lenticular aquifer from the littoral one, corresponds to the major change in EC. In this case the EC values never goes below 17-20 mS/cm and the fresher water lens is not always present, possibly depending on the availability of surficial freshwater.

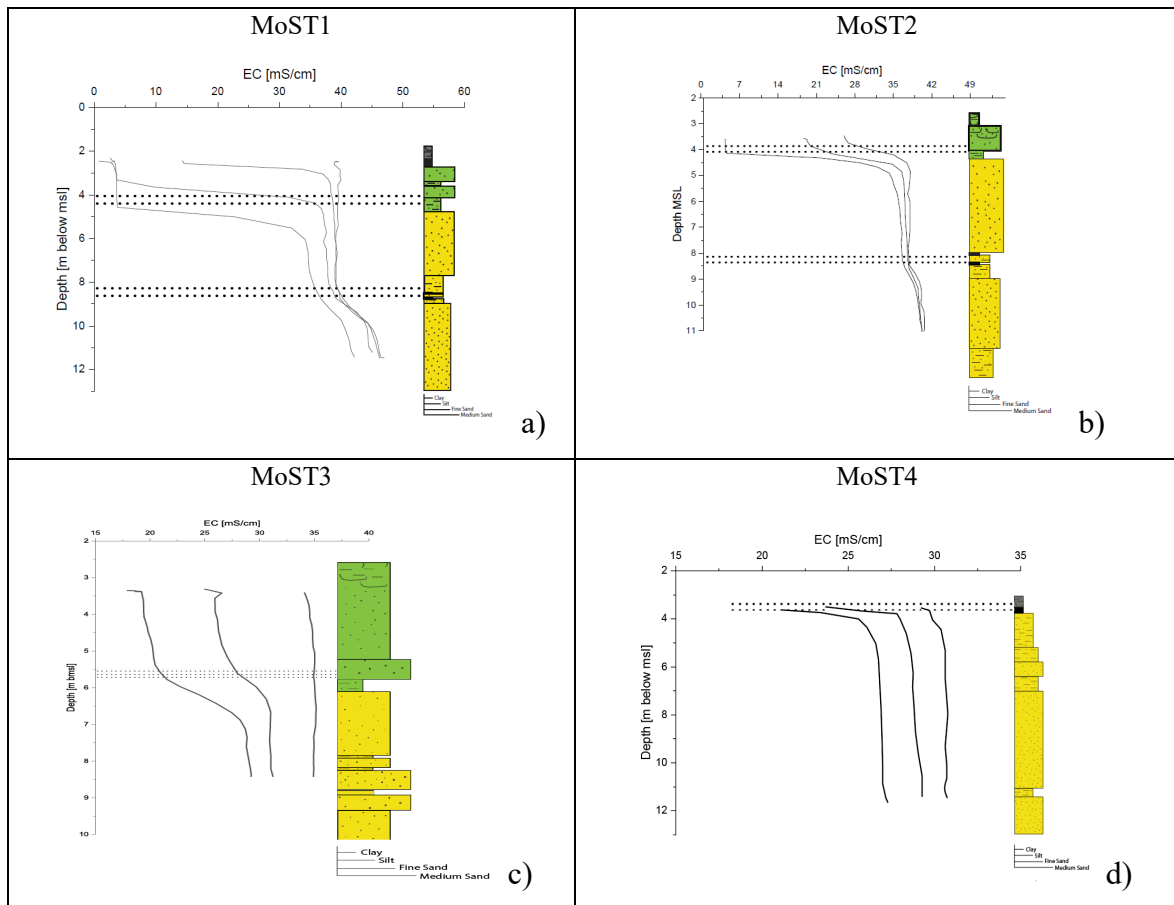
MoST4 (Fig. 9d) presents a quite homogeneous (sandy) stratigraphy, indeed, in this area the sandy lenticular surficial body is absent. The only stratigraphic discontinuity is at the top of the aquifer, where peat and clay layers are present. The EC profiles always show a variation, with an increase of 2-4 mS/cm, in correspondence of the surficial peat layer. Below this level the profiles are straight, presenting higher (around 30 mS/cm) or lower values (27 mS/cm) depending on the availability of fresh water.

MoST5 (Fig. 9e) is the only well located above msl, at the northern bank and very close to the fresh artificial drainage channel (Canal Morto). The stratigraphy is characterized by the presence of few surficial fine-grained meters, down to 3 m below msl, and the sandy littoral aquifer, presenting finer-grained layers at about 8.5 m. The EC profile of this well present very low values (1 to 2.5 mS/cm), probably due to the proximity of the Canal Morto fresh water. The peat layer at 2.5 m below msl seems to confine at the very top a fresher water lens. The lower part of the profiles is straight. The fine-grained layer at 8.5 m seems to not influence the water stratification, possibly because the EC values are quite homogeneous and too low to show remarkable variations in the water column.

In general, analyses of the various wells have shown that small sedimentological discontinuities, such as the presence of fine-grained layers, although not capable of confining the aquifer, significantly influences groundwater stratification by controlling the shape and location of the interface and the transition zone formed between freshwater and saltwater. Based on this information, and taking into account that the major freshwater recharge of the phreatic aquifer is related to the leakage from the



freshwater courses and precipitation events, a conceptual model showing how the stratigraphic architecture of the subsoil could modify the vertical profile of the EC, assumed as representative of the groundwater density (i.e. the salinity), has been sketched (Fig. 9f).



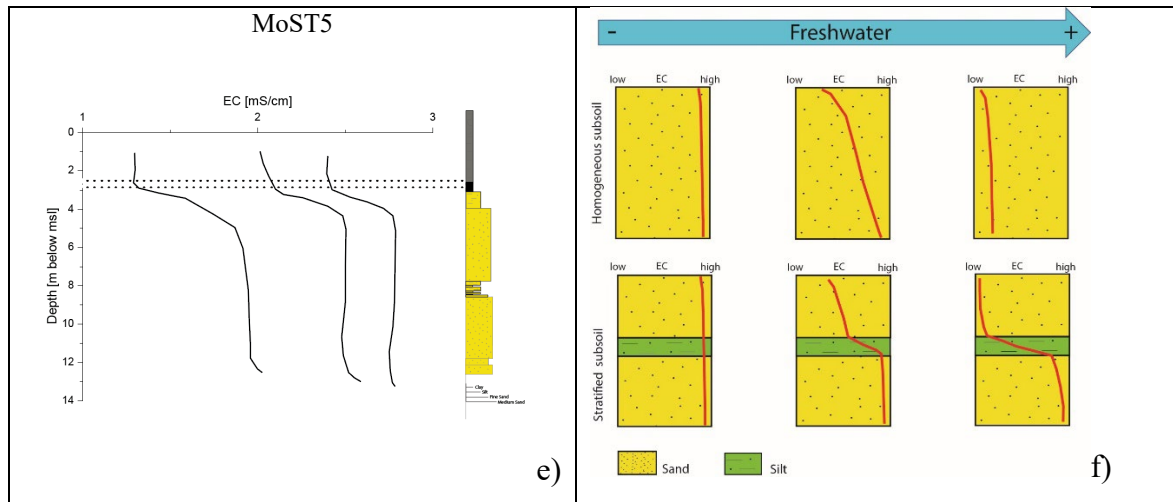


Fig. 9 – a-e) Vertical EC profiles and stratigraphic sections recorded in MoST1, MoST2, MoST3, MoST4, and MoST5 wells. The two dotted bands represent the major changes in salinity corresponding to sedimentological discontinuities. f) Conceptual model of the propagation of the mitigation signal in surficial aquifer characterized by homogeneous or stratified subsoil, respectively.

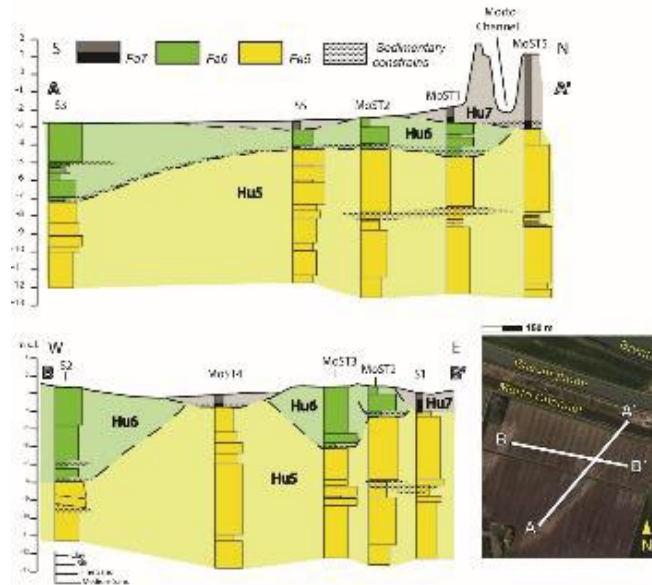
The model highlights that the EC profile shape (i.e. the groundwater stratification) can be strongly influenced by the presence of stratigraphic discontinuities. Two cases based on different stratigraphic setting are considered: a sandy homogeneous subsoil and a subsoil containing a silt layer interrupting the stratigraphy. Both cases have been conceptualized considering an increasing availability of freshwater. The model show how the EC curve varies between two end-members: no input (on the left) and large input of freshwater from the top of the aquifer.

In the case of homogeneous subsoil, almost constant values of EC depict vertical profiles under both negligible and high freshwater inputs. In between of these two extreme EC conditions, the progressive increase of freshwater in the uppermost part of the aquifer allows the formation of a transitional zone where the salinity gradually increases toward the bottom of the aquifer.

In the case of a stratified subsoil, a quite vertical EC profile is shaped (as in the case of the homogeneous subsoil) under high salinity condition and absence of freshwater in the upper part the aquifer. Conversely, the EC profile shows a sharp change in correspondence of the fine-grained layer when the freshwater input progressively increases in the upper part of the aquifer. The fine-grained layer acts as a sort of constraint of the groundwater salinity dynamics that delays the infiltration of freshwater into the deeper part of the aquifer. The freshening signal hardly propagates vertically,

passing through the fine (and less permeable layer), and expands preferentially laterally with the progressive increase in extension and freshness of the surficial lens.

Detailed analysis of the relationships between the vertical EC and stratigraphic profiles was carried out along two orthogonal sections crossing the study area (Fig. 10), one roughly perpendicular to the lagoon margin and the watercourses recharging the aquifer and one perpendicular to the buried geomorphological structures, respectively



*Fig. 10 – NS and WE stratigraphic sections of the upper portion of the subsoil of the study area, corresponding to the phreatic aquifer. In the sections the stratigraphic constrains are indicated by dotted polygons.*

. Summarizing, four setting where stratigraphic constraints occur were recognized:

- In correspondence to the clay layers at the base of Hu6. The presence of the channelized aquifers (MoSt1, MoSt2, S5, S3, S2) trigger the formation and the maintenance through time of fresher water lenses in the phreatic aquifer.
- Eventually if in Hu6 finer layers are present (S2, S3). Such event happens in the western channelized surficial sandbody (S2) and in the southern part of the eastern one (S3), where the Hu6 shows its major thickness.
- Inside the littoral aquifer Hu5, in the upper part, where coarser sand passes downward to finer one (S2), or around the middle portion of Hu5, where silty-clay layers often appear (S1, MoSt1, MoSt2)

- Often present at the base of Hu7 (very surficial stratigraphic constraints) in correspondence to peaty clay layers (MoST5, and MoST4), that could preserve fresher water at the very top of the phreatic aquifer.

We can assume the base of the channelized aquifer (Hu6) as the most important constraint to the groundwater dynamics of the study area. Indeed, the fine layer at the base of Hu6 always hosts fresher water lenses. The other layers could be regarded as secondary constraints that can be developed or not depending on the freshwater inputs in the aquifer.

### *2.5 Conclusive remarks*

The hydro-stratigraphic setting of the Italian pilot site geological investigated by hydrogeological and sedimentological analysis revealed the occurrence of a complex relationship between stratigraphic discontinuities and groundwater dynamics. Sedimentological constraints occurring in the unconfined aquifer significantly influence to the groundwater fresh-saltwater stratification. The constraints could be: peat layers at the base of Hu7, fine-grained layers inside Hu6 or at its base, the passage between finer and coarser sand in Hu3. The portion of the aquifer most influenced by freshwater availability is the north-central part, where a paleo-channel system (Hu6) is present, but with minor thickness in respect of the one existing at the westernmost and southernmost part of the area. This area, being the most sensitive to changes in freshwater inputs should be considered in the frame of eventual mitigation strategies.

Although this study represents a step forward in understanding the fresh-saltwater dynamics into the aquifers, we are aware that a number of uncertainties still need to be resolved by further investigations, especially to address optimal strategies for mitigation and water-management practices.

## 2.6 References

- Carbognin, L., Tosi, L., 2003. Il progetto ISES per l'analisi dei processi di intrusione salina e subsidenza nei territori meridionali delle province di Padova e Venezia. Istituto per lo Studio della Dinamica delle Grandi Masse - CNR, Grafiche Erredici Padova (Italy).
- Carbognin, L., Gambolati, G., Putti, M., Rizzetto, F., Teatini, P., Tosi, L., 2006. Soil contamination and land subsidence raise concern in the Venice watershed, Italy. *WIT Transactions on Ecology and the Environment* 99:691-700.
- de Franco, R., Biella, G., Tosi, L., Teatini, P., Lozej, A., Chiozzotto, B., Giada, M., Rizzetto, F., Claude, C., Mayer, A., Bassan, V., Gasparetto-Stori, G., 2009. Monitoring the saltwater intrusion by time lapse electrical resistivity tomography: The Chioggia test site (Venice Lagoon, Italy). *J. of Appl. Geophys.* 69(3-4):117-130.
- Donnici, S., Serandrei-Barbero, R., Bini, C., Bonardi, M., Lezziero, A., 2011. The Caranto Paleosol and its role in the early urbanization of Venice. *Geoarchaeology: An International Journal* 26(4):514-543.
- Lovrinović, I.; Bergamasco, A.; Srzić, V.; Cavallina, C.; Holjević, D.; Donnici, S.; Erceg, J.; Zaggia, L.; Tosi, L. (2021) Groundwater Monitoring Systems to Understand SeaWater Intrusion Dynamics in the Mediterranean: The Neretva Valley and the Southern Venice Coastal Aquifers Case Studies. *Water* 2021, 13, 561. <https://doi.org/10.3390/w13040561>
- Teatini, P., Tosi, L., Viezzoli, A., Baradello, L., Zecchin, M., Silvestri, S., 2011. Understanding the hydrogeology of the Venice Lagoon subsurface with airborne electromagnetics. *J. Hydrol.* 411(3-4):342-354.
- Tosi, L., Rizzetto, F., Bonardi, M., Donnici, S., Serandrei Barbero, R., Toffoletto, F., 2007. Note illustrative della Carta Geologica d'Italia alla scala 1: 50.000, Foglio 148-149 Chioggia-Malamocco, APAT, Dip. Difesa del Suolo, Servizio Geologico d'Italia, SystemCart, Roma, p. 164, 2 Maps.
- Tosi, L., Da Lio, C., Bergamasco, A., Cosma, M., Cavallina, C., Fasson, A., Viezzoli, A., Zaggia, L., Donnici, S., 2002, Sensitivity, Hazard, and Vulnerability of Farmlands to Saltwater Intrusion in Low-Lying Coastal Areas of Venice, Italy. *Water*, 14, 64. <https://doi.org/10.3390/w14010064>

### **3. APPENDIX: THREE-DIMENSIONAL FINITE ELEMENT MODEL**

The appendix provides the text of the MSc thesis developed at UNIPD focused on the development and application of a three-dimensional density-dependent finite element model for the simulation of the groundwater flow a salt transport in the Venice study site

# Chapter 1

## Saltwater intrusion in coastal aquifers

---

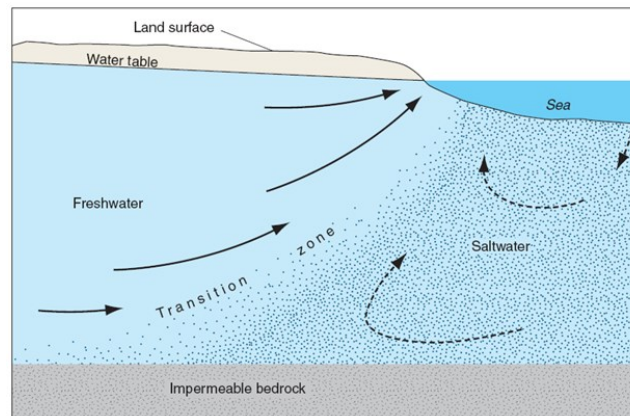
### 1.1 Seawater intrusion

Seawater intrusion in coastal aquifers is one of the most challenging and worldwide environmental problems. It is a natural phenomenon severely worsened by anthropogenic factors, due to coastal urbanization and human activities (such as the excessive pumping of groundwater for drinking water supply and irrigation, land subsidence, sea level rise, and climate change) which contribute to the reduction of natural recharge (White and Kaplan, 2017).

Demands from aquifers for irrigational purposes are about 70% of world's freshwater usage. In areas of limited surface water availability like coastal zones, groundwater resources are essential since they are the primary or sole freshwater sources for drinking, domestic, irrigation and industrial uses. Since more than 60% of the global population lives within 100 km of coastlines (and this percentage is predicted to further increase in the following decades), most part of water demand is taken from coastal aquifers. Furthermore, with global warming and sea level rise, many coastal regions may be affected by enhanced coastal erosion, coastal barrier breaching, coastal flooding due to extreme storm surges and tropical storms and subsequent seawater intrusion into fresh groundwater systems (Elsayed and Oumeraci, 2018).

Coastal areas and aquifers turn out to be very sensitive environments and saline intrusion has become the main restriction for groundwater exploitation in many coastal aquifers (Rorai, 2007). Groundwater withdrawal from a coastal aquifer can disrupt the natural equilibrium between freshwater and seawater, resulting in a landward movement of saltwater. Marine saltwater is denser than continental freshwater, mainly due to salinity differences. Therefore, in stable conditions the freshwater floats on the saltwater whereas the saltwater exerts a higher hydrostatic pressure and intrudes inland below the freshwater, creating a salt groundwater body lying on the aquifer bottom called "salt wedge". As shown in Figure 1.1, freshwater discharges into the sea and in the deeper part seawater moves inland. The freshwater thickness decreases from the wedge toe towards the sea. Among these two defined flow patterns, there is a not well-defined transition zone, called mixing or

brackish zone and its shape, extent and position depend on many factors like hydraulic properties of the aquifer and variations of tides and recharge. A circulation of saltwater from the sea to the transition zone and then back to the sea is induced by mixing of freshwater and seawater in the mixing zone. If the mixing zone is thin compared to the aquifer thickness (representing only a few percent of the



*Figure 1.1 Groundwater flow patterns and the transition zone in a simplified coastal aquifer (after Barlow, 2003).*

saturated thickness), it can be assumed as a sharp interface between the two fluids (Custodio and Bruggeman, 1987). The rate and degree of seawater intrusion is ruled by different parameters, including aquifer thickness, permeability, variations in the hydrological cycle processes such as precipitation and evapotranspiration and the quality and quantity of inflows and outflows (Hussain et al., 2019). The excessive exploitation of coastal aquifers causes a cone of depression which can determine a displacement of the mixing zone with a consequent increase of the saltwater wedge extent.

Seawater intrusion is a threat to the quality and sustainability of fresh groundwater resources in coastal aquifers. Saline water is the most common pollutant in fresh groundwater which can also compromise the agriculture and the economy of the affected regions. A salt concentration equal to 2-3% can make freshwater unusable for domestic purposes, whereas a concentration of 5% is too high for irrigational uses for many crops (Rorai, 2007). Moreover, remediation of brackish or saline groundwater with biological, chemical, and physical techniques is a very expensive process and can take a long time, depending on the source and level of salinity (Hussain et al., 2019).

Therefore, the problem of saline intrusion along the land-sea border requires a better understanding of the flow dynamics in coastal aquifers. This can allow a more sustainable groundwater management and the development of engineering solutions to mitigate or prevent saltwater contamination threatening ecosystems, water supplies and coastal infrastructure.



## 1.2 Examples of saltwater intrusion sites around the world

In Asia, India is one of the most affected countries by seawater intrusion with a coastline of 7500 km (Figure 1.2). Coastal freshwater resources are increasingly stressed due to population growth and rapid industrialization leading to water scarcity issues and seawater intrusion into coastal aquifers.

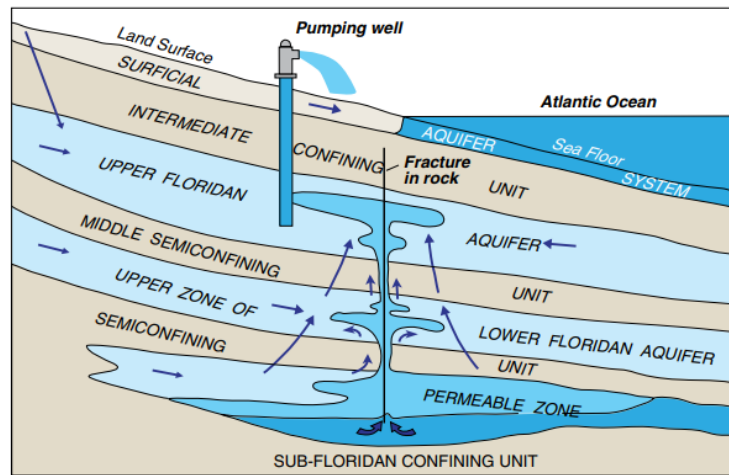
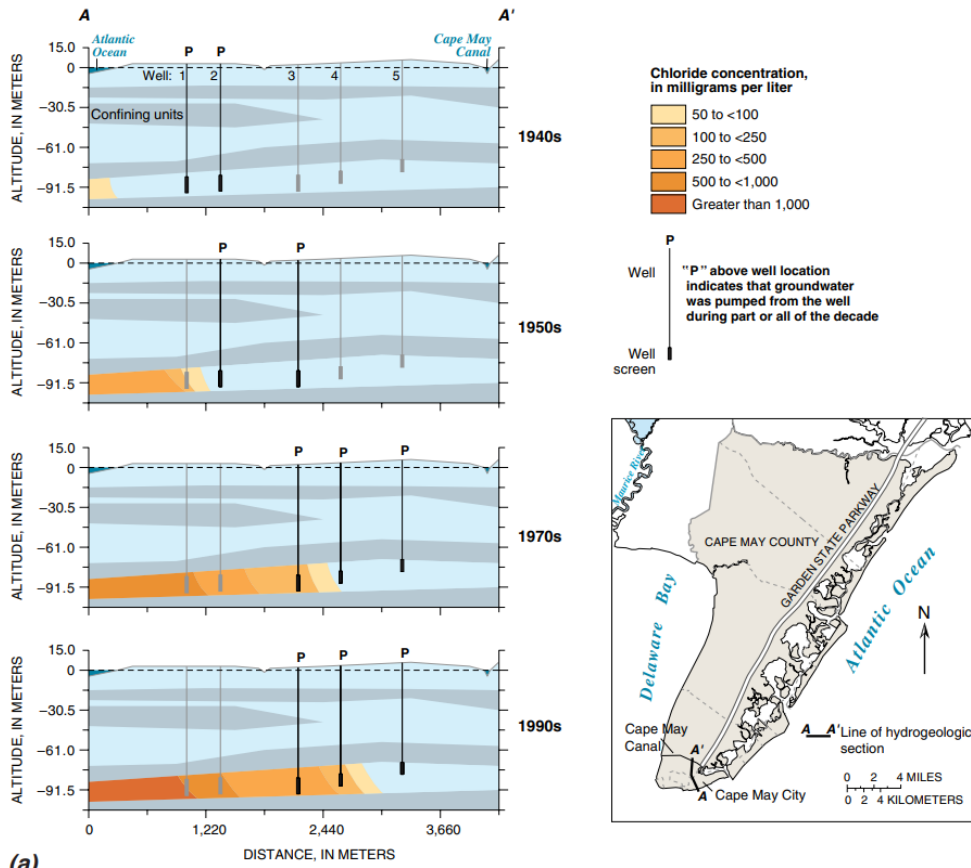


*Figure 1.2 Districts of India (in blue) under the direct influence of seawater (after Prusty and Farooq, 2020).*

Uncertainty in rainfall and scarcity of surface water in some areas have resulted in over-exploitation of groundwater resources, especially during the summer season when there is a very limited natural recharge with a significant decrease in the groundwater level. Intensive irrigation is the main factor in stressing the groundwater resources. Almost all the coastal states are under stress with groundwater conditions categorized as semi-critical, critical, over-exploited, and saline. Seawater intrusion is more prominent on the east coast than the west coast of India because of different factors: the larger extension of the coastline; the geological formation with thicker alluvial sediments (which facilitate the seawater inflow into the east coast aquifers); significant sediment loads brought by rivers, whose deposition results in a lower hydraulic gradient, and frequent cyclonic disturbances resulting in higher tidal activities, flooding and salinization in the coastal areas (Prusty and Farooq, 2020).

Saltwater has also intruded into many coastal aquifers of the United States, Mexico, and Canada, but the extent of saltwater intrusion varies widely among localities and hydrogeologic settings. In some instances, saltwater contamination is of regional extent and has resulted in the closure of many groundwater supply wells.

Groundwater pumping is the primary cause of saltwater intrusion in coastal regions of North America, but lowering of the water table by drainage canals has also led to regional saltwater contamination in a few locations, such as south-eastern Florida, where an extensive network of canals was constructed mainly for agricultural and urban development. There are different modes of saltwater intrusion into coastal aquifers, such as lateral intrusion from the ocean, upward intrusion from deeper saline zones of a groundwater system, and downward intrusion from coastal waters. Saltwater contamination also has occurred along open boreholes and within abandoned, improperly constructed, or damaged wells that provide preferential pathways for vertical migration across interconnected aquifers. Some examples in the United States are: lateral encroachment of saltwater into confined freshwater aquifers in the Cape May County, New Jersey, situated on a peninsula, especially in the Cape May City and vertical migration along fractures in the aquifer system in south-eastern Georgia and north-eastern Florida (Figure 1.3). In Canada, most of saltwater intrusion occurs naturally along river channels due to high tides. An exception is the saltwater intrusion into the sandstone aquifers of Prince Edward Island, caused by groundwater pumping. Saltwater intrusion on the island is facilitated by fractures within the sandstone that increase the overall permeability of the aquifer. Finally, in Mexico one of the most extensive saltwater-intrusion problems is in the western state of Sonora, where lateral saltwater intrusion from the Gulf of California has occurred in several coastal irrigation districts in response to pumping for agriculture that exceeds the natural recharge rates that occur within this arid region (Barlow and Reichard, 2010).



Not to scale


(b) 

Figure 1.3 (a) Hydrogeologic sections showing lateral encroachment of saltwater and contamination of supply wells at the Cape May City (New Jersey) well field and map of Cape May County, New Jersey; (b) Simplified conceptual model of saltwater vertical migration along fractures in the aquifer system in south-eastern Georgia and north-eastern Florida (after Barlow and Reichard, 2010).

Lastly, in Africa over the 50% of the population live in coastal zones. In East Africa more specifically, coastal aquifers are the main source of freshwater supply for all the economic sectors and domestic activities and groundwater exploitation has increased with time. The population growth along the coastal areas of Kenya causes increasing water demand, which is mainly met by exploitation of coastal groundwater resources. The Tiwi aquifer (near the Tiwi village) is amongst the most threatened aquifers in East Africa by seawater intrusion because of groundwater over-exploitation. Figure 1.4 shows a comparison of 2016 groundwater data with the 1977 data (post and prior groundwater development, respectively), suggesting that the seawater front in the Tiwi wellfield has moved inland as a result of over-exploitation of groundwater resources to meet the demand of ever-increasing population. Over-pumping together with possible future decrease in rainfall and increase in temperature (which would affect the recharge negatively) will lead to water scarcity if not controlled, with great effects on socio-economic development of the region (Oiro and Comte, 2019).

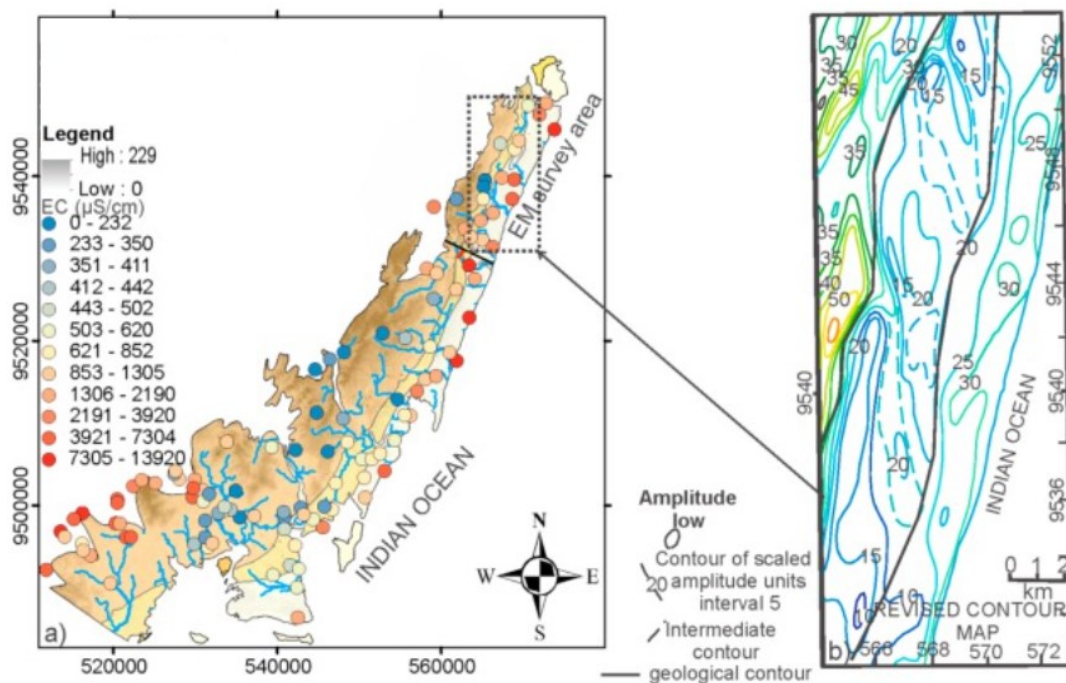


Figure 1.4 (a) Pore water EC in 2016 obtained from groundwater sampling of wells and boreholes; (b) Total aquifer EC in 1977 obtained from airborne electromagnetic surveys (after Oiro and Comte, 2019).

## 1.3 Management strategies: prevention and mitigation

Seawater intrusion in coastal aquifers is a widespread problem which requires sustainable management strategies and measures to restore groundwater quality or at least to prevent further degradation of water quality. The choice of a certain management strategy considers different constraints such as the strategic nature of the aquifer (related to the importance and scarcity of freshwater), existing infrastructures and historical rights that require abstraction rates and water quality remain almost unchanged. Consequently, it is as important as challenging to find a proper trade-off between pumping demand and quality requirements (Abarca et al., 2006). This evaluation implies the estimation of a suitable limit for the landward extent of the saline water body and the computation of the freshwater discharge towards the sea needed to keep the interface between seawater and freshwater in a certain position. Various measures to control seawater intrusion have been introduced in recent decades. This paragraph presents an overview of the main available management strategies, distinguished in conventional methods, physical barriers, and hydraulic barriers according to *Hussain et al. (2019)*.

### 1.3.1 Conventional methods

Conventional methods include the reduction of pumping and the relocation of pumping wells, which can be used as temporary solutions together with other control measures.

The reduction of abstraction rates from pumping wells is the simplest and most cost-effective measure to avoid the overexploitation of groundwater and to control seawater intrusion problems. However, the possibility of this option can be limited in some areas due to high water demands. As previously mentioned, the agriculture is the main responsible of water consumption all over the world. This means that actions taken in this sector (such as a change of crop patterns, a reduction of high-demand water crops, and the adoption of water-saving irrigation techniques) can have a significant impact in the reduction of groundwater pumping.

As concerns the relocation of pumping wells, the wells near the coastline or across the contaminated zone must be eliminated and moved further inland to guarantee an adequate seaward hydraulic gradient. Here too, there can be some restrictions due to, for example, the lack of land, conflicts with public projects or private infrastructures and the transportation costs of water from the new pumping wells to the already existing areas near the coastline. Therefore, the new location of the pumping

wells should be accurately designed to be effective in controlling the problem. Optimization methods are then used to address practical questions related to the location of well field and the abstraction rates.

### 1.3.2 Physical barriers

Physical subsurface barriers are distinguished in three types, according to the position of the wall into the aquifer: cut-off wall, installed from the top of the aquifer to a predefined depth and with the discharge below the barrier; subsurface dam, resting on the aquifer bottom and allowing the natural discharge of freshwater above its crest, and a fully penetrating barrier extended throughout the whole aquifer depth (Figure 1.5). They can be impermeable and semi-permeable and they are constructed parallel to the coast.

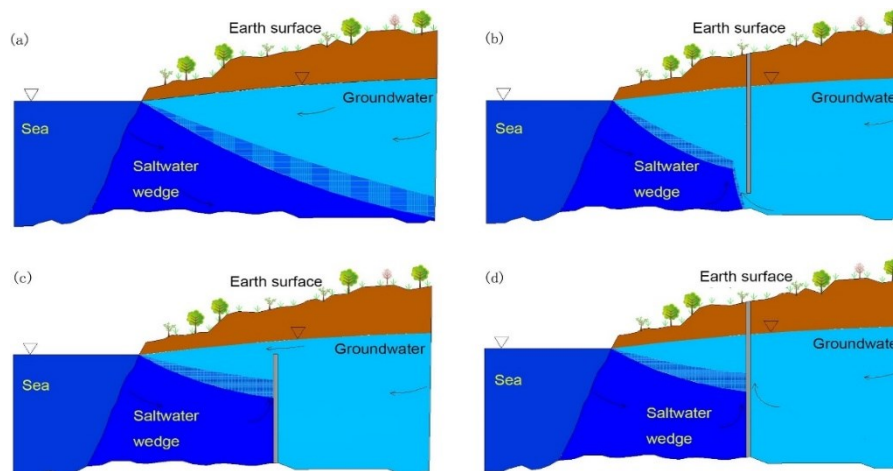


Figure 1.5 Schematic diagrams of: (a) Seawater intrusion in natural conditions, (b) Cut-off wall, (c) Subsurface dam and (d) Fully penetrating barrier (after Chang et al., 2019).

Wu et al. (2020) used a 3D numerical model to test the efficiency of these subsurface barriers (assumed to be impermeable) in preventing seawater intrusion in a simplified representation of a coastal aquifer, with and without pumping well. In the absence of pumping, the cut-off wall resulted to have higher performances in excluding seawater compared to subsurface dams of the same vertical length, especially for barriers closer to the coast. In pumping scenarios, subsurface dams were more efficient than cut-off walls in terms of maximum safe pumping rates. This occurs because without pumping the seaward freshwater flow is forced to pass below the cut-off wall, hindering the landward advance of the saltwater wedge, whereas with a subsurface dam freshwater would flow over the crest in a similar way as it discharges towards the sea without barriers. By a similar reasoning, the pumping effect moves saltwater along the aquifer bottom and, therefore, a subsurface dam can more effectively

block it. In most cases, fully penetrating barriers performed optimally, but it is important to note that they may cause greater negative effects such as inland soil salinization and accumulation of pollutants. Comparable results were found in both confined and unconfined aquifers. In general, subsurface barrier design should consider the effect of shore-parallel length (the flow around the barrier edges) to avoid overestimation of the barrier benefits.

Combined barriers are also investigated in *Abdoulhalik et al. (2017)*, where 2D laboratory experiments and numerical simulations were developed to study the effect of a mixed barrier system made up of a semi-permeable subsurface dam and an impermeable cut-off wall. The results showed the mixed barrier can significantly enhance the efficiency of seawater prevention than the simple cut-off walls or the semi-pervious subsurface dams. Moreover, the construction costs required for the mixed barrier are lower, mainly because its penetration depth is about 40% of the aquifer thickness while the single cut-off wall must penetrate to the deeper zone of the aquifer (about 90% of the aquifer thickness).

As to physical surface barriers, we refer to coastal land reclamation (Figure 1.6): the coastline is artificially extended with a desired geometry and slope seaward, using a suitable type of soil. This technique is mainly adopted in the case of new urbanization because of population growth. In order to restore the hydraulic equilibrium, the fresh groundwater penetrates the new soil thus increasing the distance between inland pumping wells and the coastline with a consequent decrease of the saltwater intrusion process. The choice of this type of intervention is limited due to some constraints such as the cost of equipment and materials, possible land subsidence and the environmental impact on marine life, fishing, and tourism activities.

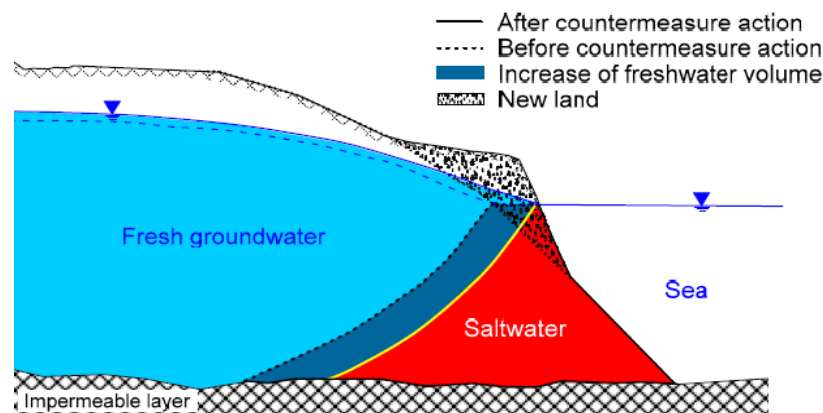


Figure 1.6 An illustration of coastal land reclamation before and after countermeasure action (after Hussain et al., 2019).

Land reclamation is common in many coastal areas of the world (such as UK, USA, Korea, Japan, and the Netherlands) due to the increasing demand for houses and other land use. An example is the Shekou peninsula, Shenzhen, China, where over 15 km<sup>2</sup> of land were reclaimed from the sea in different years from 1983 to 2005 (Figure 1.7). After reclamation, there was a slow but significant modification of the groundwater flow system, including change of the seaward groundwater discharge and a regional increase of groundwater level due to the increase of recharge in the newly reclaimed land (Hu and Jiao, 2010).

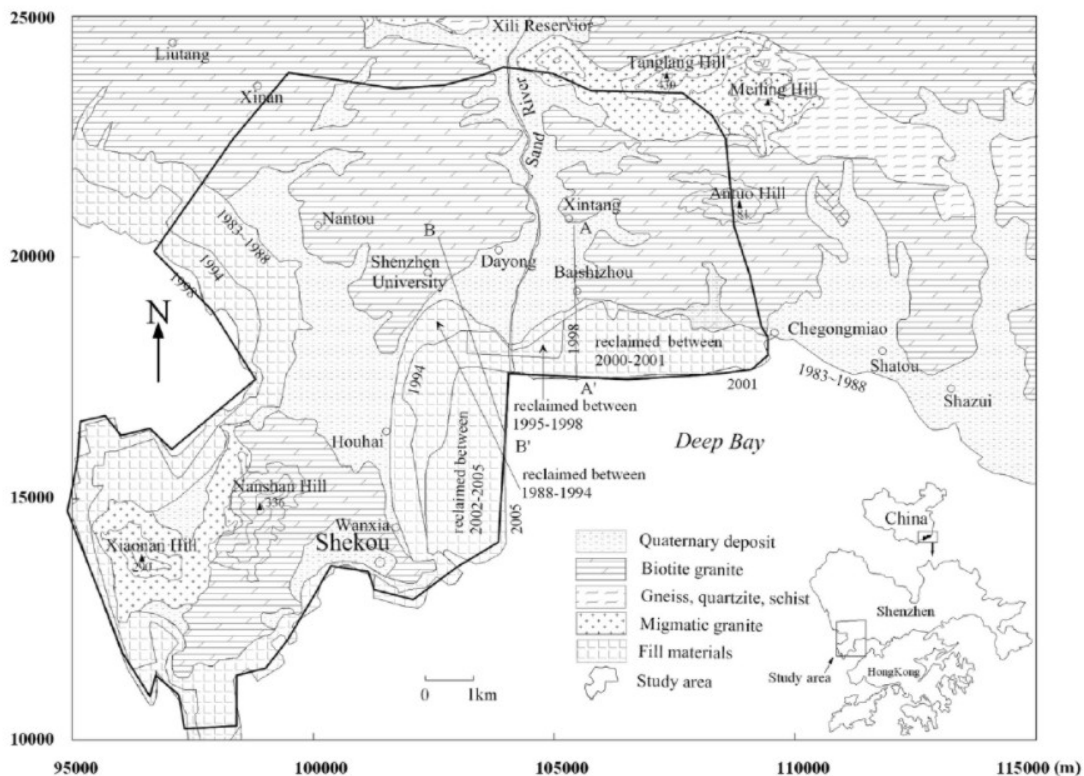


Figure 1.7 Location of the study area in the Shekou peninsula and the change of coastline corresponding to different years (after Hu and Jiao, 2010).



### 1.3.3 Hydraulic barriers

Hydraulic barriers can be categorised in three main types: positive, negative, and mixed barriers (Figure 1.8).

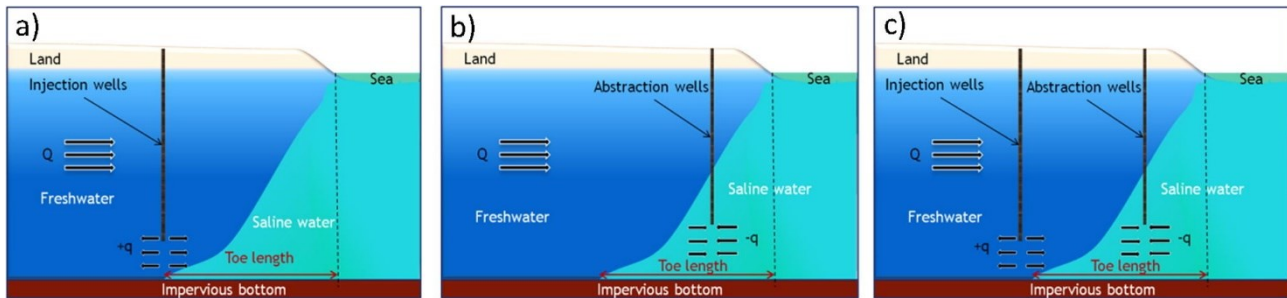
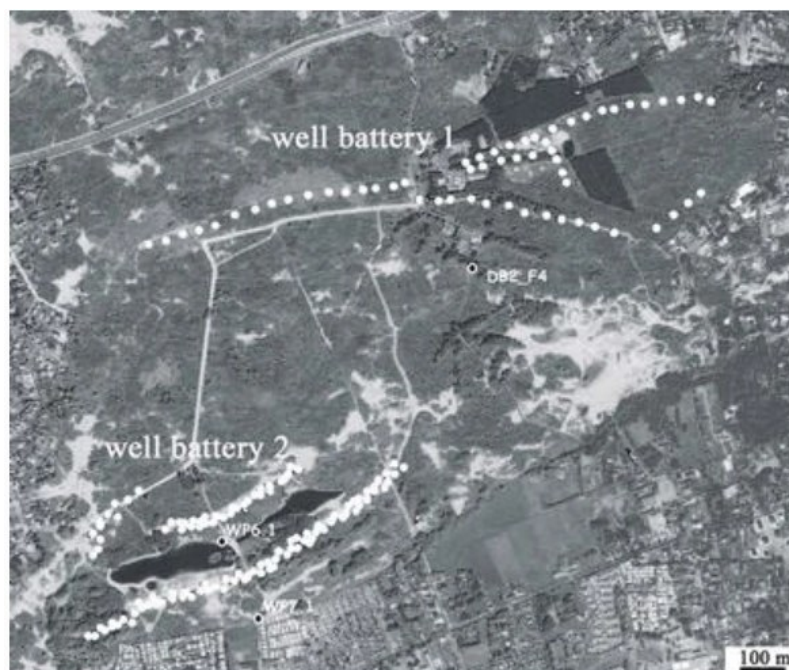


Figure 1.8 Simplified diagrams of the main types of hydraulic barriers: a) Positive barrier, b) Negative barrier and c) Mixed barrier (after Abdoulhalik et al., 2017).

In positive or pressure barriers, high-quality water (that is surface water, rainwater, extracted groundwater, treated wastewater and desalinated water) is injected into the aquifer to increase the water table and thus to maintain the seaward hydraulic gradient and hinder the seawater intrusion. Recharge wells are often located in series along the seacoast. Positive barriers are one of the most popular techniques, due to the higher cost of equipment, materials, and installation of physical barriers at a large scale. They are efficient in delaying seawater intrusion in any geological condition, but their performances are reduced if injection wells are placed farther and higher from the toe position of the seawater wedge. Freshwater injection has also been compared to air injection which can be a viable option in regions with limited access to freshwater, despite its lower effectiveness. The artificial recharge of groundwater can also be done with the help of surface reservoirs, lakes, and canals. One of the main limitations of these barriers is due to the scarcity of water, stressing the important role that can be played by renewable sources of water in the artificial recharge to mitigate seawater intrusion.

Negative or abstraction barriers consist of pumping the intruding saltwater (brackish or saline water) near the coast through deep abstraction wells. The abstracted water can be directly discharged into the sea or it can be used as feed water for desalination plants or in industrial activities, for instance for cooling purposes. The disposal of the extracted groundwater into the sea could be a source of concern due to the environmental impact on marine life, fishing, and tourism activities. Furthermore, due to the seaward hydraulic gradient created by this strategy, the barrier turns out to extract more freshwater than saltwater which eventually cause a reduction of the available groundwater of the aquifer.

Depending on the level of risk of seawater intrusion and its impact on the groundwater quality in coastal aquifers, the previously mentioned strategies can also be combined to better control the seawater intrusion, benefiting from their advantages together. The combination of a positive and a negative barrier is called mixed hydraulic barrier, where freshwater is injected and at the same time saltwater is extracted to move the saltwater wedge seaward. Some variants have been suggested but for the sake of brevity they are not discussed here. This measure would involve important operational and maintenance costs due to the high risk of well clogging (Abdoulhalik et al., 2017). Another example is given by the combination of recharge barrier with the reduction of pumping, which was adopted in the western Belgian coastal plain. In this area, the two Westhoek and St-André water extractions faced problems with lowering of the groundwater table, while for Westhoek also saltwater intrusion was an issue. For the latter, it turned out that decreasing the extraction rate was the only effective option, but subsequently two interconnected artificial recharge ponds with tertiary treated wastewater were installed for the other extraction (Figure 1.9), also to compensate for the decrease in extraction rates. Due to the reduction of pumping, the water table increased with 3 m in the vicinity of the Westhoek water extraction after about 10 years. More water can be extracted than in the past, but less water is extracted directly from the aquifer and therefore the groundwater resources of the aquifer are less exploited (Vandenbohede et al., 2009).



*Figure 1.9 Location of the well batteries of the St-André water extraction and of the artificial recharge ponds (between the wells of the second well battery). The wells are indicated with white dots (after Vandenbohede et al., 2009).*

## 1.4 The MoST project and the thesis aims

Nowadays, many coastal regions around the world are affected by seawater intrusion and saltwater contamination is expected to worsen with climate change effects and groundwater overexploitation. Consequently, this topic is of ever-increasing concern which makes necessary a better understanding of the physical processes at the base of this phenomenon to find proper countermeasures.

For this purpose, the Interreg Italy-Croatia MoST (Monitoring Sea-water intrusion in coastal aquifers and Testing pilot projects for its mitigation) project has been started (January 2019 – June 2022), given that agricultural activities and tourism are damaged by saltwater intrusion in both these countries. The main goal of this project is the monitoring of the seawater intrusion in certain areas of the northern Adriatic coastland in Italy and the Neretva plain in Croatia to assess its relevance and test suitable countermeasures (such as subsurface barriers and recharge wells) in a transnational level. This is performed by means of detailed data collection, geophysical surveys, monitoring sites, and laboratory and numerical experiments. In this way, it is possible to better understand the process and its evolution, verify the efficiency of the considered countermeasures in pilot sites, to simulate and analyse the field results, and forecast different scenarios. The project is carried out with the collaboration and the involvement of local stakeholders and authorities, which will benefit from enhanced crop productivity and touristic activities.

This thesis is developed inside the wider MoST project program, performing a modelling study of a recharge drain as a possible measure to mitigate soil and groundwater salinization. The model is used to simulate the dynamics of saltwater intrusion and to assess the potential effects of a drain recently established along a sandy paleochannel in a pilot site at the southern margin of the Venice lagoon. The drain will be used to distribute freshwater into a farmland where the shallow phreatic aquifer is characterized by high salt concentrations.

The thesis is composed of an initial section describing the study area of the project and available data collected in the last years, which are necessary to implement realistic parameters in the numerical model. Subsequently, a section is dedicated to the 3D finite-element density-dependent groundwater flow and transport model, introducing the coupled density-dependent flow and transport equations solved with the GroundWater Simulator. Finally, the application of the model and the preliminary results are presented to assess the effects of the drain in the farmland.

## Chapter 2

# The study area: a coastal farmland near Ca' Pasqua

---

### 2.1 The study area

This work focuses on an area of about 160×650 m including a coastal farmland for maize cultivation. It is located near Ca' Pasqua, in the southern part of the Venice lagoon, Italy, approximately 7 km from the Adriatic Sea (Figure 2.1). The area is delimited by mainly agricultural fields at the South and it is crossed by the Bacchiglione and Brenta rivers and the Morto channel at the North before the Venice lagoon (characterized by the presence of salt marshes).



*Figure 2.1 The study area location near Ca' Pasqua, at the southern boundary of the Venice lagoon (Italy).*

The two rivers flow parallel in NW-SE direction just before the Bacchiglione converges in the Brenta river discharging into the Adriatic Sea. The Morto channel is a reclamation channel (parallel to the Bacchiglione river), whose water level is controlled by a few pumping stations upstream and a mobile gate connecting the channel to the Bacchiglione river downstream.

A pumping station, the Casetta pumping station, and a dense network of open ditches control the depth to the groundwater table, which is kept below the ground level and shallow during summer to promote sub-irrigation (Manoli et al., 2015). On the contrary, during highly rainy periods, the water is conveyed in the lagoon through the pumping station to avoid flooding of the agricultural land.

The ground level of the farmland is on average 2.5 m below the mean sea level (msl), in the range of approximately -1.5 to -3.3 m below msl (Manoli et al., 2015). Especially in the southern part, land subsidence (mainly due to the oxidation of superficial peat soil) has caused a lowering of more than 1 m over the last few decades reaching an elevation of around -3 m below msl (Gambolati et al., 2006).

The soil is primarily composed of silt and clay with the presence of sand and peat because the coastal area was covered by swamps and reeds before land reclamation occurred in the '30s which converted the area mainly to agricultural fields.

From a hydrological point of view, in the study area there are a series of deep aquifers up to 100 m. In the first 20-30 m the soil is very heterogeneous because of the presence of different lithological deposits: alluvial, lagoonal, littoral and deltaic. There are also phreatic, semi-confined and locally confined aquifers (Rizzetto et al., 2003; Teatini et al., 2011; Scudiero et al., 2013).

Since the inland ground is depressed compared to the lagoon, the hydraulic gradient is reverse and saltwater seriously affect this region. The salt plume intrudes from the sea and the lagoon up to 10 - 15 km inland and up to 100 m of depth in the southern part. The seawater intrusion is worsened by different factors: the area elevation below the mean sea level; the seawater encroachment along the river mouths, due to the occurrence of high tide together with a low hydrometric level in the river; a general decrease in the freshwater river discharge, and the water levels in the drainage channels kept low by pumping stations (Teatini et al., 2011). Moreover, the stratigraphy of the subsoil contributes to amplify the saline intrusion. From about -3 to -11.8 below msl, there are some sandy bodies which are the remains of ancient littoral ridges and paleochannels from late Pleistocene and Holocene and they have a higher hydraulic conductivity in comparison with the surrounding soil (Rizzetto et al., 2003). Paleochannels are ancient stretches of watercourses by now buried underground and they are fundamental features of this case study because they consist of sandy bodies hydraulically connecting the lagoon and the nearby rivers with the agricultural land. This allows the saline intrusion to move faster through them: they represent preferential pathways for flow and transport. This characteristic can then be used in our favour to enhance the spreading of freshwater in the subsoil through a drain and mitigate soil and groundwater salinization.

In the study area, there is a main paleochannel crossing the field in SW-NE direction. A recharge drain was recently installed at 1.5 m depth along the paleochannel (Figure 2.2). Freshwater is supplied



*Figure 2.2 Trace of the recharge drain (line in blue) along the main paleochannel (in green) in the study area delimited in red (to the left) and the drain installation during the field operations (to the right).*

by the Morto channel, displacing salt in the most superficial layers to protect the plants in the field which cannot tolerate high salt concentrations. This is done without energy consumption because the hydraulic head is higher in correspondence of the channel. The corrugated polyethylene drain has an outside diameter of 160 mm and an inside diameter of 120 mm (Appendix A.1). The drain is covered throughout its length (220 m) by a geotextile to reduce clogging due to the surrounding soil (Figure 2.3). This is because higher is the permeability of the drain, lower is its resistance and thus the soil is more likely to enter the drain. So far, only one experimental test of the drain was carried out in October 2019 for a few hours with a flowrate of about 580 m<sup>3</sup>/day.



*Figure 2.3 Detail of the drain location along the paleochannel (to the left) and of the drain (to the right).*

As already mentioned, the efficiency of the drain should be also enhanced by the higher permeability of the paleochannel. The goal is to reduce the salt concentration in the upper part of the aquifer and the superficial soil to promote crops growth. Since the groundwater table and the water content in the vadose zone are not constant, it is possible to control the drainage regime based on the climatic period and the agronomic phases.

## 2.2 Available data

In the last years, the area has been subjected to several measurements, geophysical surveys and monitoring activities performed both in the field and in laboratories to better characterize soils and (surface and ground) waters. These data are necessary to implement realistic parameters in the numerical model.

The level elevation was obtained by kinematic GPS survey. The acquired data were used to develop a digital map with georeferenced points. Some manual points were added to have a more detailed description of the ground elevation.

The lithological characterization of the study area was defined with measurements carried out in three boreholes (Figure 2.4). The upper part is mainly composed of silt below which coarse sand is located down to about -12 m below msl. At depth larger than -18 m below msl there is a Caranto unit, that is an over-consolidated clay layer which separates the Holocene from the Pleistocene deposits. Given

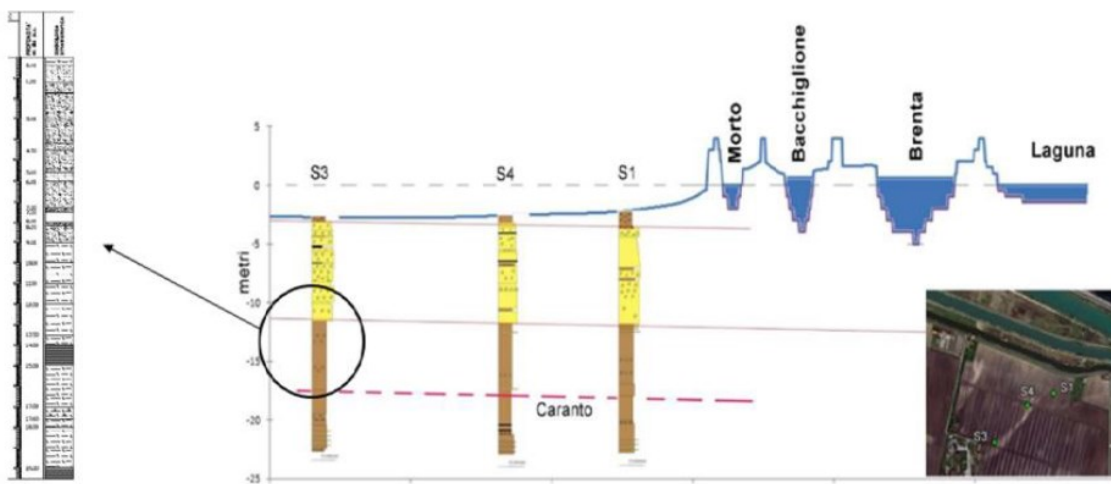
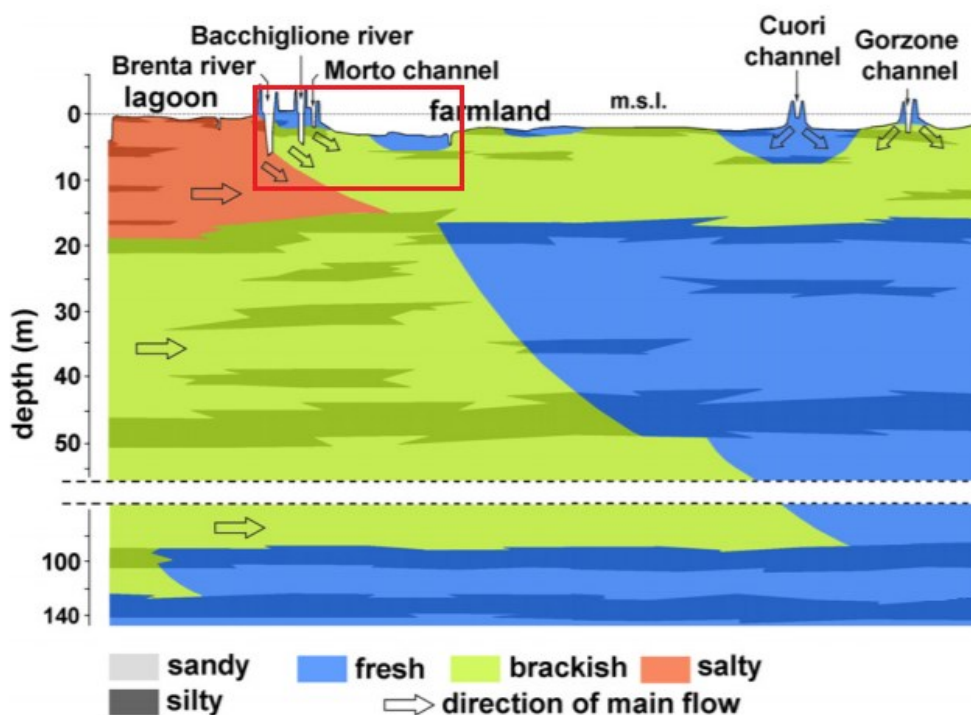


Figure 2.4 Boreholes data and stratigraphy below the paleochannels (S1, S2 and S3). Only borehole S1 is located within the simulated area (after Cunico, 2019).

that it has a low conductivity, the Caranto acts as a natural barrier and partially hinders further saline intrusion downward.

A representative sketch of the conceptual model was obtained in *Teatini et al. (2011)* by integrating the dataset provided by an AEM (Airborne ElectroMagnetics) survey with available hydrogeologic, geological and morphological information (Figure 2.5). At the lagoon margin, the groundwater moves preferentially from the lagoon towards the farmland mainly because of the higher density of saltwater and the inland piezometric head lower than the surface water level. This is because the land elevation is below the mean sea level with a widespread use of pumping stations to keep lowlying lands drained.



*Figure 2.5 Conceptual model of the southern Venice Lagoon subsurface. The study area is delimited by the red rectangle (after Teatini et al., 2011).*

The groundwater table is controlled by a drainage system. It oscillates between -3.6 and -4 m below msl depending on the season. During winter, the water level is lowered with pumping stations to prevent flooding whereas in summer it is raised to enhance the irrigation of the agricultural soil. Where the Bacchiglione converges in the Brenta river, there is a floodgate which controls the dynamics inside the Morto channel. Its water level was measured in 2006 by Consorzio di Bonifica Adige-Bacchiglione and it resulted constant at about 0 m a.s.l. with negligible oscillations. Instead, the water level in the lagoon side fluctuates due to tide. The water levels oscillations in Bacchiglione and Brenta rivers depend on seasonal conditions and they are relevant in the dynamics of saline intrusion (Cunico, 2019). The study “Flussi di acque sotterranee nel Sistema lagunare veneziano”



carried out by CORILA (2003-2006) provides measurements of water levels in superficial bodies and aquifers in correspondence of piezometers (CA01-CA14) located in the study area and the surrounding. The Figure 2.6 shows the minimum and maximum measured levels in the superficial bodies and in the piezometers projected along a North-South section orthogonal to the lagoon boundary. It is possible to note that the groundwater table is located at about -4 m below msl (1-1.5 m below the ground surface). During late spring to early autumn, the water level of the Brenta and Bacchiglione rivers is generically lower and they become salty because the seawater encroaches from

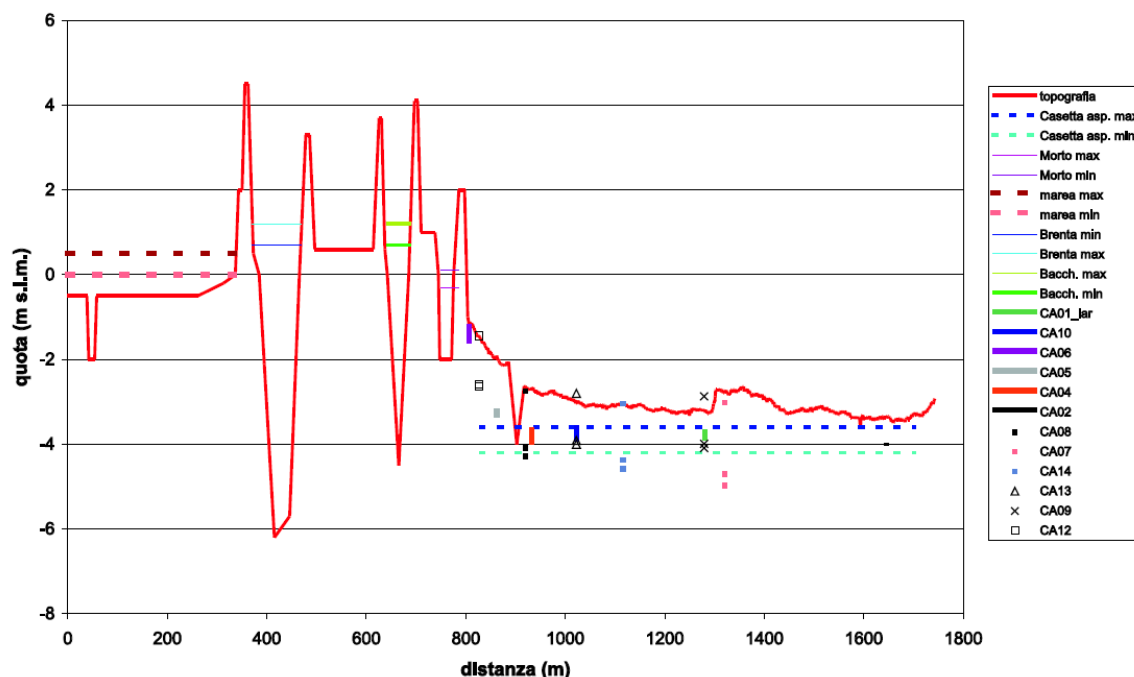


Figure 2.6 Minimum and maximum water levels measured in the superficial bodies and in the piezometers CA01-CA14 along a section North-South at the lagoon margin (after Rorai, 2007).

the mouths and flows up the rivers. Therefore, saline intrusion advances inland for kilometres, exacerbated by the saltwater flux that seepages from the riverbeds. In contrast, during the wet season, the freshwater discharges of the rivers are generally higher, reducing the seawater contamination.

Salinity levels in the Morto channel (Figure 2.7), Bacchiglione (Figure 2.8) and Brenta (Figure 2.9) rivers were monitored by Consorzio di Bonifica Adige Euganeo, which made measurements in the locations showed in Figure 2.10 at different depths and times from 27/05/2020 to 16/12/2020.

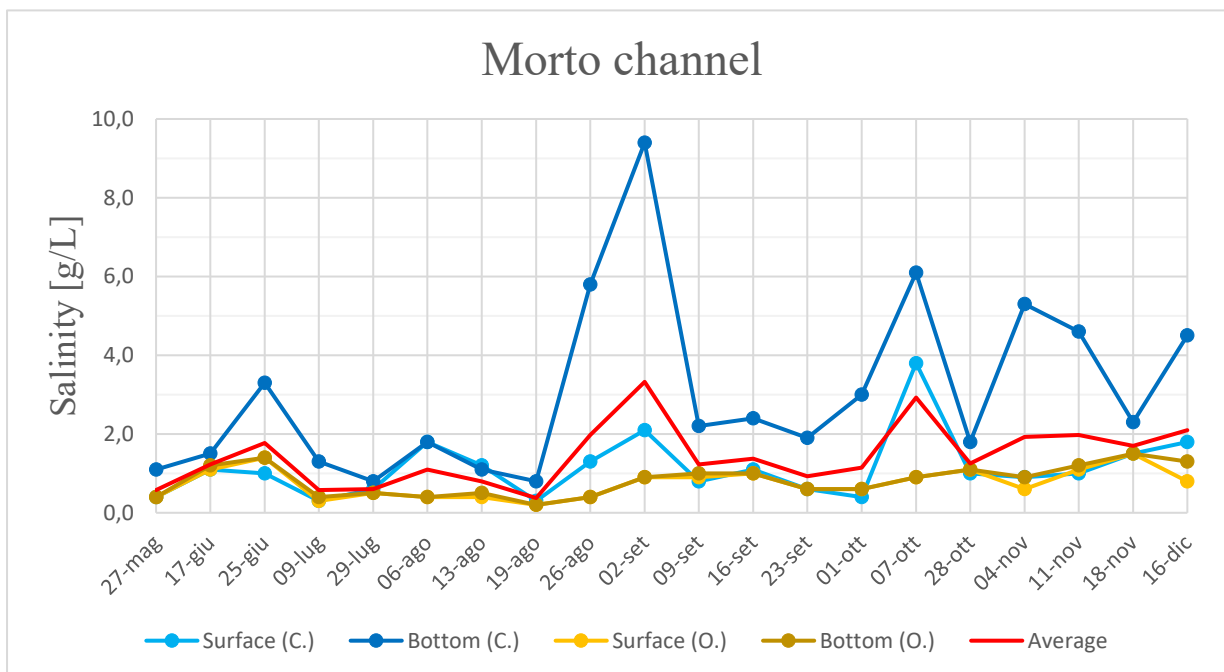


Figure 2.7 Salinity levels in the Morto channel at the surface and bottom measured in the stations Casetta (C.) and Oratorio (O.) and average level.

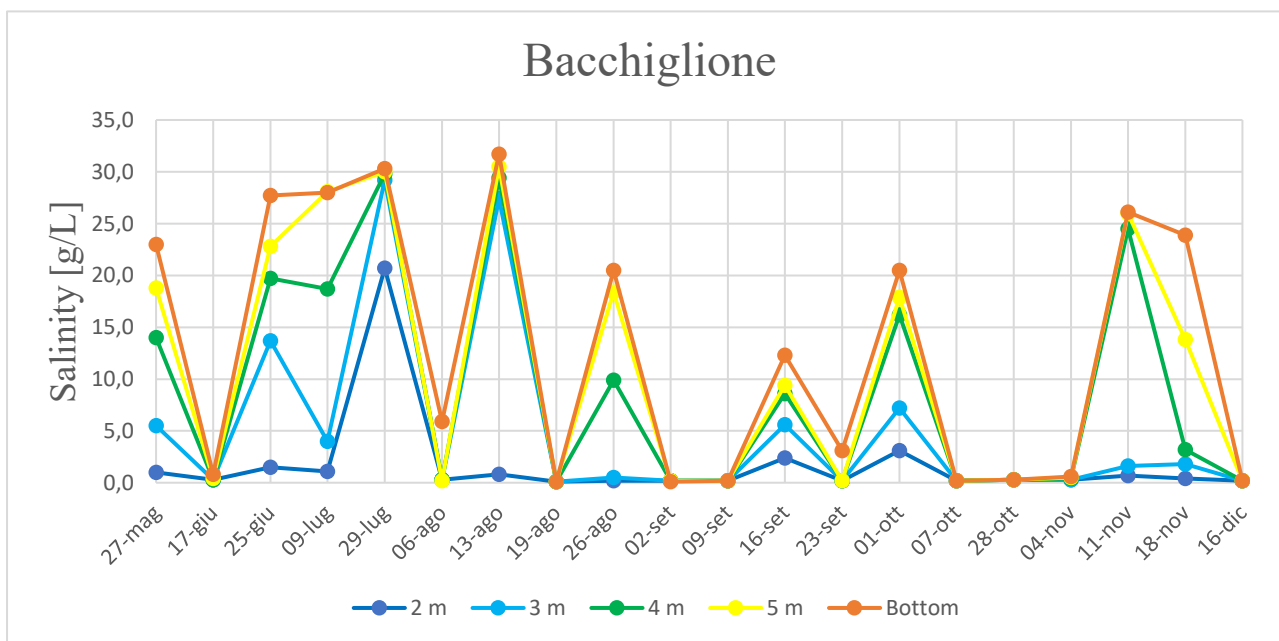


Figure 2.8 Salinity levels in the Bacchiglione river at different depths.

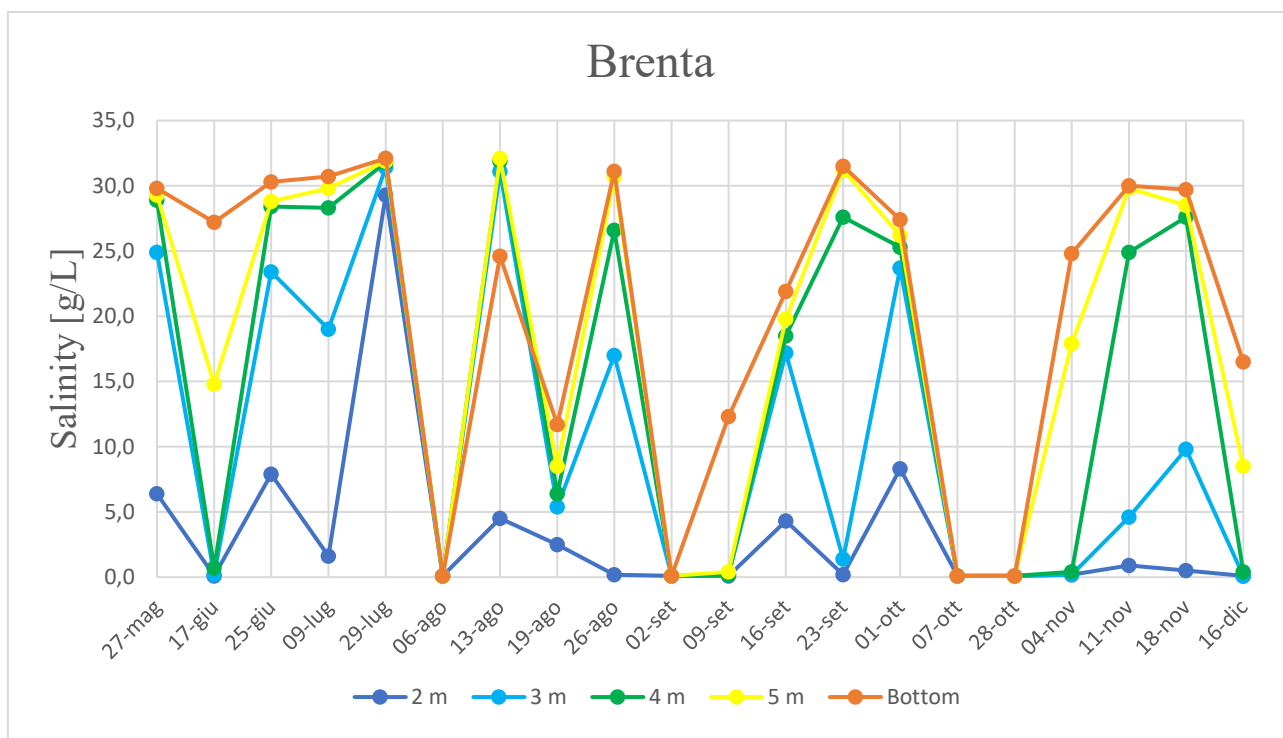


Figure 2.9 Salinity levels in the Brenta river at different depths.



Figure 2.10 Experimental measurement locations (in yellow) for salinity levels in the Morto channel and in the Bacchiglione and Brenta rivers.

Precipitation and evapotranspiration are also available. They are daily data during the year 2011, acquired by a rain gauge and provided by a numerical model (without spatial variability), respectively (Figure 2.11).

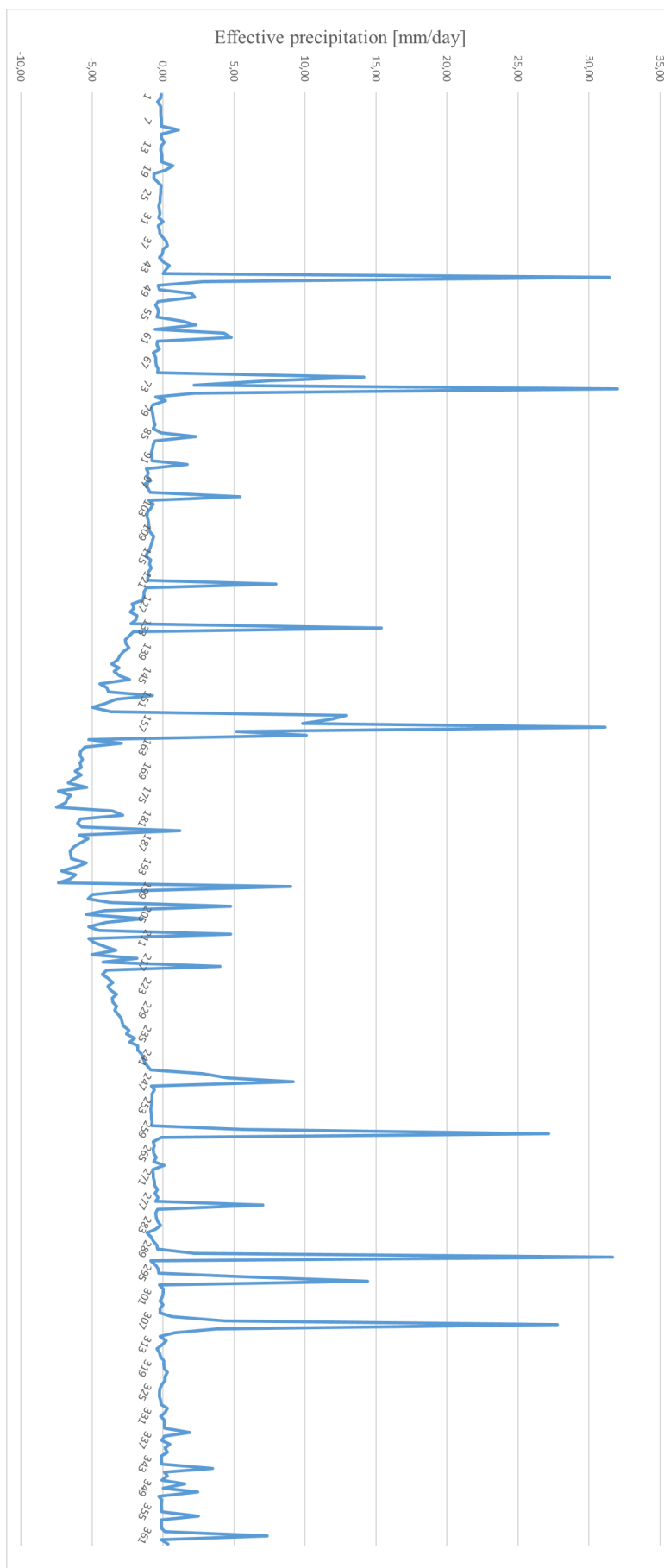


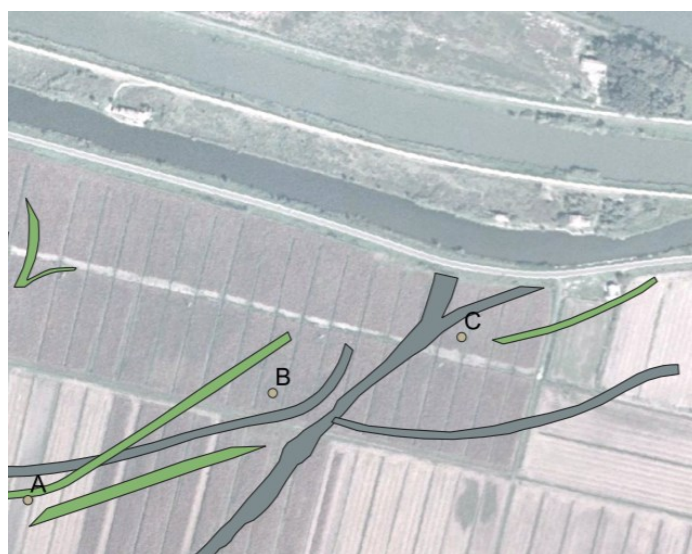
Figure 2.11 Effective precipitation during the year 2011.

The properties of the unsaturated soils have been characterized using lab tests and field measurements. The van Genuchten parameters used to characterize the flow in the vadose zone are the residual ( $\theta_r$ ) and saturated ( $\theta_s$ ) moisture content, empirical parameters ( $\alpha$  and  $n$ ), the saturated hydraulic conductivity ( $K_s$ ) and the pore connectivity and tortuosity ( $l$ ). The parameters resulting from laboratory tests were obtained only for sandy and silty/clayey soils (Bevington et al., 2016) and they are shown in Table 2.1. As concerns the field measurements, on the basis of collected data (water

*Table 2.1 Parameters obtained by laboratory tests to characterize the water retention curve for sandy and silty/clayey soils (Bevington et al., 2016).*

	Sand	Silt/Clay
$\theta_r$	0,12	0,32
$\theta_s$	0,49	0,59
$\alpha$ (1/m)	2	3
$n$	1,75	1,32
$K_s$ (m/d)	0,56	0,05
$l$	0,002	-0,74

content and capillary pressure) in three monitoring stations (indicated with A, B and C in Figure 2.12) during previous studies, it was possible to characterize the hydraulic parameters of the soil by an inverting procedure developed within the applications of Hydrus, which is a modelling software used for analysis of water flow, heat and solute transport in variably saturated porous media. The results are reported in Table 2.2 for the three stations at different depths.



*Figure 2.12 Stations A, B and C of field measurements for hydraulic characterization of the soil.*

Table 2.2 The van Genuchten inverted parameters for the stations A, B and C. The four layers correspond respectively to the following depth ranges: 0 - 0.15 m, 0.16 - 0.35 m, 0.36 - 0.51 m and 0.52 m – maximum aquifer depth. The pore connectivity and tortuosity  $l$  is always equal to 0.5.

Station A

Layer	Sand (%)	$\theta_r$	$\theta_s$	$\alpha$ [1/cm]	$n$	$K_s$ [cm/d]
1	39,6	0,3035	0,5009	0,007	2,102	36,29
2	42,3	0,2309	0,659	0,0545	1,201	592,42
3	17,8	0,1958	0,6112	0,0559	1,132	2,6679
4	17,8	0,0023	0,5538	0,046	1,046	34,97

Station B

1	51,9	0,0299	0,4629	0,0094	1,926	104,18
2	49,2	0,1094	0,517	0,0698	1,3	117,43
3	92,1	0,0792	0,4808	0,0093	3,296	56,66
4	92,1	0,0964	0,4865	0,0296	1,629	115,01

Station C

1	26,9	0,16237	0,6046	0,04761	1,4434	397,36
2	32,4	0,25116	0,636	0,24224	1,1444	816,21
3	45	0,0005	0,7677	0,00913	1,1767	1072,3

## Chapter 3

# The mathematical and numerical models

---

### 3.1 Flow and transport equations

The governing equations used for the mathematical formulation of the problem of salt movement in a variably saturated aquifer are the flow equation and the transport equation in porous media. Mathematical models are based on partial differential equations imposing mass conservation for the fluid mixture and the contaminant (i.e. salt). These equations are reported here for the general case of a three-dimensional porous medium.

The flow equation through variably saturated porous media is applicable both in the unsaturated and saturated zone. It is known as the Richards equation, which is reported in the following:

$$\sigma \frac{\partial \psi}{\partial t} = \nabla \cdot [K_s K_r (\nabla \psi + \eta_z)] + q \quad (3.1)$$

where  $\sigma$  is the general storage term or overall storage coefficient,  $\psi$  is the pressure head,  $t$  is time,  $\nabla$  is the gradient operator,  $K_s$  is the saturated hydraulic conductivity tensor,  $K_r$  is the relative hydraulic conductivity,  $\eta_z$  is a vector equal to zero along the horizontal directions  $x$  and  $y$  and 1 in its  $z$  component, i.e. along the vertical direction, and  $q$  represents distributed source or sink terms (volumetric flow rate per unit volume).

The general storage term  $\sigma$  is written as:

$$\sigma = S_w S_s + \phi \frac{dS_w}{d\psi} \quad (3.2)$$

where  $S_w = \theta/\theta_s$  is the water saturation, with  $\theta$  the volumetric moisture content (equal to the ratio of water volume to soil volume) and  $\theta_s$  the saturated moisture content (generally equal to the porosity  $\phi$  of the medium), and  $S_s$  is the specific elastic storage of the porous medium.

The Richards equation is obtained by combining the Darcy equation for an unsaturated porous medium:

$$q = -K_s K_r (\nabla \psi + \eta_z) \quad (3.3)$$

and the continuity equation for an incompressible fluid:

$$\nabla \cdot q + \frac{\partial \theta}{\partial t} = 0 \quad (3.4)$$

The Richards equation is highly nonlinear due to pressure head dependencies in the storage and conductivity terms which make it difficult to get analytic solutions of the partial differential equation. These terms can be expressed using various constitutive or characteristic relationships describing the soil hydraulic properties (Paniconi et al., 1994). We used the following expressions (van Genuchten, 1980):

$$S_e = \frac{\theta - \theta_r}{\theta_s - \theta_r} = (1 - (\alpha\psi)^n)^{-m} \quad (3.5)$$

$$K(\theta) = K_s S_e^{\frac{1}{2}} \left[ 1 - (1 - S_e^{1-m})^m \right]^2 \quad (3.6)$$

where  $\theta_r$  is the residual moisture content,  $K$  is the (unsaturated) hydraulic conductivity,  $S_e$  is the effective saturation, and  $\alpha$ ,  $n$  and  $m = 1-1/n$  are empirical parameters.

The transport equation accounts for advection (groundwater flow), molecular diffusion, and mechanical dispersion processes. The equation describing transport of a non-reactive solute reads:

$$\phi \frac{\partial S_w c}{\partial t} = \nabla \cdot (D \nabla c) - \nabla \cdot (c \mathbf{v}) + q c^* + f \quad (3.7)$$

where  $\phi$  is the porosity,  $c$  the salt concentration,  $D$  the dispersion tensor,  $\mathbf{v}$  the Darcy velocity vector,  $c^*$  the normalized concentration of salt in the injected (positive)/extracted (negative) volumetric flow rate  $q$ , and  $f$  the volumetric flow rate of injected/extracted solute that does not affect the velocity field. The advection term in the equation is represented by  $\nabla \cdot (c \mathbf{v})$ , whereas the molecular diffusion and the hydrodynamic dispersion are in the term  $\nabla \cdot (D \nabla c)$  (Gambolati et al., 1999).

The dispersion tensor  $D$  is defined in Bear (1979) as:

$$D_{ij} = \phi S_w \tilde{D}_{ij} = \alpha_T |\mathbf{v}| \delta_{ij} + (\alpha_L - \alpha_T) \frac{v_i v_j}{|\mathbf{v}|} + \phi S_w D_0 \tau \delta_{ij} \quad i, j = x, y, z \quad (3.8)$$



where  $\alpha_L$  and  $\alpha_T$  are the longitudinal and transversal dispersivity coefficients, respectively,  $|\mathbf{v}| = \sqrt{v_x^2 + v_y^2 + v_z^2}$  is the average flow velocity,  $\delta_{ij}$  is the Kronecker delta,  $D_0$  is the molecular diffusion coefficient and  $\tau$  is the tortuosity of the porous medium.

### 3.2 Density-dependent flow model

The problem of saltwater intrusion is described by means of a density-dependent flow process, where groundwater flow and solute transport equations are non-linearly coupled. The non-linearity is given by the fact that salt concentration influences the solution density and therefore the groundwater movement, which in turn affects the fate of the contaminant (Gambolati and Putti, 2000).

The mathematical model of density-dependent flow and transport in groundwater is written in terms of an equivalent freshwater head  $h$ , useful to compare levels with each other in case of fresh, brackish, and saline groundwater:

$$h = \psi + z \quad (3.9)$$

where  $\psi = p/(\rho_0 g)$  is the equivalent freshwater pressure head, with  $p$  pressure,  $\rho_0$  the freshwater density and  $g$  the gravitational constant, and  $z$  is the elevation (vertical coordinate directed upward). The density  $\rho$  of the saltwater solution is expressed as a function of the reference density  $\rho_0$  and the normalized salt concentration  $c$ :

$$\rho = \rho_0(1 + \epsilon c) \quad (3.10)$$

where  $\epsilon = (\rho_s - \rho_0)/\rho_0$  is the density ratio, typically  $\ll 1$ , and  $\rho_s$  the solution density at the maximum normalized concentration  $c = 1$ . According to the application,  $\rho_s$  can represent, for example, the seawater density or the density of the solution closest to a surface salt mound or around an underground saline diapir. The dynamic viscosity  $\mu$  of the saltwater mixture is also written in terms of  $c$  and of the reference viscosity  $\mu_0$ :

$$\mu = \mu_0(1 + \epsilon' c) \quad (3.11)$$

where  $\epsilon' = (\mu_s - \mu_0)/\mu_0$  is the viscosity ratio and  $\mu_s$  the viscosity of the solution at the maximum normalized concentration  $c = 1$ .

Consequently, the mathematical model is given by the coupled system of variably saturated groundwater flow and miscible salt transport equation:

$$\sigma \frac{\partial \psi}{\partial t} = \nabla \cdot \left[ K_s \frac{1 + \epsilon c}{1 + \epsilon' c} K_r (\nabla \psi + (1 + \epsilon c) \eta_z) \right] - \phi S_w \epsilon \frac{\partial c}{\partial t} + \frac{\rho}{\rho_0} q \quad (3.12)$$

$$\mathbf{v} = -K_s \frac{1 + \epsilon c}{1 + \epsilon' c} K_r (\nabla \psi + (1 + \epsilon c) \eta_z) \quad (3.13)$$

$$\phi \frac{\partial S_w c}{\partial t} = \nabla \cdot (D \nabla c) - \nabla \cdot (c \mathbf{v}) + q c^* + f \quad (3.14)$$

where the general storage term  $\sigma$  is now function of both the pressure head and the concentration and it is obtained multiplying the Equation 3.2 by  $(1 + \epsilon c)$  (Gambolati et al., 1999):

$$\sigma = S_w S_s (1 + \epsilon c) + \phi (1 + \epsilon c) \frac{\partial S_w}{\partial \psi} \quad (3.15)$$

### 3.3 Initial and boundary conditions

The mathematical formulation of the flow and transport problem is completed by initial and Dirichlet, Neumann or Cauchy boundary conditions.

As concerns the flow equation, these conditions are expressed in the following form:

$$\psi(\mathbf{x}, 0) = \psi_0(\mathbf{x}) \quad (3.16)$$

$$\psi(\mathbf{x}, t) = \psi_p(\mathbf{x}, t) \quad \text{on } \Gamma_1 \quad (3.17)$$

$$\mathbf{v} \cdot \mathbf{n} = -q_n(\mathbf{x}, t) \quad \text{on } \Gamma_2 \quad (3.18)$$

where  $\mathbf{x} = (x, y, z)^T$  is the Cartesian spatial coordinate vector,  $\psi_0$  the pressure head at time 0,  $\psi_p$  the prescribed pressure head (Dirichlet condition) on the boundary  $\Gamma_1$ ,  $\mathbf{n}$  the outward normal unit vector and  $q_n$  the prescribed flux (Neumann condition) across the boundary  $\Gamma_2$ . The sign convention used for  $q_n$  is positive for an inward flux and negative for an outward flux, which is consistent with the convention used for  $q$  and  $f$  in the flow and transport equations previously reported.

Regarding the transport equation, the initial and boundary conditions are:

$$c(\mathbf{x}, 0) = c_0(\mathbf{x}) \quad (3.19)$$

$$c(\mathbf{x}, t) = c_p(\mathbf{x}, t) \quad \text{on } \Gamma_3 \quad (3.20)$$

$$D\nabla c \cdot \mathbf{n} = q_d(\mathbf{x}, t) \quad \text{on } \Gamma_4 \quad (3.21)$$

$$(\mathbf{v}c - D\nabla c) \cdot \mathbf{n} = -q_c(\mathbf{x}, t) \quad \text{on } \Gamma_5 \quad (3.22)$$

where  $c_0$  is the initial concentration,  $c_p$  is the prescribed concentration (Dirichlet condition) on boundary  $\Gamma_3$ ,  $q_d$  is the prescribed dispersive flux (Neumann condition) across boundary  $\Gamma_4$ , and  $q_c$  is the prescribed total flux of solute (Cauchy condition) across boundary  $\Gamma_5$ . The sign convention for  $q_d$  and  $q_c$  is the same as for  $q_n$ ,  $q$  and  $f$  (Gambolati et al., 1999).

### 3.4 GroundWater Simulator (GWS) specifications

The simulations developed in this thesis have been carried out through the GroundWater Simulator (GWS). GWS is a software implemented in Fortran90 by M3E Srl (<https://www.m3eweb.it/>) updating and integrating previous codes developed at the Department of Mathematical Methods and Models for Scientific Applications, University of Padova (Paniconi et al., 1994; Gambolati et al., 1999). GWS solves the coupled density-dependent flow and transport equations using the finite element method (FEM). The Galerkin formulation approximates the partial differential equations involved in the process.

A FEM requires discretizing a given domain into elements (tetrahedra in GWS) connected to each other with a finite number of nodes. Therefore, the mesh (replacing and simplifying the considered geometry) must be constructed to improve the calculation operations, for example by avoiding a strong deformation of the elements and increasing the elements density (i.e. reducing the element characteristic dimension) in particular areas where we expect high pressure and concentration gradient. Iterative techniques (Picard or Newton) are implemented to solve the non-linear systems and conjugate-gradient like iterative solvers are implemented to subsequently solve the linear systems thus obtained. GWS is a software continuously “under development” and some improvements and updates have been made to the Fortran code based on this thesis work with the collaboration of the M3E developer. The following paragraphs are meant to provide a simple GWS manual, explaining the content of the input and output files listed in the file *gw.fnames* (Figure 3.1). Input files are the following: *param*,

*solver\_FLOW\_PIC*, *solver\_TRAN*, *coord*, *topol*, *mat\_SOIL*, *mat\_FLOW*, *mat\_TRAN*, *tablist\_SOIL*, *ic\_FLOW*, *ic\_TRAN*, *bcdir\_FLOW*, *bcneu\_FLOW*, *bcspg\_FLOW*, *bcatm\_FLOW*, *bcdir\_TRAN*, *print\_time\_FLOW*, *print\_time\_TRAN*, *print\_list\_nod\_FLOW*, *print\_list\_nod\_TRAN*, and *print\_list\_ele\_FLOW* (Appendix A.2). If we want to solve only a flow problem (without the transport), the files related to the transport (ending with “TRAN”) must be void. Physical units must be decided a priori and the inputs must be coherent with this choice. Output files are: *hw\_nod*, *hw\_ele*, *c\_nod*, *c\_ele*, *pro\_ele\_FLOW*, *hw\_nod\_list*, *c\_nod\_list*, and *pro\_ele\_list\_FLOW*.

```

./INPUT/param'          ! I_unit 11 : parametri simulazione
./INPUT/solver_FLOW_PIC' ! I_unit 12 : parametri solutore per il flusso
./INPUT/solver_TRAN'    ! I_unit 13 : parametri solutore per il trasporto
./INPUT/coord'          ! I_unit 14 : coordinate
./INPUT/topol'          ! I_unit 15 : topologia
./INPUT/mat_SOIL'       ! I_unit 16 : materiali per il terreno
./INPUT/mat_FLOW'       ! I_unit 17 : materiali per il flusso
./INPUT/mat_TRAN'       ! I_unit 18 : materiali per il trasporto
./INPUT/tablist_SOIL'   ! I_unit 19 : lista tabelle per il flusso
./INPUT/ic_FLOW'        ! I_unit 22 : condizioni iniziali per il flusso
./INPUT/ic_TRAN'        ! I_unit 23 : condizioni iniziali per il trasporto
./INPUT/bcdir_FLOW'     ! I_unit 24 : bc dirichlet per il flusso
./INPUT/bcneu_FLOW'     ! I_unit 25 : bc neumann per il flusso
./INPUT/bcspg_FLOW'     ! I_unit 26 : bc seepage per il flusso
./INPUT/bcatm_FLOW'    ! I_unit 27 : bc atmosf per il flusso
./INPUT/bcdir_TRAN'     ! I_unit 28 : bc dirichlet per il trasporto
./INPUT/print_time_FLOW' ! I_unit 30 : lista tempi per stampe per il flusso
./INPUT/print_time_TRAN' ! I_unit 31 : lista tempi per stampe per il trasporto
./INPUT/print_vol_FLOW' ! I_unit 32 : lista nodi per stampe di volumi per il flusso
./INPUT/print_list_nod_FLOW' ! I_unit 34 : lista nodi per stampe soluzione per il flusso
./INPUT/print_list_nod_TRAN' ! I_unit 35 : lista nodi per stampe soluzione per il trasporto
./INPUT/print_list_ele_FLOW' ! I_unit 36 : lista nodi per stampa proprietà per il flusso

./OUTPUT/debug'        ! O_unit 51 : debug
./OUTPUT/hw_nod'       ! O_unit 52 : carico di pressione ai nodi
./OUTPUT/hw_ele'       ! O_unit 53 : carico di pressione sugli elementi
./OUTPUT/c_nod'        ! O_unit 54 : concentrazione normalizzata ai nodi
./OUTPUT/c_ele'        ! O_unit 55 : concentrazione normalizzata sugli elementi
./OUTPUT/vol_FLOW'     ! O_unit 56 : flussi e volumi per il flusso
./OUTPUT/pro_ele_FLOW' ! O_unit 58 : proprieta' sugli elementi per il flusso
./OUTPUT/hw_nod_list'  ! O_unit 60 : carico pressione su lista nodi
./OUTPUT/c_nod_list'   ! O_unit 61 : concentrazione normalizzata su lista nodi
./OUTPUT/pro_ele_list_FLOW' ! O_unit 62 : proprieta' sugli elementi della lista

```

Figure 3.1 The *gw.fnames* file with inputs and outputs of GWS.

### 3.4.1. Input files

Knowing the material properties of the system we want to model, it is possible to distinguish the material types with a constitutive law id (*id\_law*), integer material parameters (*iparam*) and real material parameters (*rparam*) in three different files: *mat\_SOIL*, *mat\_FLOW* and *mat\_TRAN*. In the first file, the integer parameter is *itab*, that is the index of the table containing the values of the functions  $\text{cms} = \text{cms}(d)$ ,  $\text{cms} = \text{cms}(sz)$  and  $\text{sz} = \text{sz}(d)$ , where *cms* is the material compressibility, *d* is the depth and *sz* is the vertical (effective) stress. In other words, these functions are the compressibility variation with depth and vertical stress and the vertical stress variation with depth,

respectively. In the *tablist\_SOIL* file, there is a link to another file called *depth\_cms\_sigeff.tab* or *markers.tab* in the *tab* directory where the three-column tables are listed (the first column is for the depth, the second is for the compressibility and the third is the vertical stress). It is important to always assign a variation of compressibility and stress between two consecutive values (depths), even a small one if we want to impose a constant value, considering that the compressibility decreases and the stress increases with depth. This is because the code does a linear interpolation between them and if the difference goes to zero, it has a zero as denominator. Then, there are four real material parameters in *mat\_SOIL*: *fac\_cms0* (a multiplicative coefficient), *ocr0* (initial over-consolidation factor,  $\geq 1$ ), *cr* (the ratio between the compressibility in virgin loading and unloading condition,  $\geq 1$ ) and *tol*. The initialization algorithm for each element works like this:

- 1) the material assigned to the element is identified
- 2) the table assigned to the material (*itab*) is identified
- 3) the element depth (*d*) is computed
- 4) the maximum stress  $sz\_max = sz(d) \times ocr0$  is assigned
- 5) the initial compressibility is assigned according to the *ocr0* value:
  - if  $ocr0 = 1$ ,  $cms0 = cms(d) \times fac\_cms0$
  - if  $ocr0 > 1$ ,  $cms0 = cms(d) \times fac\_cms0/cr$

The material can also have mechanical hysteresis. Being *sz\_curr* the current vertical stress, we have two phases during the simulation:

- 1) virgin loading phase:  $sz\_curr = sz\_max$ ,  $cms = cms(d) \times fac\_cms0$
- 2) unloading-reloading phase:  $sz\_curr < sz\_max + tol$ ,  $cms = cms(d) \times fac\_cms0/cr$

The material is linear elastic in both phases, but it has different stiffness. Therefore, specific elastic storage is quantified accordingly.

In *mat\_FLOW*, we set the number of materials that we consider in our flow problem and for each of them the constitutive law *id* (=1 if the condition is saturated and =2 if unsaturated) and real material parameters such as the hydraulic conductivity in *x*, *y* and *z* directions (*kx*, *ky* and *kz*) and porosity (*poros*). If the condition is unsaturated, we are also asked to insert the van Genuchten parameters  $\alpha$ ,  $n$  and  $\theta_r$  (*vga*, *vgn* and *swr*), whereas *l* is set equal to 0.5 by default.

*Mat\_TRAN* is similar to *mat\_FLOW*, but there is only one constitutive law *id* (1) and the physical parameters to provide are the longitudinal and transversal dispersivity (*aL* and *aT*), molecular diffusivity (*DO*) and tortuosity (*tau*).

*Solver\_FLOW\_PIC* and *solver\_TRAN* contain the parameters for the solver of the flow and transport like the maximum number of iterations, the exit tolerance of the iterative scheme used to solve the linear system of equations, the type of preconditioner and a link to its parameters (given in another file in the *prec* directory).

The topology of the grid is given by two separate files: *coord* and *topol*. The first one contains the number of nodes in the first row, followed by a list with four columns: node number in ascending order and the  $x$ ,  $y$  and  $z$  coordinates for each node. In *topol*, at first there is the total number of elements and from the second row onwards there are the element numbers in ascending order and for each element there are the number associated to four element properties and four nodes representing its vertices (in case of tetrahedral elements). The four element properties are in order: the element type and the numbers corresponding to the material for soil, flow and transport.

Initial conditions are set through the *ic\_FLOW* and *ic\_TRAN* files, where pressure and concentration values, respectively, are imposed at the start of the simulation for each mesh node in one column with a fixed format. These values are essential for solving the governing equations in transient simulations and not for the steady-state simulations (independent from initial conditions), but from a numerical point of view, setting initial conditions that are reasonable or as close as possible to the steady ones can help the convergence.

Boundary conditions are distinguished in *bcdir\_FLOW*, *bcdir\_TRAN*, *bcneu\_FLOW*, *bcatm\_FLOW* and *bcpsg\_FLOW*. The first two files allow to impose Dirichlet conditions to selected nodes in different times starting from  $t = 0$ . Even in this case, it is necessary to respect a fixed format. For a general idea, a typical file starts with the time value, followed by the number of Dirichlet nodes, the list of all nodes in ascending order written in five columns and the list of the corresponding values (pressure for flow and concentration for transport) again written in five columns. *Bcneu\_FLOW* and *bcatm\_FLOW* are both Neumann conditions, but the atmospheric conditions depend also on pressure head and they have been recently added. In the original GWS version, every inflow or outflow condition into/from the simulated domain must be imposed as a Neumann condition in *bcneu\_FLOW*. The modification was introduced to avoid that the pressure head ( $hw$ ) at the Neumann nodes becomes too low or too high. This is done through the so-called atmospheric conditions *bcatm\_FLOW* that allow to prescribe limit values  $minhw$  and  $maxhw$ . The values of these variables are set in the *param* file. From the numerical point of view, it is a boundary condition varying with the solution. The nodes on the “atmospheric surface” can have three states according to the pressure head:

- 1) if  $minhw < hw < 0$ , Neumann conditions are imposed
- 2) if  $hw < minhw$ , Dirichlet conditions are imposed ( $hw = minhw$ )

3) if  $hw > 0$ , Dirichlet conditions are imposed ( $hw = 0$ )

*Bcatm\_FLOW* and *bcneu\_FLOW* conditions have the same physical meaning (they are flow rates) and the files have the same format of the Dirichlet conditions files. Finally, *bcspg\_FLOW* imposes atmospheric pressure on selected nodes in a fixed format (number of nodes and list of nodes in five columns with specific spaces to be respected).

There are also several files for parameter printing: *print\_time\_FLOW*, *print\_time\_TRAN*, *print\_list\_nod\_FLOW*, *print\_list\_nod\_TRAN*, and *print\_list\_ele\_FLOW*. The first two files are used to impose, for the flow and transport solution, respectively, the number of times and the list of times to print. A logical variable must also be provided to the right of the number of times depending on whether we want the solution of the pressure/concentration on the nodes and/or on the elements and the solution of the properties (water saturation) on the elements. The last three files are also a recent modification of the simulator and they allow us to print the solution for each time-step on a list of nodes (for pressure and concentration) and elements (for water saturation) at the user's choice. These files contain the total number of nodes/elements chosen and the list of nodes/elements in a single column.

The *param* file contains the simulation parameters such as: the non-linear scheme for flow and transport (Picard or Newton scheme), the maximum number of iterations for the non-linear scheme (*NL\_itermax*), the convergence criterion for the non-linear scheme (*NL\_iconv*), the exit tolerance of the non-linear iterative scheme (*NL\_tol*), the number and the list of time steps (*ndeltat* and *deltat*), the minimum time step (*mintstep*), the water compressibility (*cmw*), the volume weight of water (*volwew*), limit values of pressure head for *bcatm\_FLOW* (*minhw* and *maxhw*), and the density and viscosity ratios (*epsilon\_den* and *epsilon\_vis*). Changing the convergence criterion, reducing the minimum time step, and increasing the exit tolerance (to some extent) are some valuable options to help achieving solution convergence in certain cases. There are also some logical variables imposing, for example, a coupled solution instead of solving only the flow or the solution with total pressure head instead of pressure head increment (without the gravitational term). According to the option chosen, the initial and Dirichlet conditions must be coherently defined.

### 3.4.2 Output files

The output files generated by GWS using the *gw\_simulator* executable. A properly working simulation prints its progress as output on the screen. Specifically: opening of files, reading of data

input, model initialization (elements, materials, boundary conditions) and the start of time-step loop. For every step, information about the previous, current and next time is given together with the current time step and the convergence profile. If convergence is reached within the maximum number of iterations set in the *param* file, the simulation proceeds to the next time step, otherwise it backsteps reducing the time step of a given factor and tries again until it reaches the convergence or the minimum time step (also set in *param*) and, in this last case, an error appears on the screen.

As already mentioned in the previous paragraph, according to the specifications set in the input files, it is possible to obtain the solution in terms of pressure and concentration on the nodes (*hw\_nod* and *c\_nod*) or on the elements (*hw\_ele* and *c\_ele*) and the solution of water saturation on the elements (*pro\_ele\_FLOW*) for the chosen times to print. Moreover, the three variables are print on a few selected nodes and elements (*hw\_nod\_list*, *c\_nod\_list* and *pro\_ele\_list\_FLOW*) for all the time steps.



## Chapter 4

# Application to a schematic case study

---

### 4.1 3D mesh generation

Since the complexity of the model to develop, a preliminary study was carried out on a simplified model to gain confidence with GWS and the processes and parameters involved in the case study.

Domain geometry is the starting point to develop the computational model. In the schematic model, the considered domain is 300 m long, 150 m wide and 10 m deep and rotated 10° clockwise. It is crossed by a channel 30 m wide, located at 50 m from the closest boundary, representing the “lagoon side”. The ground level of the area together with the channel is considered -2 m below msl. Moreover, a 5-m thick outcropping sandy paleochannel (from the land surface to -7 m below msl) is supposed to cross the domain, which is assumed to be made of clayey silt (Figure 4.1).

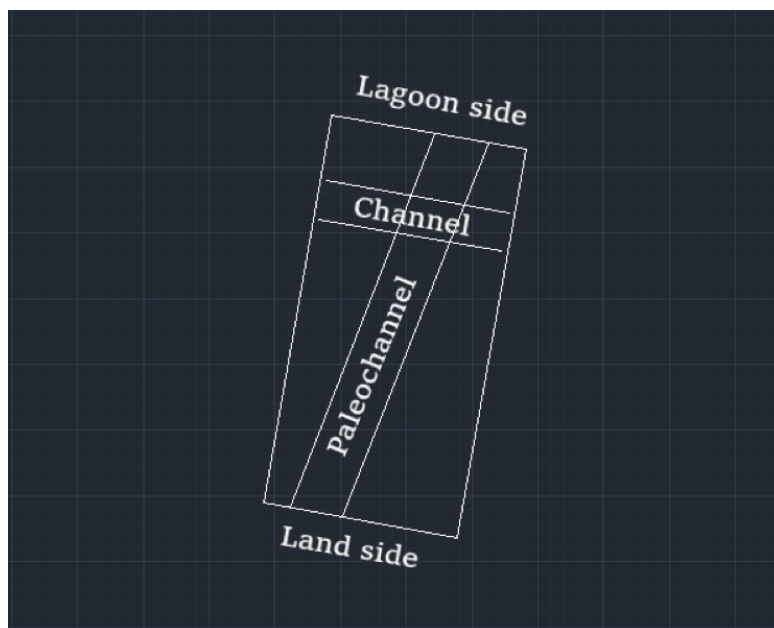


Figure 4.1 The schematic case study.

At first, the model domain was defined using AutoCAD and then imported in the software Argus ONE to generate the 2D mesh in  $x$ - $y$  plane. A discretization in triangular finite element mesh was developed, accounting for the two soil types, with the bounds roughly located along the paleochannel contours. The triangular mesh was created with a greater density nearby the channel, with a grid resolution of 4 m (given that the greatest hydraulic gradients and variations are expected to take place in this area), whereas the cell size is of 10 m far from the channel. A coarse mesh is considered in this first analysis to make the computation easier and faster.

Subsequently, the 2D mesh is extruded along the  $z$  direction through the three-dimensional mesh generation program GEN3D. For this purpose some input files were given containing information related to: the 2D mesh (such as nodes, coordinates, elements and index of materials); the Dirichlet nodes; the coordinates of the nodes of the domain surface and the surfaces at -7 and -12 m below msl; the two geological layers, each 5 m thick, subdivided in smaller layers, and the number and location of materials (clayey silt and sand in the first geological layer and clayey silt below). The 3D mesh and the three materials are shown in Figure 4.2. The whole domain is divided in 10 horizontal layers, denser close to the surface (of major interest), and with an increasing thickness with depth. The 3D mesh thus obtained is made up of 12265 nodes and 63480 tetrahedral elements.

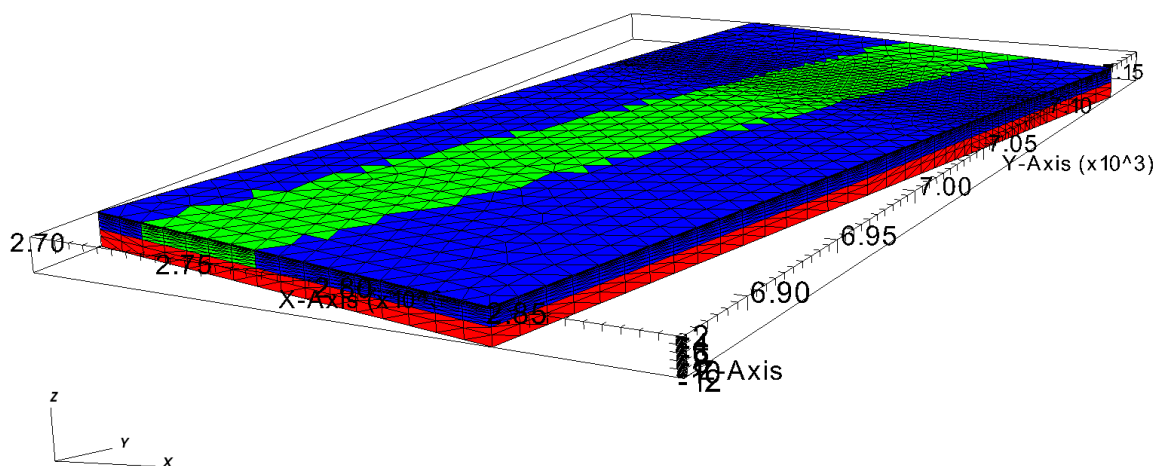


Figure 4.2 3D mesh of the schematic model with the three materials coloured with different colours (sand in green and clayey silt in blue and red).

## 4.2 Modelling set-up

Several test simulations with different conditions were carried out to become familiar with GWS in this initial phase, including a sensitivity analysis as presented in the following.

The programming platform Matlab was used to create some input files through scripts, for instance to impose boundary and initial conditions for the flow and transport equations. A hydrostatic pressure distribution was imposed by using Dirichlet conditions on the nodes along the land and lagoon side boundaries of the domain. Here, the water table is set at -7 m below msl and of -4 m below msl, respectively, with pressure heads increasing linearly with depth. No-flow conditions are prescribed on the bottom, the other two lateral boundaries and the upper boundary, where it is supposed that precipitation and evapotranspiration are balanced. A steady-state simulation was initially run, and the solution thus obtained was used as initial conditions for the transient analyses. As concerns the transport equation, initial conditions corresponding to relative salt concentration are assumed equal to 1 everywhere in the domain. So, the concentration value is normalized respect to the maximum value assumed, that is the concentration of salt in seawater.

Transient simulations are carried out prescribing a Neumann condition on the nodes corresponding to the channel bottom where a recharge due to the river water is considered. A very high uniform recharge of 0.04 m/day is assumed to favour the dynamics, whereas the flux is kept null for the other nodes on the model surface. Moreover, the Dirichlet conditions in terms of concentration are set constant and equal to 1 for the nodes on the lagoon and land side boundaries of the domain and null at the nodes corresponding to the channel, where a freshwater recharge is assumed. The simulations span a time of 365 days.

Given that in the first phase of the study simulations were performed on a schematic model, the parameters used for flow and transport are typical values of coastal soils. Moreover, even if the distinguished materials are three, as explained in the previous paragraph, for simplicity the properties are considered equal for the two clayey silt soils, ending up with only two materials (clayey silt and sand).

The sensitivity analysis was performed to assess how flow and transport are affected by changes in hydraulic conductivity and dispersivity, respectively. The van Genuchten parameters (except for  $K_s$ ) are assumed to be the same for all materials and are reported in Table 4.1.

Table 4.1 van Genuchten Parameters used in the sensitivity analysis.

$\varphi$	0.3
$\theta_r$	0.1
$\alpha$ (1/m)	0.5
$n$	3

As to the flow parameters, the saturated hydraulic conductivity is assumed isotropic. Three cases are investigated, including a homogeneous case and other two cases with an increasing  $K_s$  difference of between the two materials (Table 4.2).

Table 4.2 Saturated hydraulic conductivity investigated in the sensitivity analysis.

Material type	$K_s$ [m/day]		
	Case 1	Case 2	Case 3
Clayey silt	10	0.1	0.02
Sand	10	10	50

No available data about transport parameters are available in the study area. Therefore, for simplicity only one material type is considered for the transport model, with  $D_0 = 0.1 \text{ m}^2/\text{day}$  and  $\tau = 1$  for all cases and different values of  $\alpha_L$  and  $\alpha_T$  (Table 4.3).

Table 4.3 Longitudinal and transversal diffusivity investigated in the sensitivity analysis.

	Case 4	Case 5	Case 6
$\alpha_L$ (m)	10	5	50
$\alpha_T$ (m)	1	0.5	5

The diffusivity coefficients were varied keeping a ratio of 1:10 between the longitudinal and the transversal values. The sensitivity on  $\alpha_L$  and  $\alpha_T$  is carried out using the flow parameters of case 2.

### 4.3 Results

The simulation results are visualized with VisIt, an open-source software to visualize scalar and vector fields defined on 2D and 3D structured and unstructured meshes. The dimension along the  $z$  direction is scaled by a factor of 5 to improve the clearness of the flow and transport dynamics.

Figure 4.3 and 4.4 show the pressure head distributions at intermediate and final times (i.e. after 75 and 365 days). For the homogeneous case, no significant changes are visible due to the high permeability allowing the water to easily flow through the porous medium. The maximum and minimum values of pressure remain almost the same and there is only a slight increase of pressure, and therefore a rise of the water table, in the vicinity of the channel where freshwater recharge is forced. On the contrary, in cases 2 and 3 the maximum pressure increases significantly, reaching values up to 30 and 80 m after 365 days, respectively, in correspondence of the clayey silt. The large pressure is obviously unphysical but is considered acceptable for this simplified test model. Moreover, by comparing the two heterogeneous cases, in the case 3 there is a clearer separation between high- and low-pressure zones on the surface in correspondence of the channel. Even along the paleochannel, it is possible to notice a higher pressure increase for case 2 with respect to case 3 due to the lower permeability of the former than that of the latter.

Similar considerations can be done by analysing the saturation results. In Figure 4.5 and 4.6, it is evident how the water table rises slightly in case 1 and notably in the other cases with the red portions (corresponding to saturation equal to 1) moving upward and towards the land side (low-pressure zones). It is worthful to note that the portion of the channel crossed by the paleochannel in case 3 remains unsaturated after 365 days compared to case 2, due to a higher permeability by a factor of 5.

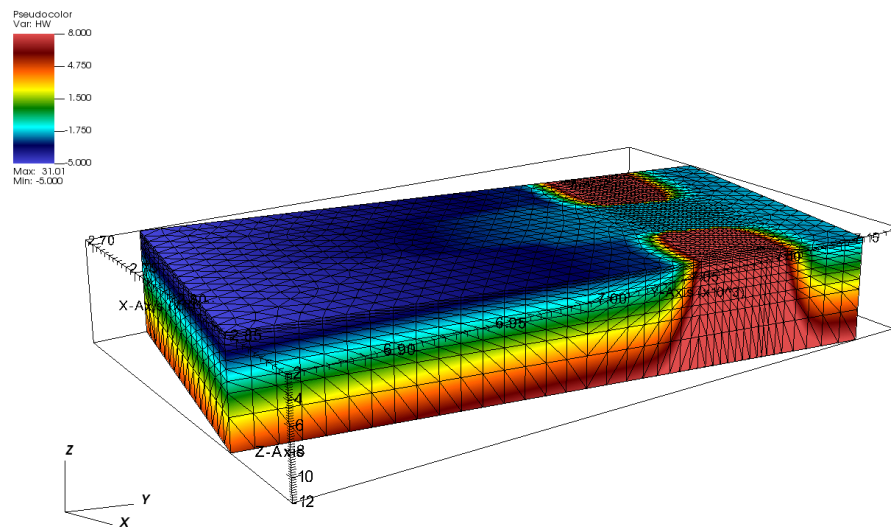
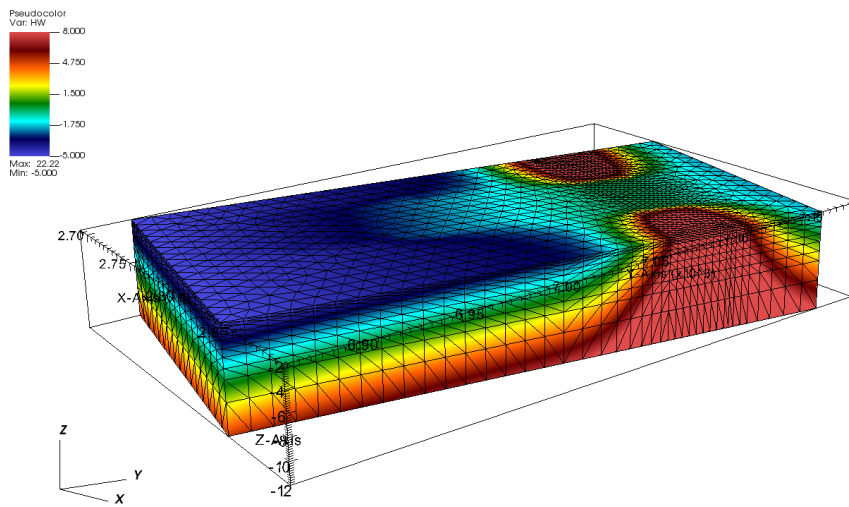
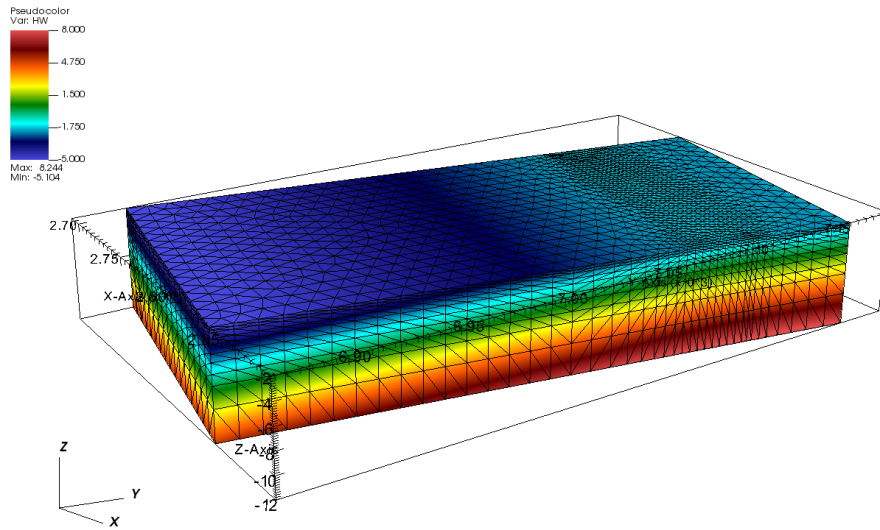
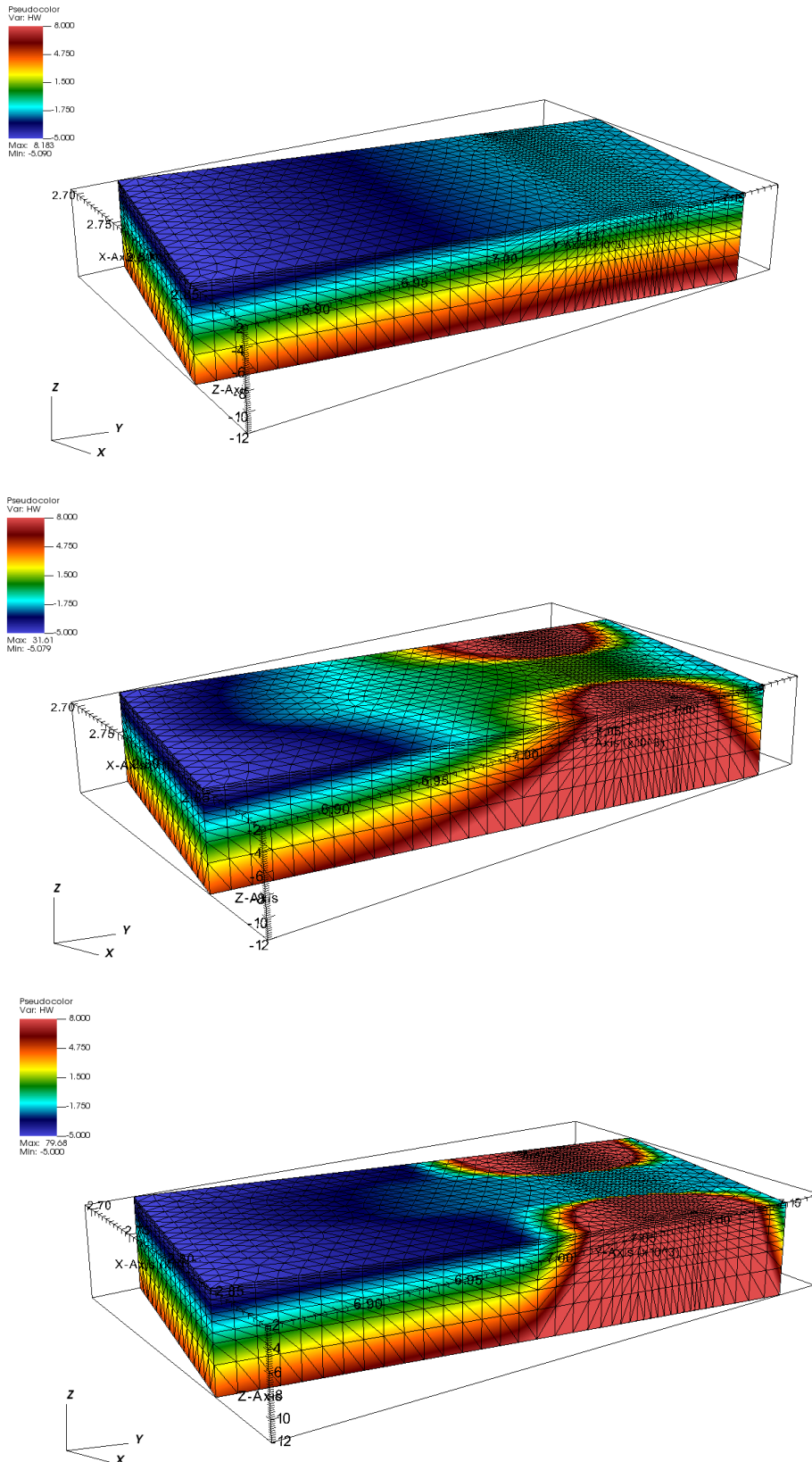
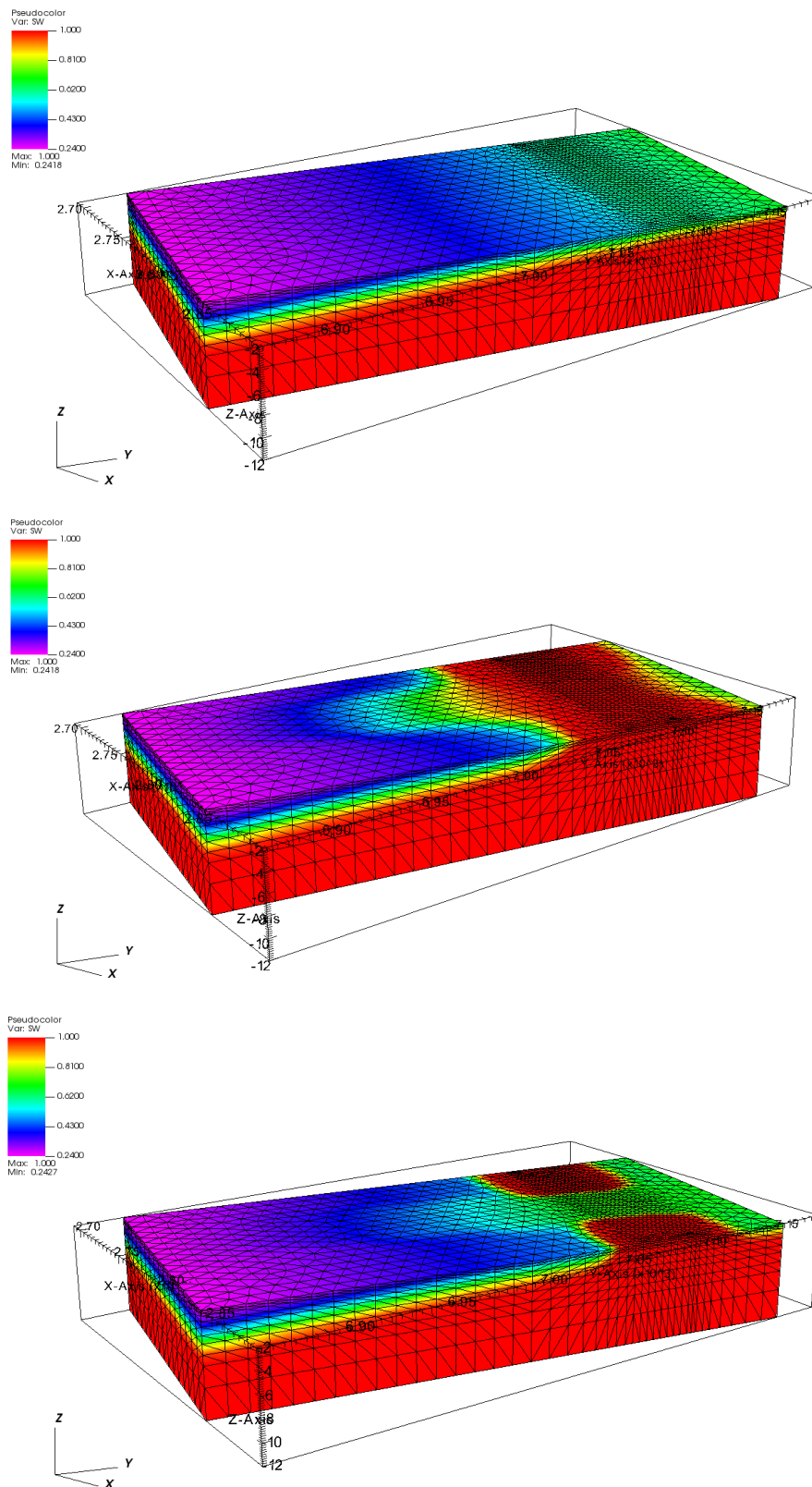


Figure 4.3 Pressure head after 75 days for cases 1, 2 and 3 (from top to bottom). Vertical exaggeration is 5.



*Figure 4.4 Pressure head after 365 days for cases 1, 2 and 3 (from top to bottom).  
 Vertical exaggregation is 5.*



*Figure 4.5 Saturation after 75 days for cases 1, 2, and 3 (from top to bottom). Vertical exaggeration is 5.*



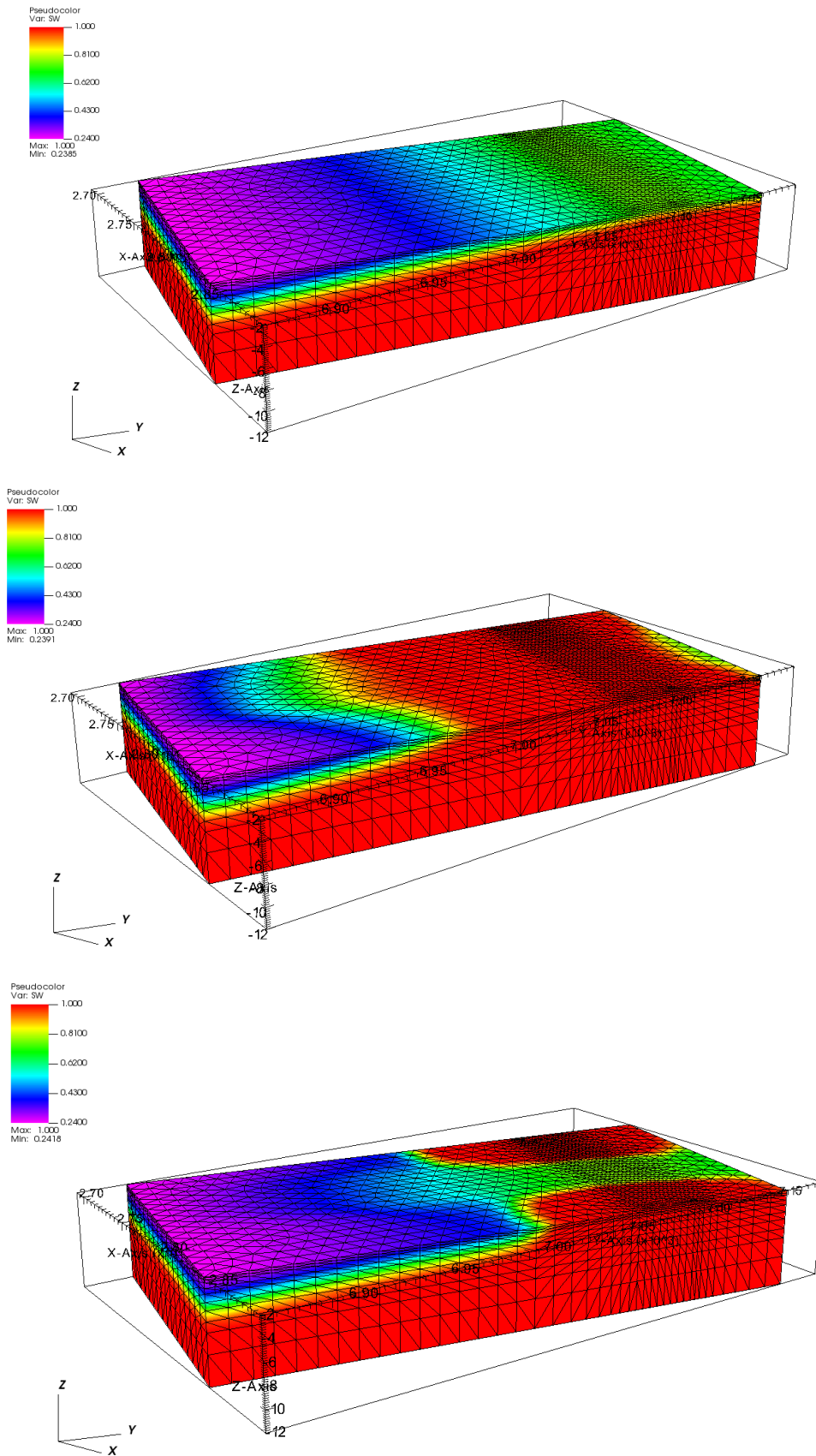
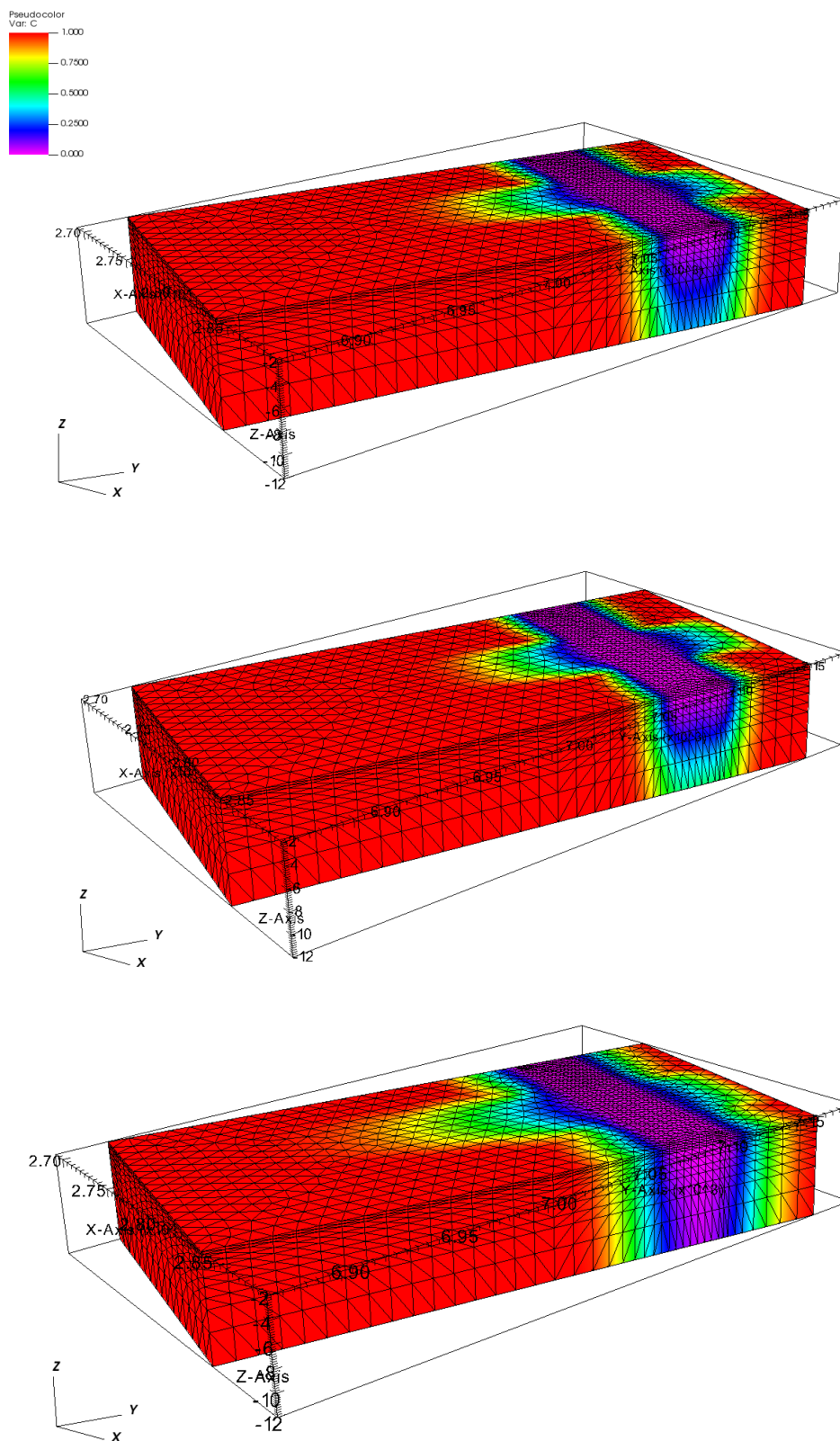


Figure 4.6 Saturation after 365 days for cases 1, 2 and 3 (from top to bottom).  
 Vertical exaggeration is 5.

As concerns the results provided by the transport model, again the outcomes are showed after 75 and 365 days (Figure 4.7 and 4.8). The model computes how the freshwater recharged from the riverbed propagated along the paleochannel. The results for case 6 clearly show the effects of higher dispersivity coefficients, with lower concentration gradient and with concentration equal to zero at the bottom of the domain below the channel already after 75 days, differently from the other two cases. Differences in transverse dispersion are also visible for the three cases, especially along the paleochannel where the “tongue” of less saline water is wider for case 6, due to higher transversal dispersivity coefficient. Differences between cases 4 and 5 are also evident for instance for the concentration distribution after 75 days at the bottom of the vertical face in correspondence of the channel: the downward movement of freshwater has a greater effect for case 4, reaching concentrations of about 0.2 compared to a value of about 0.4 for case 5.



*Figure 4.7 Concentration after 75 days for cases 4, 5 and 6 (from top to bottom). Vertical exaggeration is 5.*

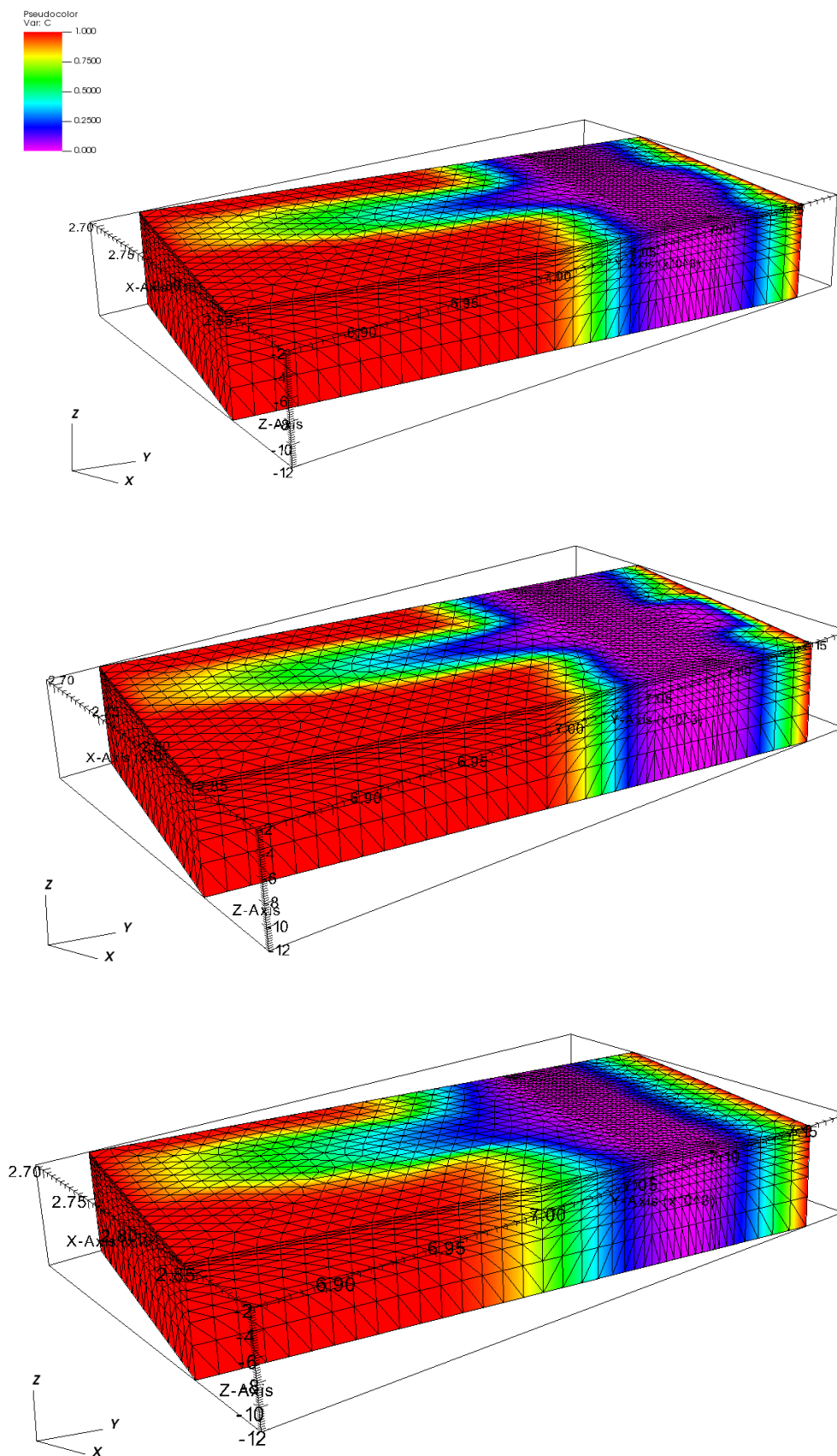


Figure 4.8 Concentration after 365 days for cases 4, 5 and 6 (from top to bottom). Vertical exaggeration is 5.

## Chapter 5

# Model application on the Ca' Pasqua study area

---

### 5.1 Introduction

The GWS simulator has been applied to the study area near Ca' Pasqua corresponding to the zone detected by the red box in Figure 2.2-left. The aim of the simulations is to anticipate the possible effect on the salt concentration of the drain established in Autumn 2020 along the paleochannel crossing the farmland from southeast to northeast (blue alignment in Figure 2.2-left). Unfortunately, only a short-time test of functioning was carried out with the drain after its establishment to check the functioning, but no monitoring activity has been carried out until now. Therefore, only a number of preliminary simulations have been developed in this work because a specific calibration will be possible from next Spring only when the drain will be put in operation and a specific monitoring network will be established in its surrounding. Here, the natural dynamics of the phreatic aquifer system has been reproduced based on data on the water quality in the waterbodies bounding the farmland northward and the effective evapotranspiration obtained by a previous modelling study aimed at calibrating a 1D vertical groundwater flow model in the shallowest 1-m thick soil.

### 5.2 Model geometry and set-up

The geometry of the final domain was realized starting from the identification of the 2D domain using a Landsat satellite image of the study area, the location of the recharge drain and paleochannels crossing the farmland, the main watercourses and their embankments, and the ditches used to keep drained the area. All these elements were accurately represented in the grid. The area was selected sufficiently large both in the direction parallel and orthogonal to the main groundwater

flow to avoid that the boundary conditions significantly affect the simulation in the area of major interest, i.e. the field crossed by the recharge drain.

The 2D mesh was created through ArgusOne. A very fine grid resolution equal to 0.25 m was prescribed along the drain and the ditch close to the southern border of the domain, where high gradients of pressure, saturation and concentration are expected to develop. The resolution in the rest of the domain was set to a maximum characteristic dimension equal to 4 m to balance the contrasting needs of reducing the elements deformation and, at the same time, keeping the computational burden to an acceptable level. Different zones were distinguished for rivers, channel, paleochannel, levees, ditch and drain to have a greater degree of freedom for parameters setting.

In relation to the vertical direction, the ground elevation was defined using a digital map of the area developed in Manoli et al. (2015). Some points were also added manually to have a more detailed description in specific areas. An elevation equal to 1 m above msl was assumed for the levees between the Morto channel and the Brenta river. Subsequently, the 2D mesh was extruded along the  $z$  direction. The final 3D mesh consists of 571'619 nodes and 3'203'288 tetrahedral elements (Figure 5.1). A 3D view of the mesh is shown in Figure 5.2 with colours representative of the elevation above the msl. A total of 19 materials were assigned according to the soil stratigraphy (Figure 5.3). For the purpose of this thesis, only the most superficial part of the phreatic aquifer up to -12 m below msl (above the Caranto unit) was analyzed. The vertical element dimension ranges between 0.1 m close to the land surface and 2 m in the deeper 6 m. The recharging drain was represented by a 0.25 m tube running along the actual trace at a depth of 1.5 m from the land surface.

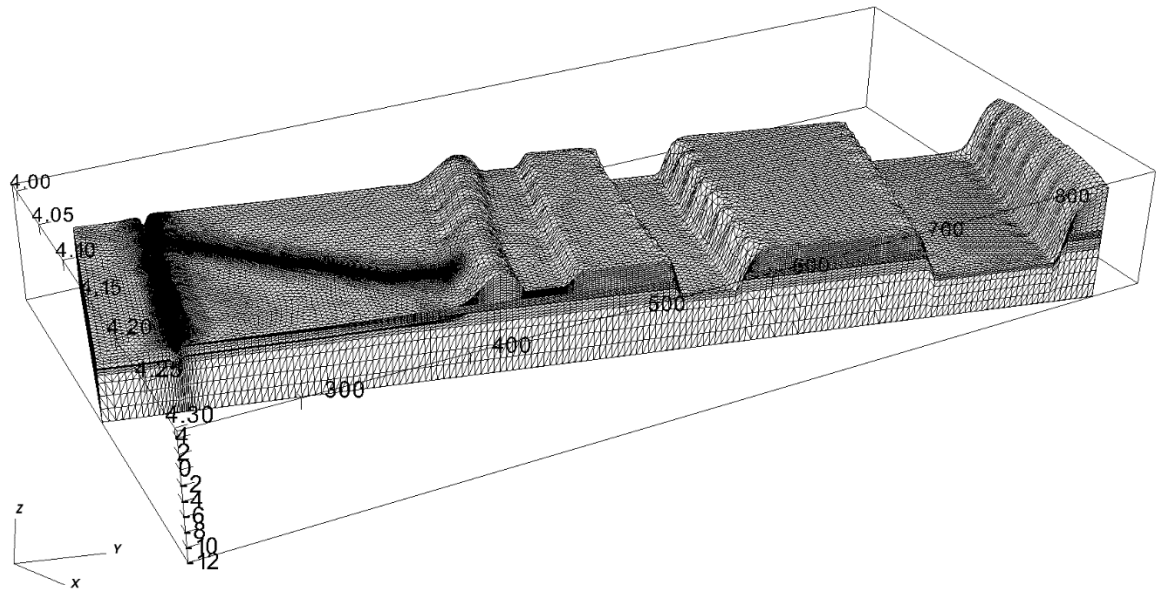


Figure 5.1 The 3D mesh. Vertical exaggeration is 5.

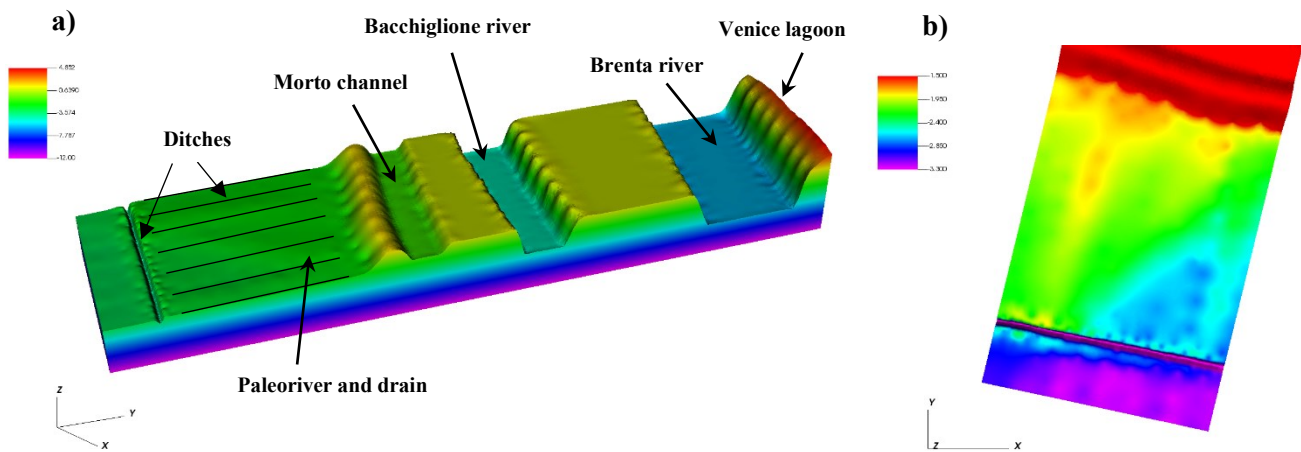
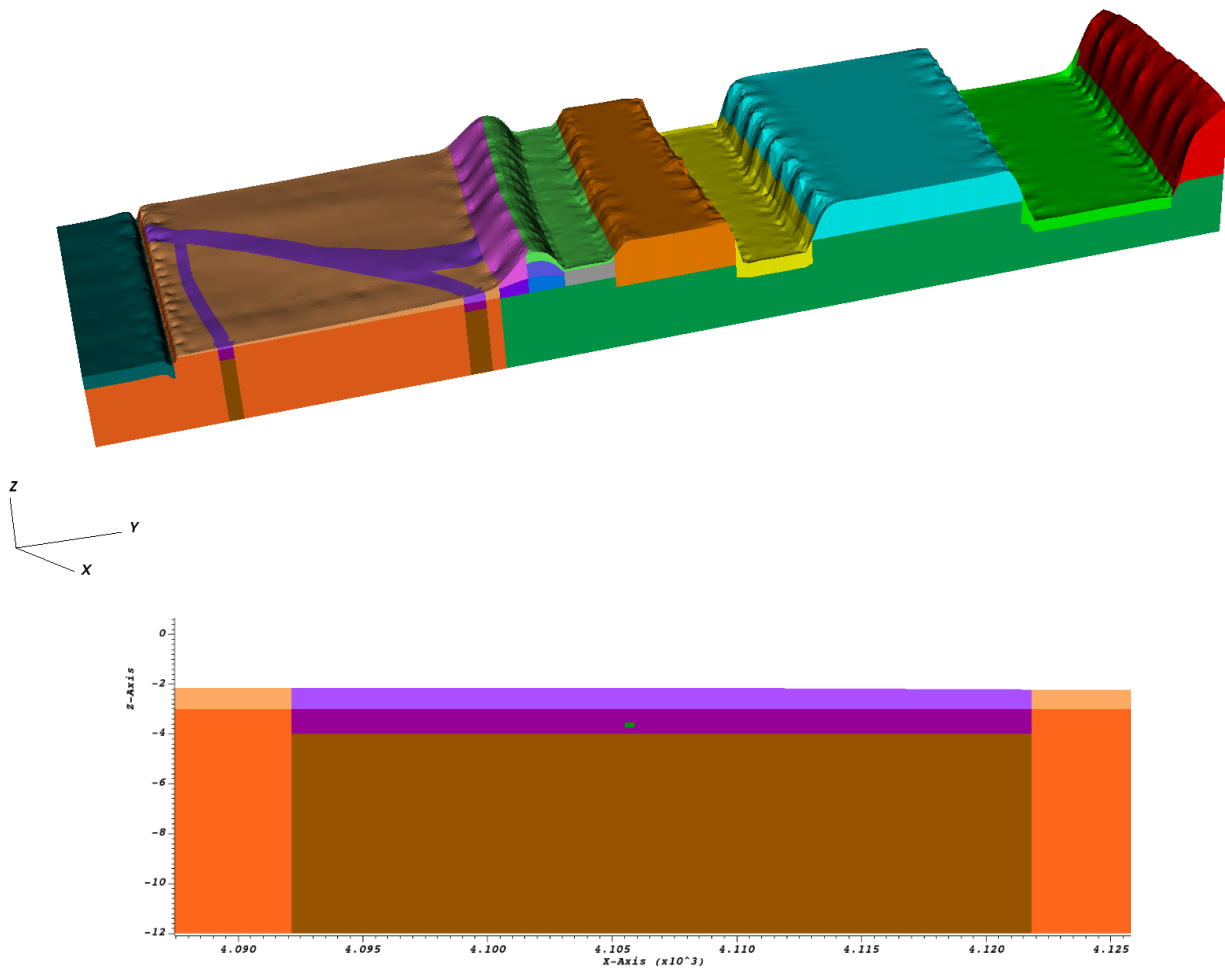


Figure 5.2 a) The simulated domain with the colours representing the elevation in m above msl. Vertical exaggeration is 5; b) Detail of the farmland surface with the colours representing the elevation in m above msl.

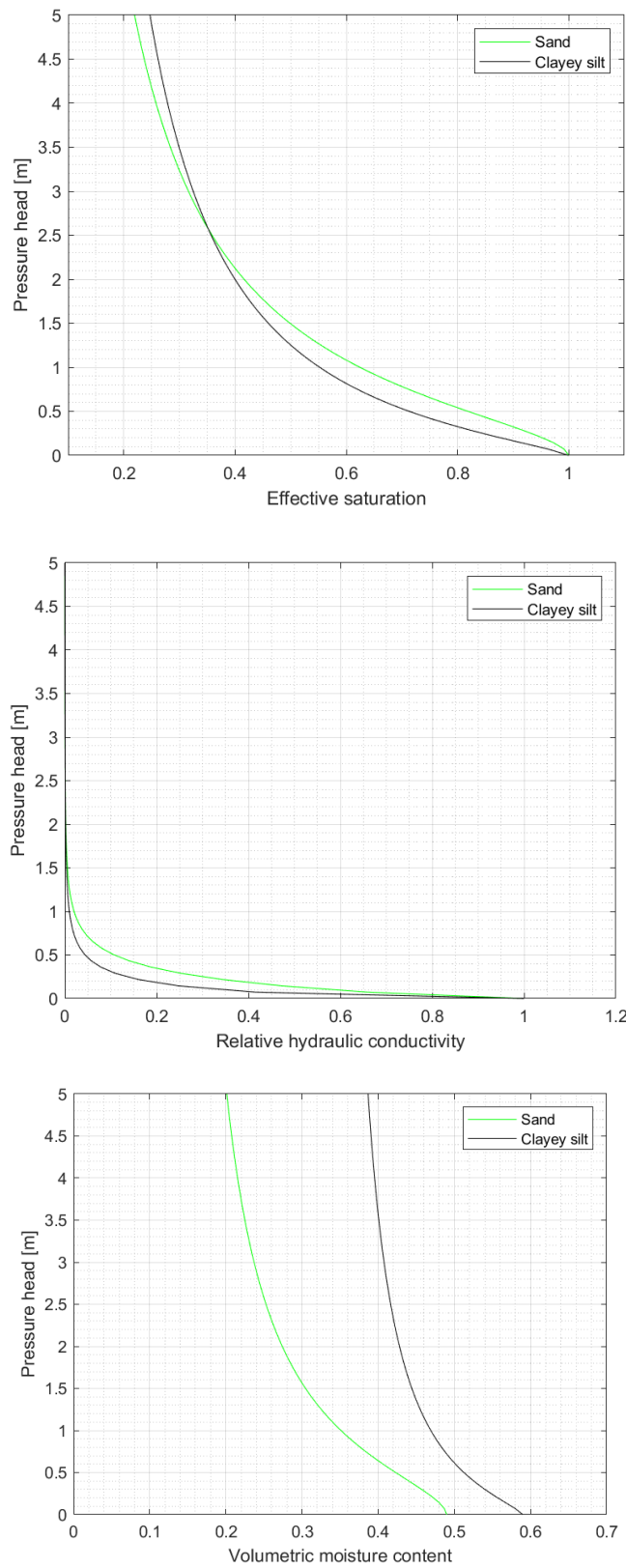


*Figure 5.3 The 19 materials highlighted with different colours (above and below) with a vertical section in the middle of the farmland (below) showing the location of the drain material (in green) at about 1.5 m below the ground level. Vertical exaggeration is 5 (above).*

The model does not include mechanical hysteresis and thus there are not compressibility variations since no large depths and pressure variation are considered.

The parameters for the flow model were appropriately chosen based on the soil type. As regards the van Genuchten parameters, by comparing the available data reported in Table 2.1 and Table 2.2, parameters from the laboratory tests were considered the most representatives and, for simplicity, the same values were applied to all sand-like materials and the others were considered clayey-silt-like materials. Figure 5.4 shows the van Genuchten relationships in terms of pressure head vs effective saturation, pressure head vs relative hydraulic conductivity, and pressure head vs volumetric moisture content for sand and clayey silt. Notice that capillary pressure and pressure head coincide (in term of absolute value). Porosity is set equal to 0.25 for clayey silt and 0.5 for sand.





*Figure 5.4 Van Genuchten retention curves for sandy and clayey-silty soils according to the laboratory data provided in Table 2.1.*

Several combinations of hydraulic conductivity values for the different materials were considered to better reproduce the physical conditions observed in the field by the model. Isotropic and vertical anisotropic conditions for the saturated hydraulic conductivity were simulated. A summary of the investigated  $K_s$  values is provided in Table 5.1. Notice that the recharging drain was characterized using a material with a very high  $K_s$  value: this strategy resulted simpler than removing the finite elements representing the tube from the 3D grid.

*Table 5.1 Ranges of hydraulic conductivity for the different materials used in the numerical model.*

<b>Material classification</b>	<b><math>K_s</math> (m/day)</b>
Levees	0.0001-0.004
Watercourse beds	0.0001-0.002
Farmland (outside the paleochannel)	0.05
Paleochannel	0.5
Aquifer	2-10
Drain	200

For the anisotropic case the permeability values along the  $z$  direction are reduced by a factor of 5 with respect to the corresponding value for the  $x$  and  $y$  directions, except for paleochannel and superficial farmland where  $K_{s,z}$  was set equal to 0.3 and 0.03 m/day, i.e. an anisotropic factor equal to 1.5 was used. Specific information of this topic is unavailable. However, a higher value should cause an excessive saturation of the shallowest soil during rainfall events.

Since no data are available to characterize the transport parameters, a sensitivity analysis was initially carried out and, finally, a homogeneous material was assumed for the transport model using the parameters values reported in Table 5.2, in agreement with previous studies.

*Table 5.2 Solute transport parameters.*

$\alpha_L$ (m)	0.1
$\alpha_T$ (m)	0.01
$D_0$	0.0001
$\tau$	200

## 5.3 Model results

The modelling activity was carried out in three phases:

- 1) steady state analysis for model initialization;
- 2) transient analysis (yearly scale) to investigate the effect of the main natural factors forcing the system dynamics, i.e. the effective precipitation and parameter fluctuation in the watercourses, using the output of simulation (1) as initial conditions;
- 3) transient analysis (weekly to monthly scale) of the effects of the recharging drain using the outcome of simulations (2) as initial conditions.

### 5.3.1 Model initialization

Initially, a steady state analysis was carried out. The goal was to characterize “on the average” the subsurface flow and salt distribution in the study area.

The boundary conditions were prescribed as follow. A hydrostatic pressure head was imposed at the land side and the lagoon side boundaries with the water table at -4 m above msl and 0 m above msl, respectively. The prescribed pressure distribution considers the different water specific weight due to salt concentration. Concentrations were set equal to 1 on the lagoon boundary and varied with depth from 0.1 at the land surface to 0.8 at the model bottom with a sigmoidal function on the land side boundary. Water levels were set constant and equal to 0 m and 1 above msl in the Morto channel and the Bacchiglione and Brenta rivers, respectively. The relative concentration in the Morto channel and the Bacchiglione and Brenta rivers were also set constant and equal to 0.04, 0.6 and 0.9, respectively, in this initial phase. Seepage face conditions were prescribed along seven ditches crossing the farmland from south-west to north-east conveying the drainage water to the main southern ditch (parallel to the main watercourses), which is finally connected to the pumping station. These latter ditches were not explicitly represented in the digital elevation model (conversely to the southernmost ditch) but were represented through a row of vertical nodes down to a 1 m depth from the ground surface. This simplification allowed to simulate the presence of the drainage channels without increasing even more the grid complexity and, consequently, the number of elements and nodes. No flow and salt concentration gradient were imposed on the model bottom, the farmland surface (i.e., precipitation almost equates evapotranspiration), and on the south-west to north-east vertical boundaries.

Figures 5.5, 5.6 and 5.7 show the steady state model outcomes in terms of pressure head, water content, and relative salt concentration, respectively. The problem is almost bi-dimensional, with the parameters that remain practically constant in the direction parallel to the watercourses. Figure 5.5 shows the pressure head distribution: a certain hydraulic gradient develops from the lagoon side to the landside boundary, with the head obviously increasing with depth. Small differences over the farmland can be noticed due to differences in the ground level. A similar reasoning holds for the saturation degree (Figure 5.6). Differences related to the elevation of the ground surface are more evident, such as along the main ditch and along the paleochannel, which is slightly more elevated than the surrounding soil. The levees located between the Morto channel and the farmland were assumed in saturated conditions to simplify the computations and reduce the simulation times, since they do not represent relevant zones for the purpose of this thesis. Finally, Figure 5.7 shows the distribution of salt concentration. The salt moves from the lagoon boundary inland and the effect of freshwater in the Morto channel is visible with brackish zones towards the farmland.

The modelling outcomes are consistent with the available information collected in the study area. A relatively thin (approx 1 m) unsaturated zone developed at the land surface, with the leakage of the freshwater from the Morto channel that helps decreasing the high saltwater flowing from the lagoon boundary southward.

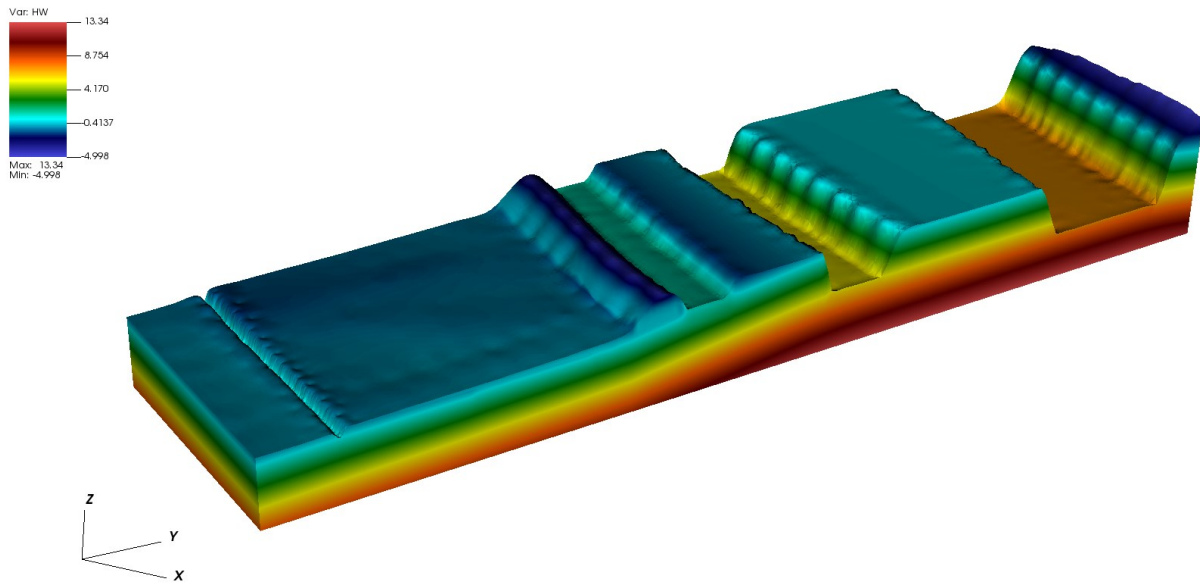


Figure 5.6 Pressure distribution on steady state with the hydraulic gradient from the lagoon side to the land side boundary. Vertical exaggeration is 5.

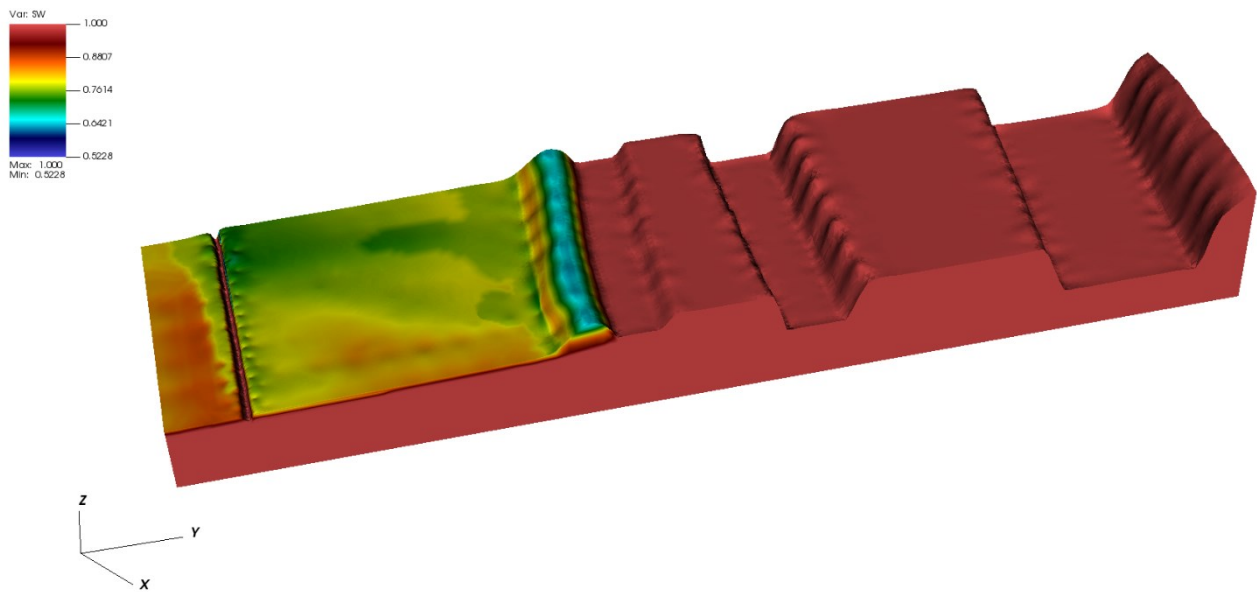


Figure 5.5 Saturation degree in steady state. Vertical exaggeration is 5.

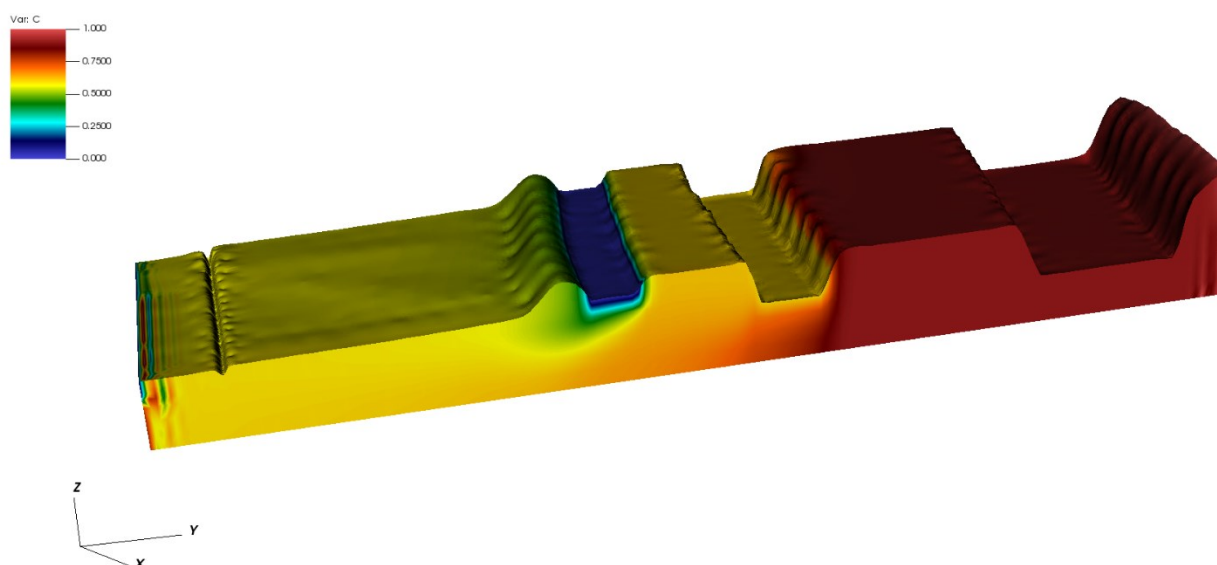


Figure 5.7 Salt concentration in steady state. The numerical fluctuations at the landside boundary are sufficiently far from the area of interest. Vertical exaggeration is 5.

### 5.3.2 Effective precipitation and river dynamics

Effective precipitation, together with water level and salt concentration in the watercourses bounding the study area northward, are the main factors driving the groundwater and salt dynamics in this portion of the Venice farmland.

Precipitation and evapotranspiration of year 2011 (Figure 2.11) were considered as the “typical” climatic stressor forcing the system dynamics. Effective precipitation was imposed as atmospheric boundary condition on the nodes of the farmland surface. Obviously, precipitation is a freshwater input to the system. As to the river conditions, “typical” dynamics were extracted from the available records of salinity measured from May to December 2020 as shown in Figure 2.8 and 2.9. Analyses of those data allowed to develop a typical fluctuation between freshwater and saltwater periods as shown in Figure 5.8, with the corresponding water levels and salt concentration reported in Table 5.3. Values for the Morto channel were kept constant over time. Dirichlet boundary conditions for both the flow and transport equations were imposed on the watercourses.

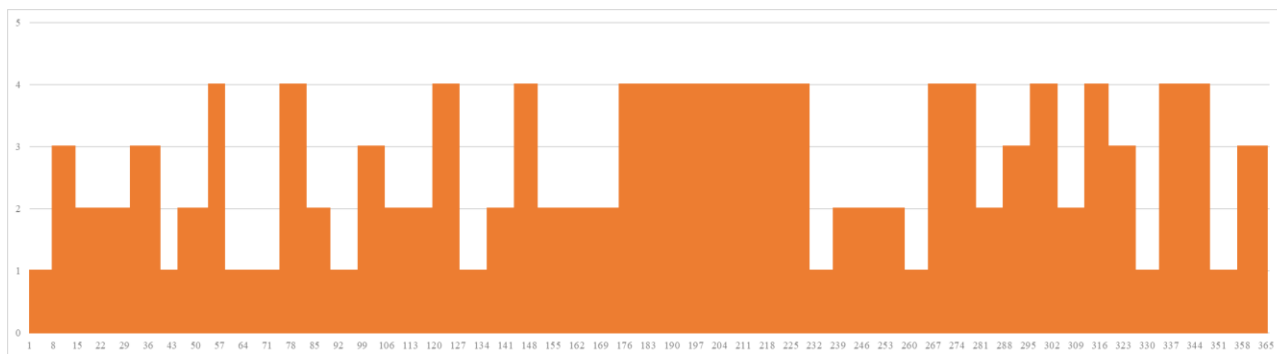


Figure 5.8 Dynamics of the Bacchiglione and Brenta rivers over the “typical” year. Values from 1 to 4 correspond respectively to: 1 - freshwater period for both the rivers; 2 - freshwater period for the Bacchiglione and saltwater period for the Brenta; 3 - saltwater period for the Bacchiglione and freshwater period for the Brenta, and 4 - saltwater period for both the rivers.

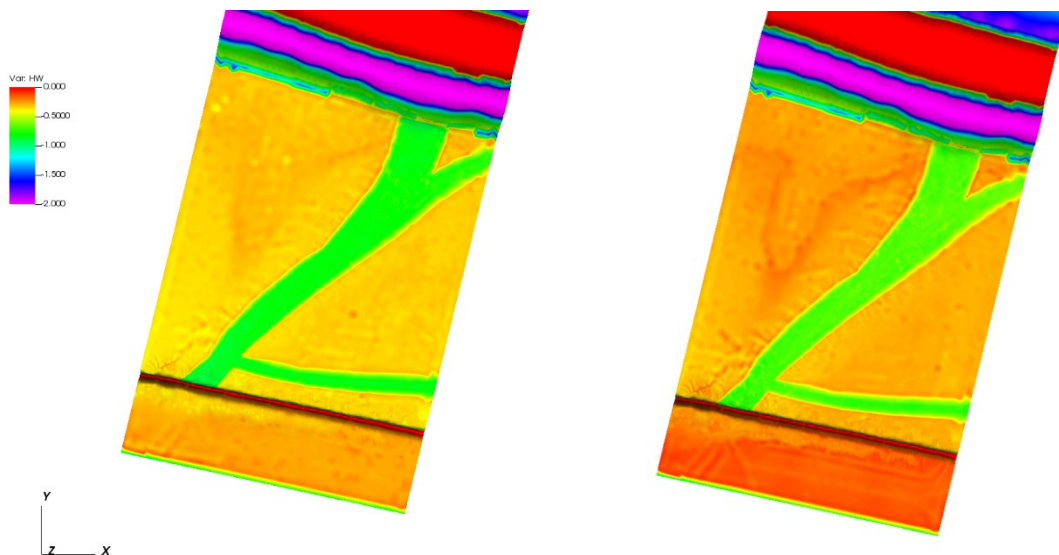
Table 5.3 Water level and salt concentration in the Morto channel and Bacchiglione and Brenta rivers during freshwater and saltwater periods. Values for the Morto channel are assumed constant over time. Concentration in the rivers during saltwater periods are assigned according to the depth from the water table.

The Morto channel	
Water table (m above msl)	0
Concentration (%)	0.04

The Bacchiglione river	Freshwater period	Saltwater period
Water table (m above msl)	1	0.8
Concentration (%)	0	0 (0 - 1 m) 0.3 (1 - 4 m) 0.6 (4 - 5.5 m)
The Brenta river		
Water table (m above msl)	1	0.8
Concentration (%)	0	0 (0 - 1 m) 0.3 (1 - 3 m) 0.9 (3 - 7 m)

Figure 5.9 and 5.10 compare the model outcomes in terms of pressure head and saturation after 76 days, i.e. at the end of a significant rainfall event, as obtained by assuming isotropic or anisotropic hydraulic conductivity. Limit values for the colour scale were set to highlight the variations due to the different  $K_{s,z}$ . It is worth to be highlighted:

- the different response between the sandy and the silty portions of the area;
- pressure head and saturation are higher in anisotropic conditions especially outside the sandy paleochannels since the infiltration of water is hindered by the lower vertical hydraulic conductivity.



*Figure 5.9 Pressure head at the land surface for the isotropic (to the left) and anisotropic (to the right) cases after 76 days. Limit values for the colour scale are set equal to -2 and 0 to appreciate the differences between the two cases.*



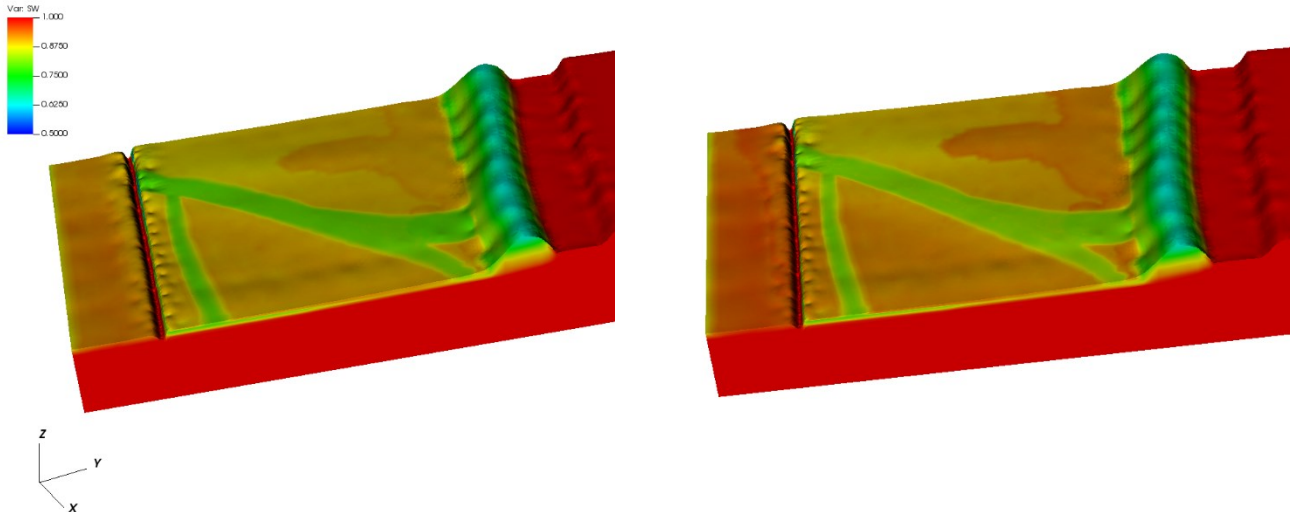


Figure 5.10 Saturation degree for the isotropic (left) and anisotropic (right) cases after 76 days. The colour scale is set between 0.5 and 1. Vertical exaggeration is 5.

Pressure head and saturation degree only for the anisotropic case are also showed specifically for the upper soil on a vertical section in the middle of the farmland (Figure 5.11). It can be observed that the water table after 76 days is slightly higher than after 198 days and that a thin more saturated zone formed with the rainfall event over the less permeable soil.

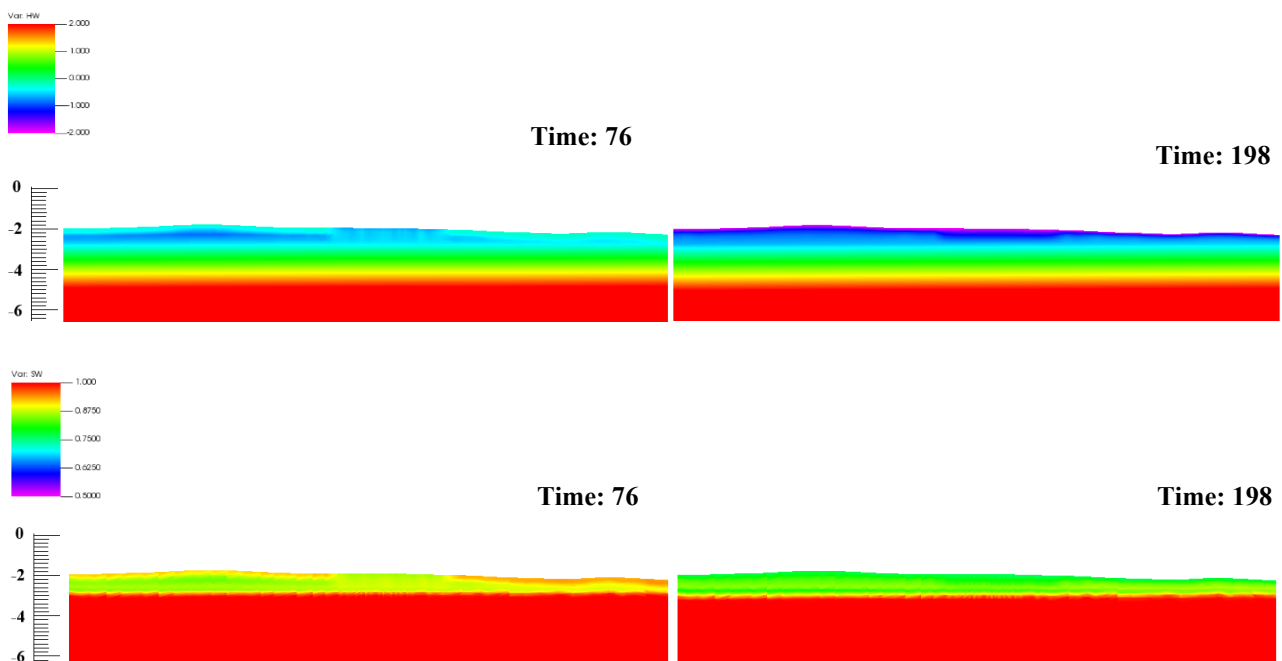


Figure 5.11 Pressure head (above) and saturation (below) after 76 (left) and 198 (right) days with anisotropic hydraulic conductivity. Vertical exaggeration is 5.

Figure 5.12 shows the salt concentration after 76 and 198 days as obtained by the model with the anisotropic property distribution. The first time (76 days) represents the condition at the end of a rainfall event with widespread freshwater (in violet) in the shallowest soil. Conversely, the conditions at 198 days are characterized by high evapotranspiration with no rainfall in the previous ten days and, consequently, the salt concentration increases also at the farmland surface. The saturation after 198 days is also reported (Figure 5.13), with lower values, as expected, ranging between 0.65 and 0.8 on the superficial soil. No significant differences between the isotropic and anisotropic cases were obtained at this time.

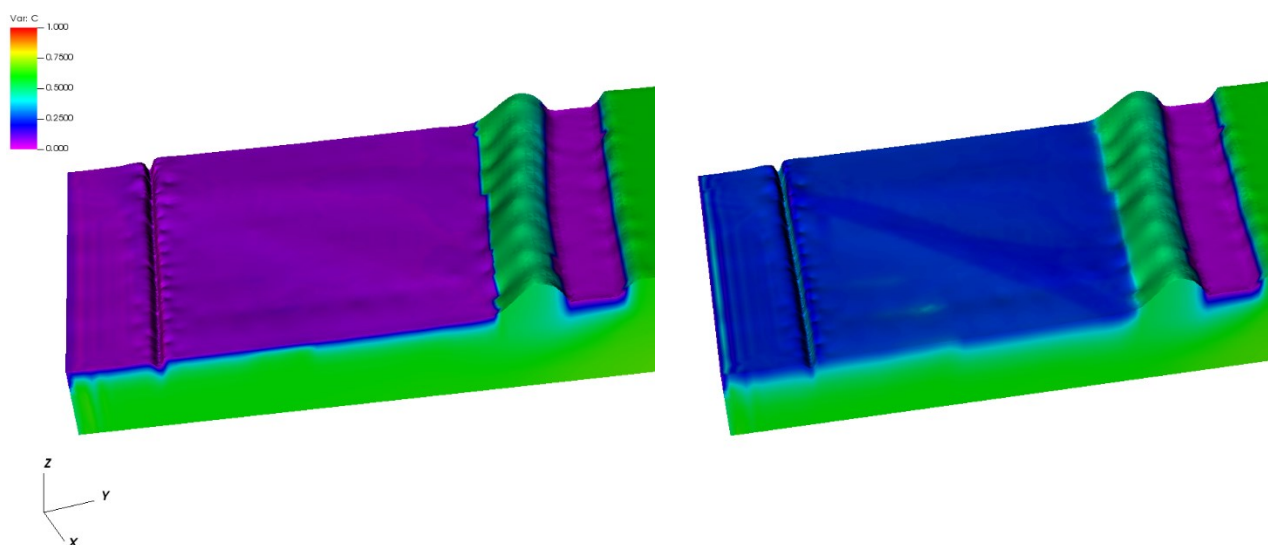


Figure 5.12 Salt concentration for the anisotropic case after 76 (to the left) and 198 (to the right) days. Vertical exaggeration is 5.

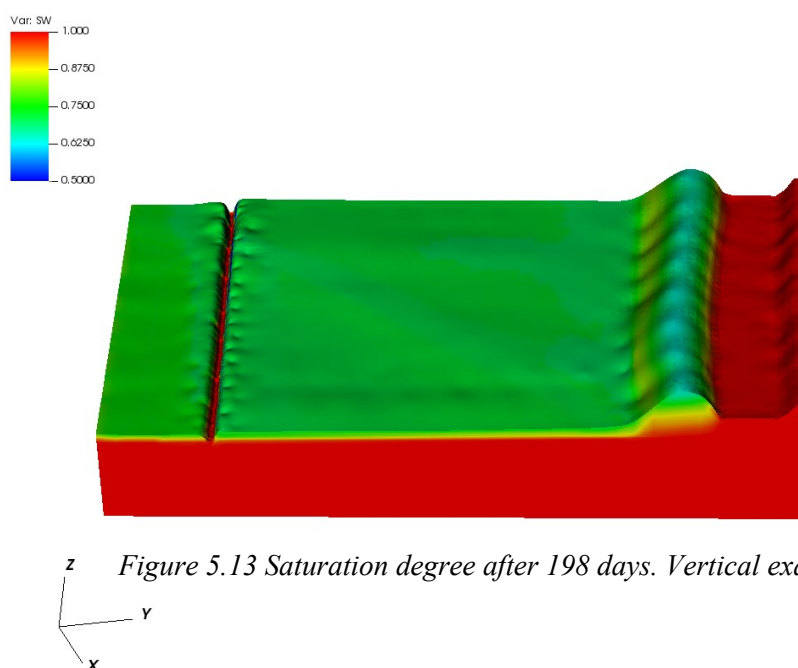
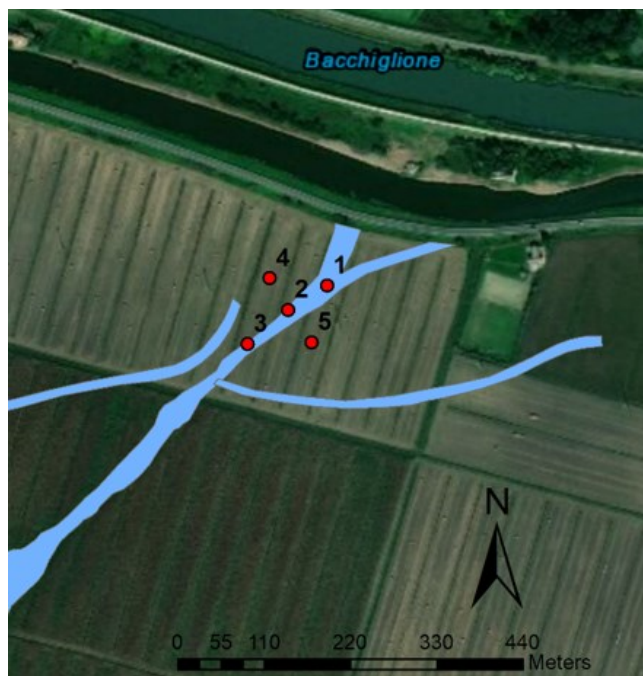


Figure 5.13 Saturation degree after 198 days. Vertical exaggeration is 5.

Ten nodes were selected at about 0.5 m and 1.5 m below the ground level in the five relevant locations (three along the paleochannel and two outside) shown in Figure 5.14, to better understand the trend of pressure head, saturation, and concentration over time.



*Figure 5.14 Relevant locations in the study area (three are along the paleochannel in blue and two are outside) selected to show the model results versus time.*

Figure 5.15 and 5.16 show the results of a 2-year simulation with the anisotropic parameters in terms of pressure head and salt concentration versus time at the 5 stations at two depths described above. The effective precipitation, representing the forcing applied to the system, is also plotted to better analyse the results. The results in terms of saturation (Figure 5.17) were obtained for a limited number of time steps and subsequently interpolated. Notice the rise of the pressure head and saturation in correspondence of rainfall events, especially for the most superficial nodes, which are more affected by the conditions on the surface. The pressure head is always negative for the nodes at 0.5 m below the ground level and is generally positive for the nodes at 1.5 m depth with saturation equal to 1 indicating that they are situated above and below the water table, respectively. Also notice that the higher pressure head at station 5, especially at depth (Figure 5.16), is due to the lower elevation of the land surface at that location. Obviously, the pressure head fluctuations are more evident close to the land surface than at depth. As to the concentration, after an initial transient phase, it is possible to notice the clear response of the parameter to the forcing factor, with concentration drops corresponding to rainfall peaks and increase in dry periods. On the average, salt concentration is larger at 1.5 than at 0.5 m depth in agreement with the available records.

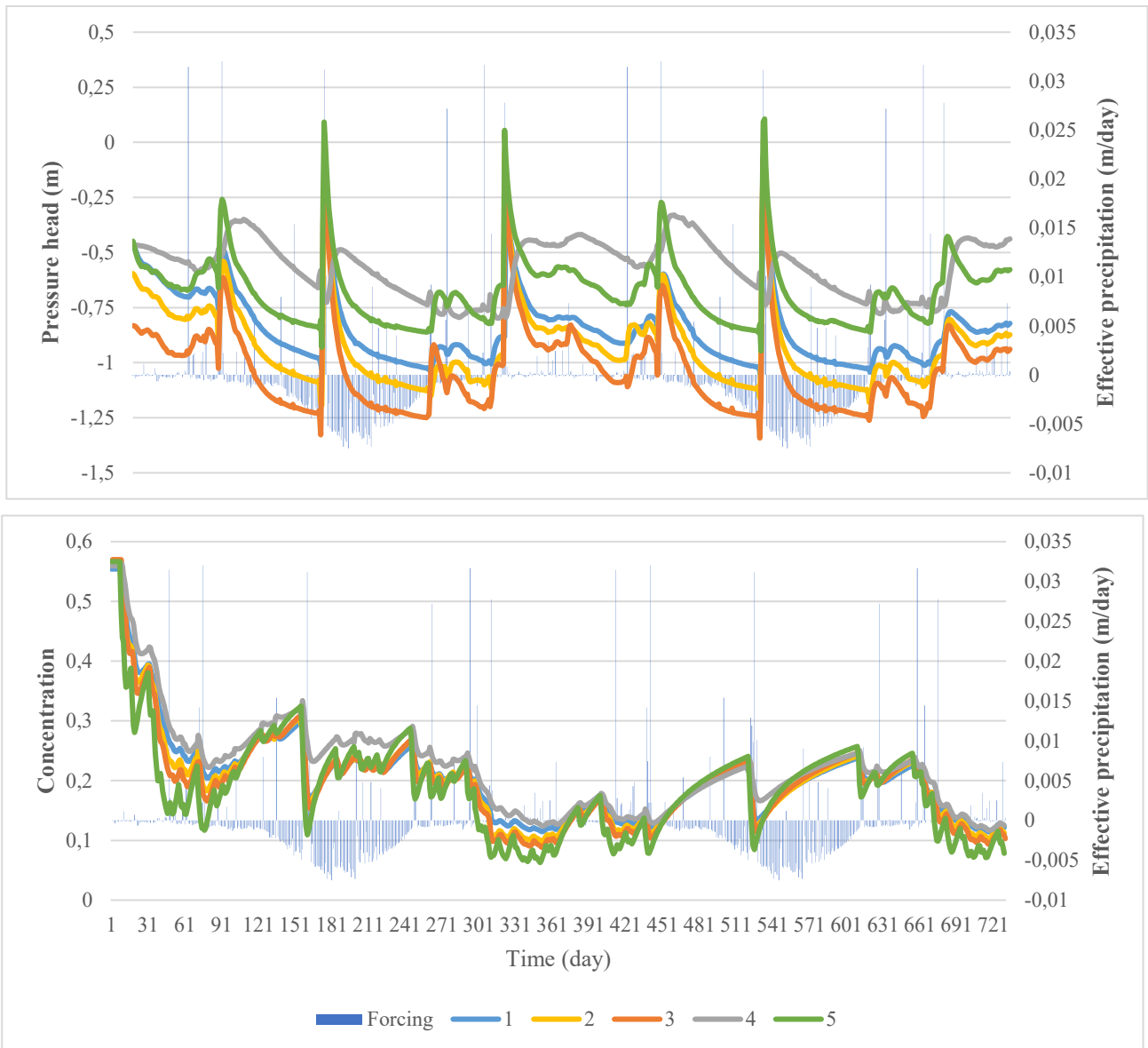


Figure 5.15 Pressure head and salt concentration over 2 years at 0.5 m below the ground level in the 5 stations shown in Figure 5.14.

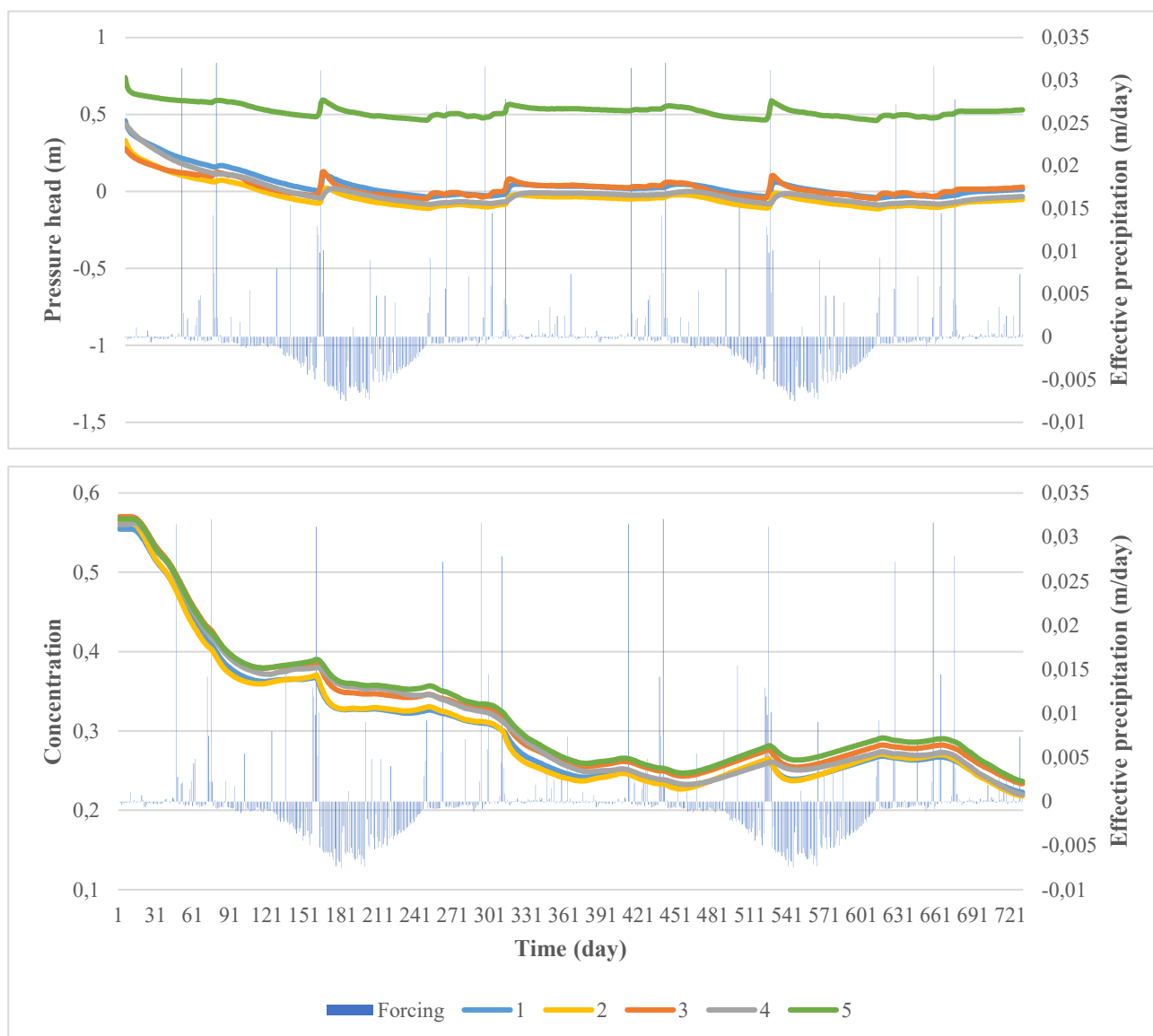


Figure 5.16 Pressure head and salt concentration over 2 years at 1.5 m below the ground level in the 5 stations shown in Figure 5.14.

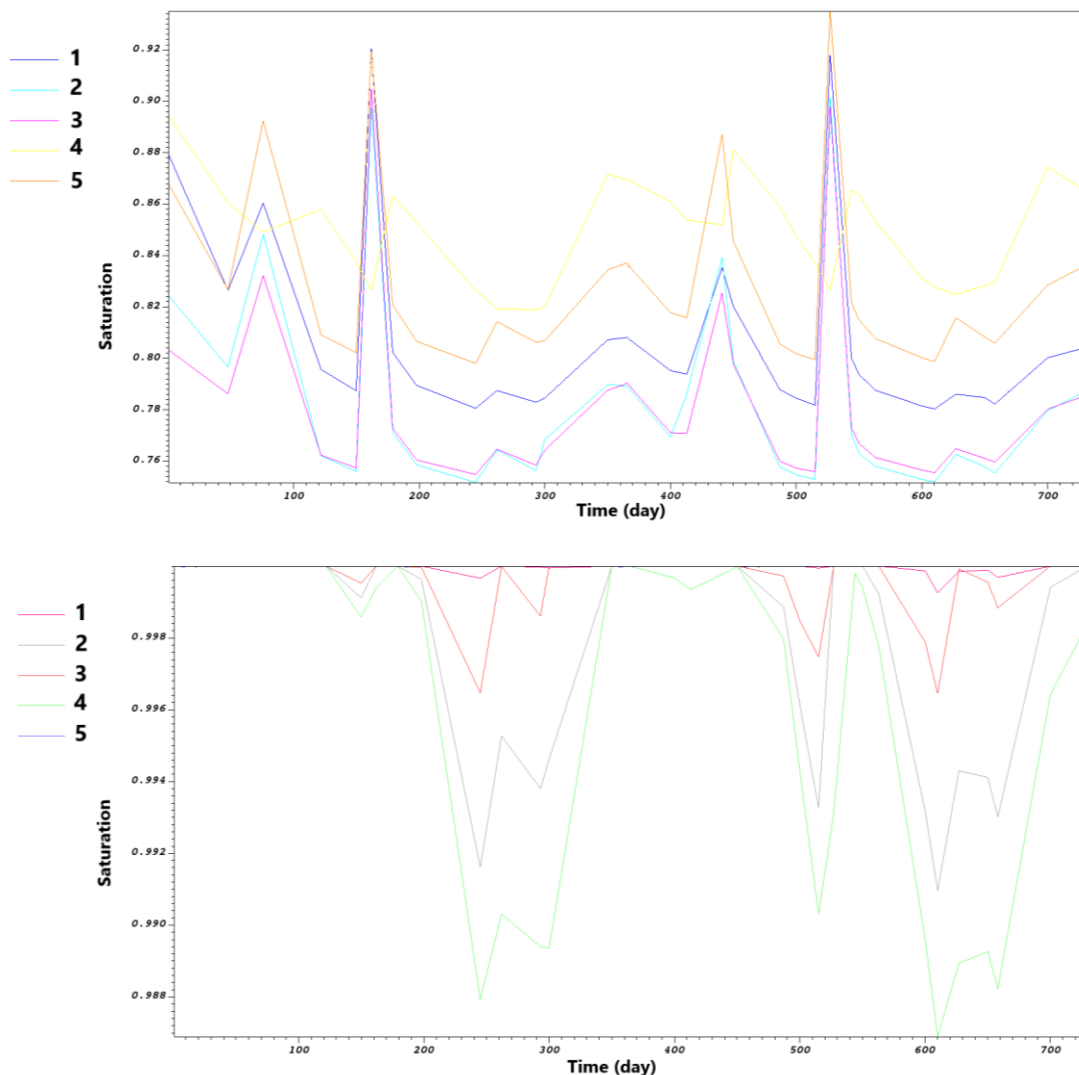


Figure 5.17 Interpolation of saturation degree over 2 years at 0.5 (above) and 1.5 m (below) below the ground level in the 5 stations shown in Figure 5.14.

A long-term simulation was carried out to understand in detail the effects of the river dynamics on the subsurface system. A 10-year simulation was developed by prescribing the boundary conditions provided in Figure 5.8 and Table 5.3 and assuming a null flow (i.e., without the effective precipitation) on the farmland surface. Only the isotropic case was considered to favour the dynamics in a conservative approach. Ten nodes located at about -6 m below msl along the longitudinal section were selected to describe the system dynamics over time (Figure 5.18). Figure 5.19 shows the simulation results of the transport model: the continuous profiles correspond to the nodes below the rivers and the channel (A, D and F), the dashed lines are relative to nodes in proximity of the levees (B, C, E and G), and the dotted lines are related to the nodes in the farmland area (H, I and J). The

salt concentration generally increases for the nodes closer to the lagoon side boundary. Notice that only the nodes located directly below the riverbeds significantly feel the large fluctuations of the salt concentration in the rivers. A smoother behaviour characterizes the evolution below the farmland, with the effect of the river dynamics that are evident with periodic phases corresponding to the different years.

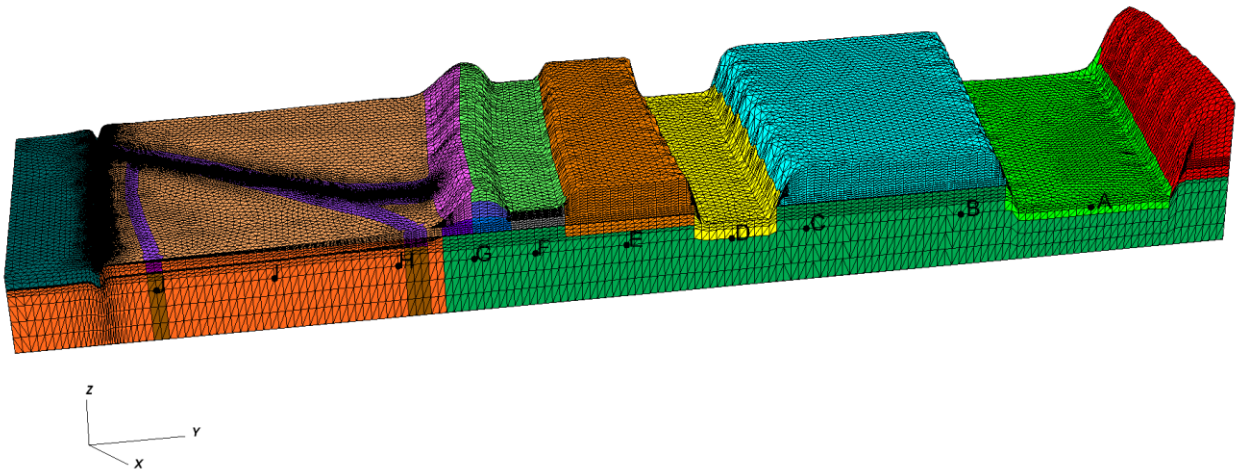


Figure 5.18 Nodes A-J selected to analyse the salt concentration profiles vs time in relation with the river dynamics over 10 years. Vertical exaggeration is 5.

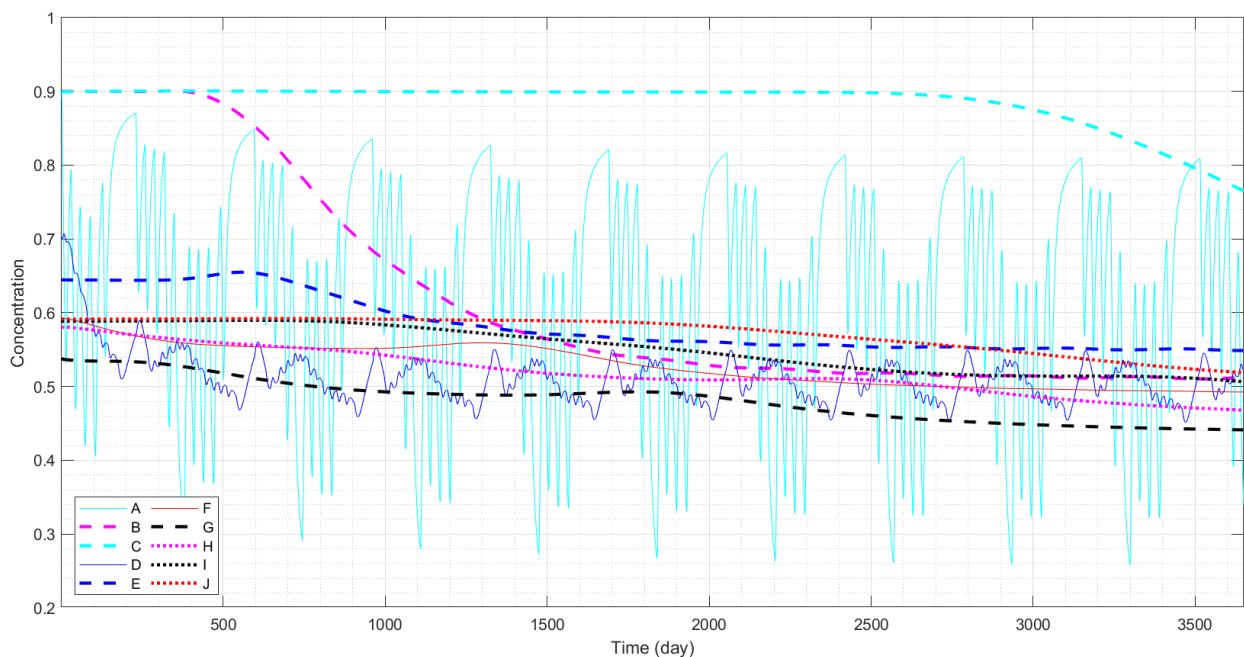


Figure 5.19 Salt concentration versus time for 10 nodes over 10 years. Node locations are provided in Figure 5.18.

The concentration distribution at the final time step is shown in Figure 5.20. The time period of 10 years turned out to be not fully sufficient to reach a “proper equilibrated” condition, as it can be deduced from the more saline zone still present along a side of the levee between Bacchiglione and Brenta. Nevertheless, the rivers dynamics does not seem to have straightforward effects in the farmland, where the concentration decreases under the effect of the recharge from the Morto channel freshwater. Here, an “equilibrated” condition was reached after about 4 years.

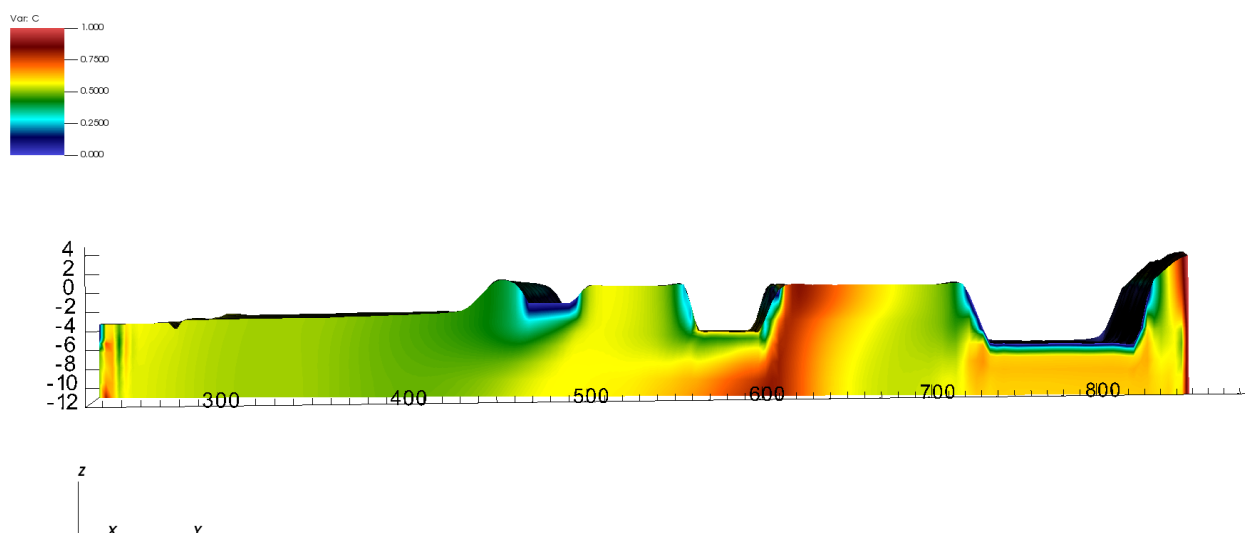
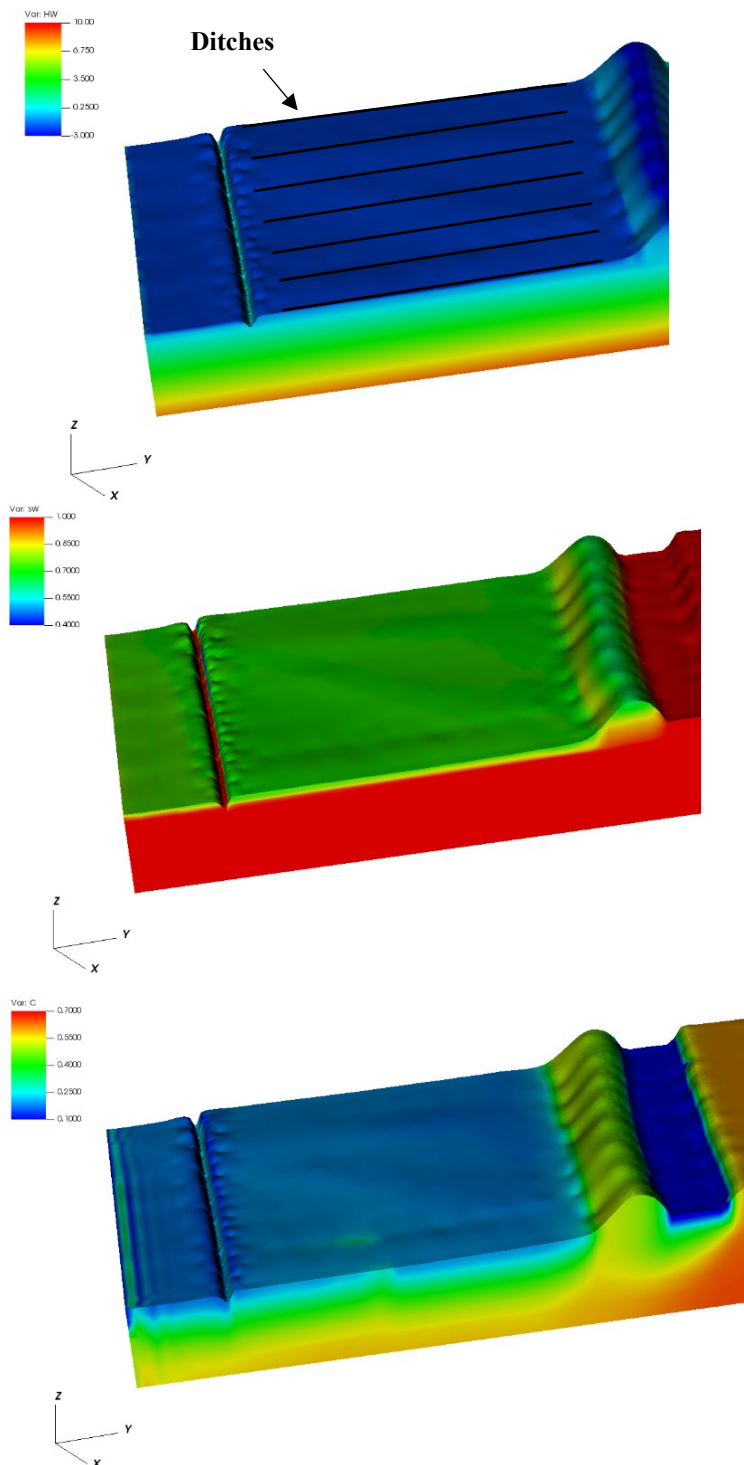


Figure 5.20 Simulation results of the transport model with the river dynamics after 10 years. Vertical exaggeration is 5.

### 5.3.3 Recharging the farmland through the drain

The effect of releasing freshwater in the paleoriver through the drain was simulated using as initial condition the model outcome at time equal to 500 days (Figures 5.15, 5.16 and 5.17). The drain recharge was superposed with the effective precipitation and river dynamics. Figure 5.21 shows the system condition in terms of pressure head, saturation degree and salt concentration at the beginning of the drain activity.

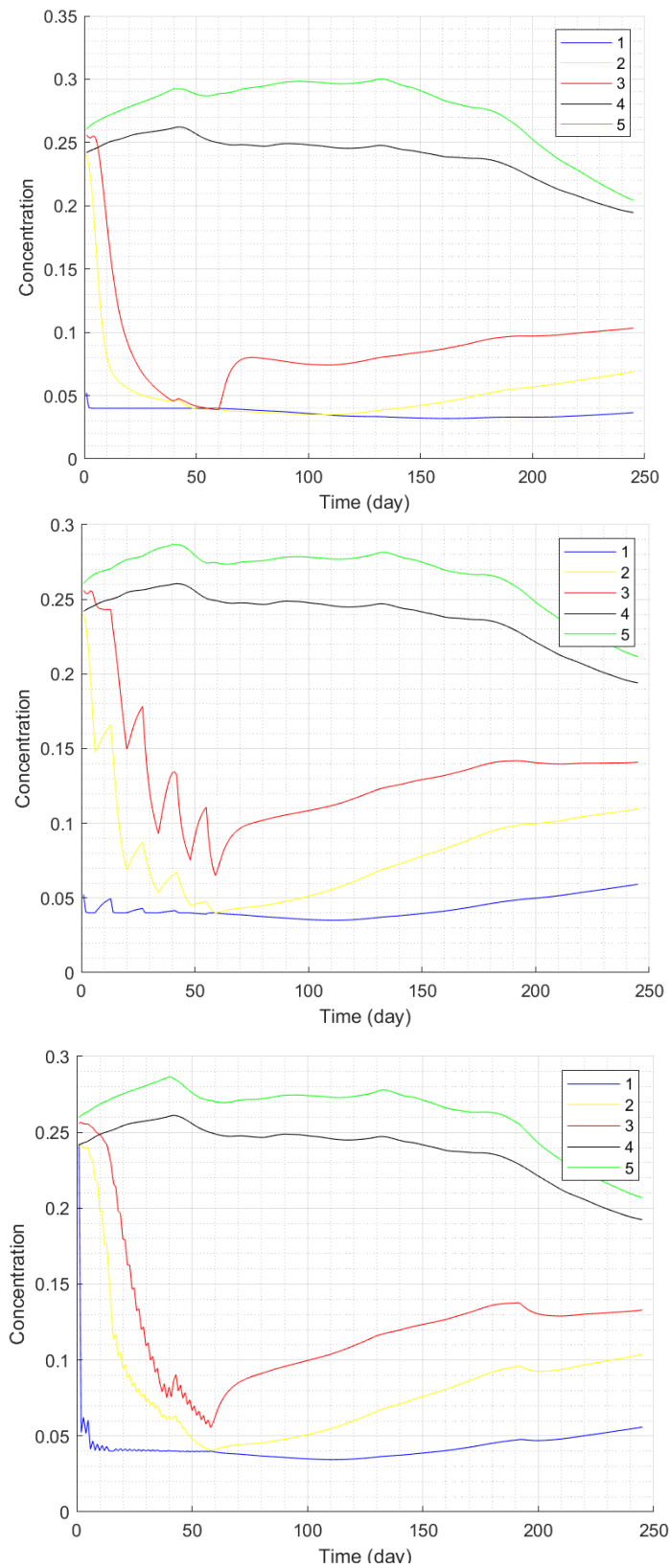




*Figure 5.21 Pressure, saturation and concentration as initial conditions for drain simulations (from top to bottom). Appropriate limit values are set according to the solution. Vertical exaggeration is 5.*

The simulations spanned a time interval of 245 days, with an initial period of 60 days between May and June (i.e., the most critical months in terms of water availability) when the drain is operating, after which the drain was shutdown. Three different operative conditions for the drain were considered: continuous discharge, weekly intermittent operation, and daily intermittent operation (indicated in the following with A, B and C case, respectively). Both isotropic and anisotropic hydraulic conductivity conditions were simulated. The drain was simulated by means of a Neumann condition, with a cumulative flowrate equal to 580 m<sup>3</sup>/day. This value was uniformly distributed along the drain.

Figure 5.22 shows concentration profiles at the five stations reported in Figure 5.14 at 1.5 m depth below the ground surface, where the effect of precipitation is less relevant compared to the most superficial nodes. During the first 60 days, the different operative conditions of the drain are evident with concentration drops when the drain is in operation in alternate weeks and days (B and C cases). The first three stations are along the paleochannel where the drain produced the maximum positive effect, whereas for the nodes at a larger distance the concentration changes were mainly due to the rainfall events. After 60 days, i.e. after the drain shutdown, the salt concentration started to rise for the stations 1, 2 and 3, especially for the last one, located at higher depth.



*Figure 5.22 Concentration of the five stations at 1.5 m below the ground level for 245 days for A, B and C cases (from top to bottom). The results refer to the outcome with an anisotropic hydraulic conductivity.*

The simulation results are also provided on a vertical section of the domain around the drain location, in the middle of the farmland. Figure 5.23 shows the simulation results after the first week of operation for both the isotropic and anisotropic cases. Notice that in the colour scale the maximum concentration value was lowered from 1 to 0.6 to enhance the contrast between different concentration levels, improving the clearness of the transport dynamics. Freshwater spreads from the drain located at about 1.5 m below the ground level. Of course, during this period, the model outcomes are the same in the A and B cases. The effect of anisotropy is evident, with freshwater propagation favoured in the horizontal direction. However, concentration results of B and C cases tend to match over longer time intervals. Obviously, case C is not a viable option for practical reasons (drain opening and shutdown must be carried out manually) and therefore further results are only provided for A and B cases. Figure 5.24 shows the salt concentration after 30 days, that is half the time of the drain operation. It is possible to notice the effect of the ditches, which make the freshwater flow towards them due to their lower pressure but at the same time they hinder the freshwater flow beyond them. Furthermore, it is also visible how freshwater moves faster in the saturated zone, where the hydraulic conductivity is higher compared to the shallower unsaturated zone.

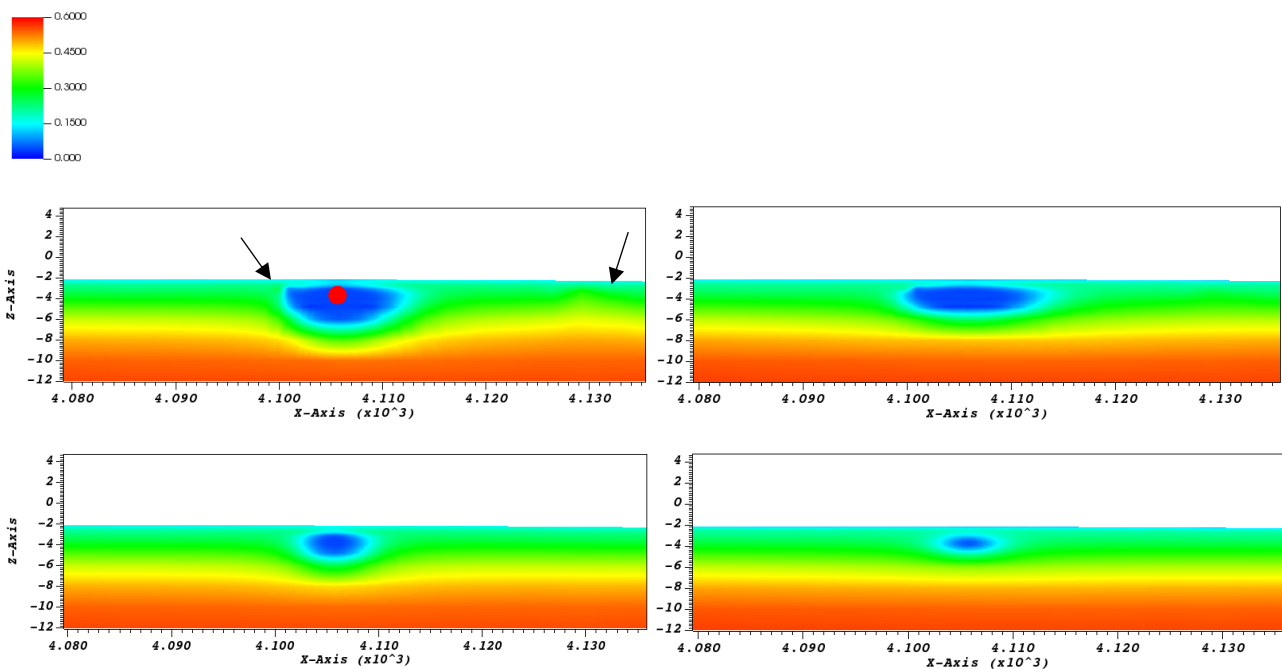
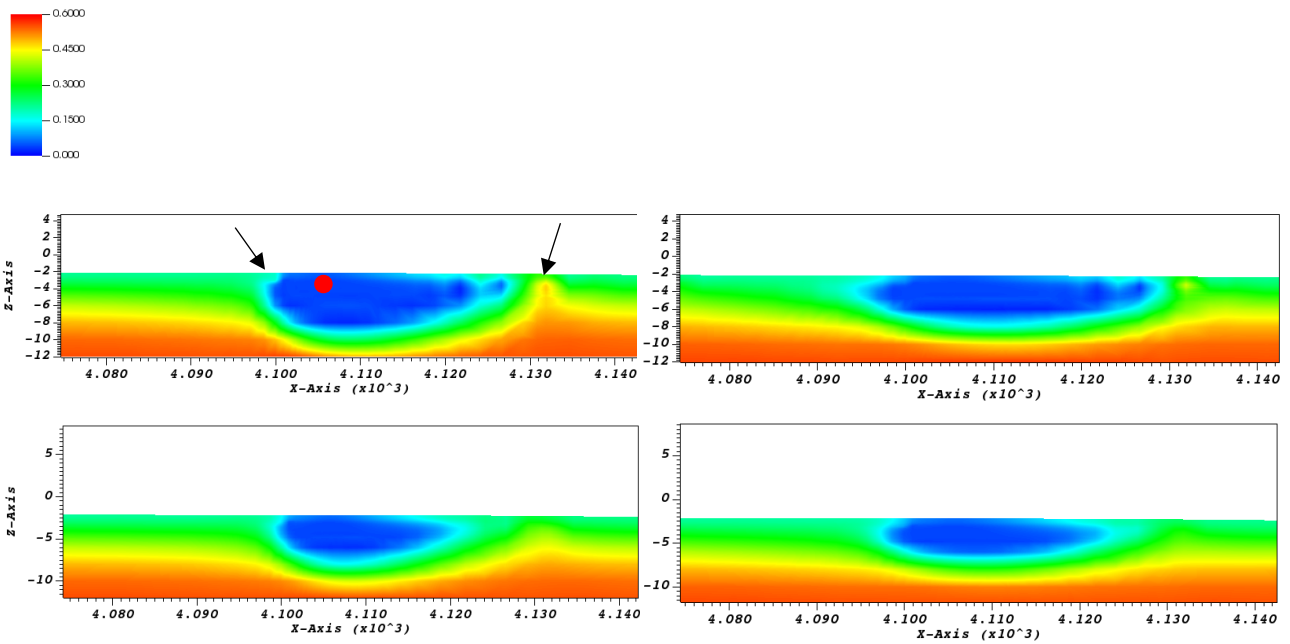


Figure 5.23 Concentration after 1 week for continuous and weekly intermittent operations (above) and for daily intermittent operation (below) considering isotropic (to the left) and anisotropic (to the right) hydraulic conductivity. Black arrows show the location of the nearby ditches and the drain is in red (not to scale).



*Figure 5.24 Concentration after 30 days for continuous (above) and weekly intermittent operations (below) considering isotropic (to the left) and anisotropic (to the right) hydraulic conductivity. Black arrows show the location of the nearby ditches and the drain is in red (not to scale).*

Concentration results are also given after 60 days, i.e. at the end of the time of drain operation (Figure 5.25) and 120 days, i.e. two months after the drain shutdown (Figure 5.26) for the anisotropic case only, as this is considered more realistic. With the parameter adopted in this simulation the transport process results very slow and freshwater “bubble” remained almost unchanged in the upper until the simulation end.

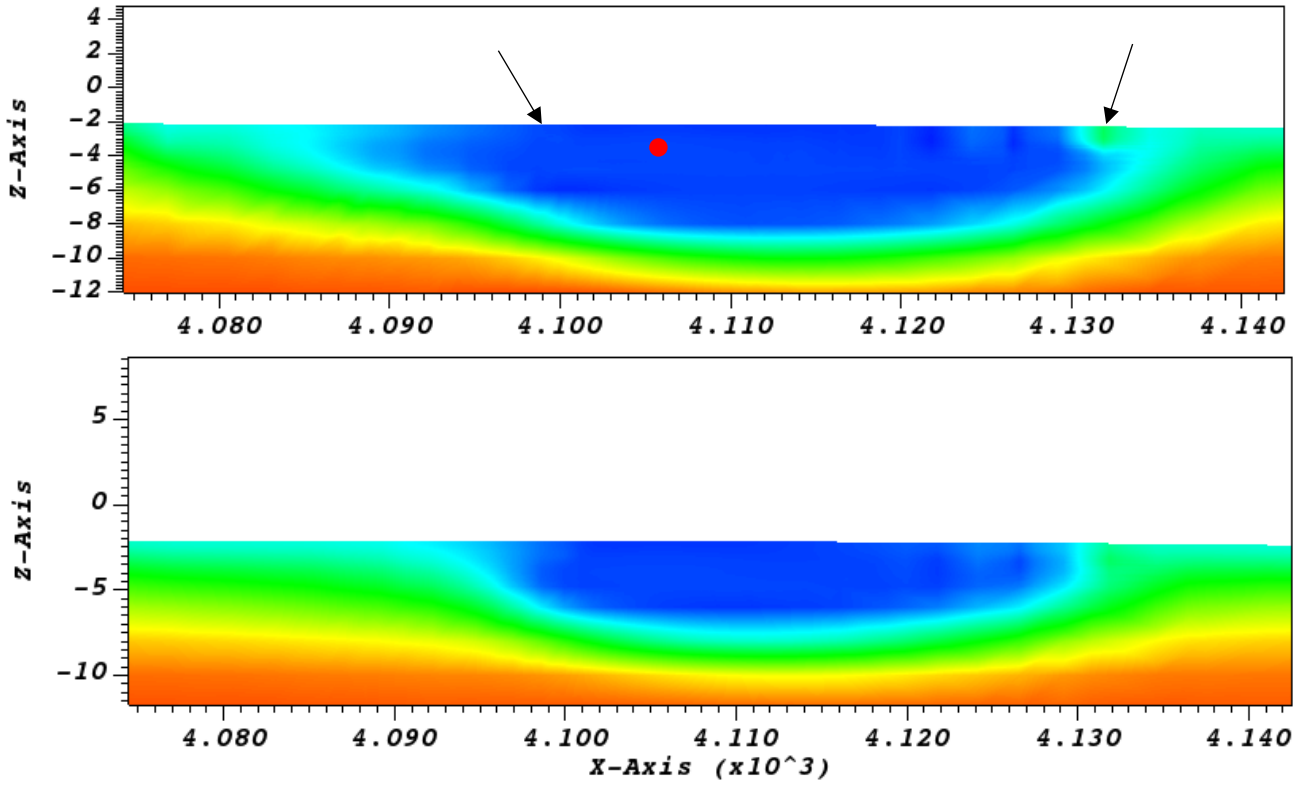
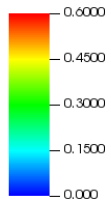


Figure 5.25 Concentration after 60 days for the continuous (above) and weekly intermittent (below) operation with the anisotropic case. Black arrows show the location of the nearby ditches and the drain is in red (not to scale).

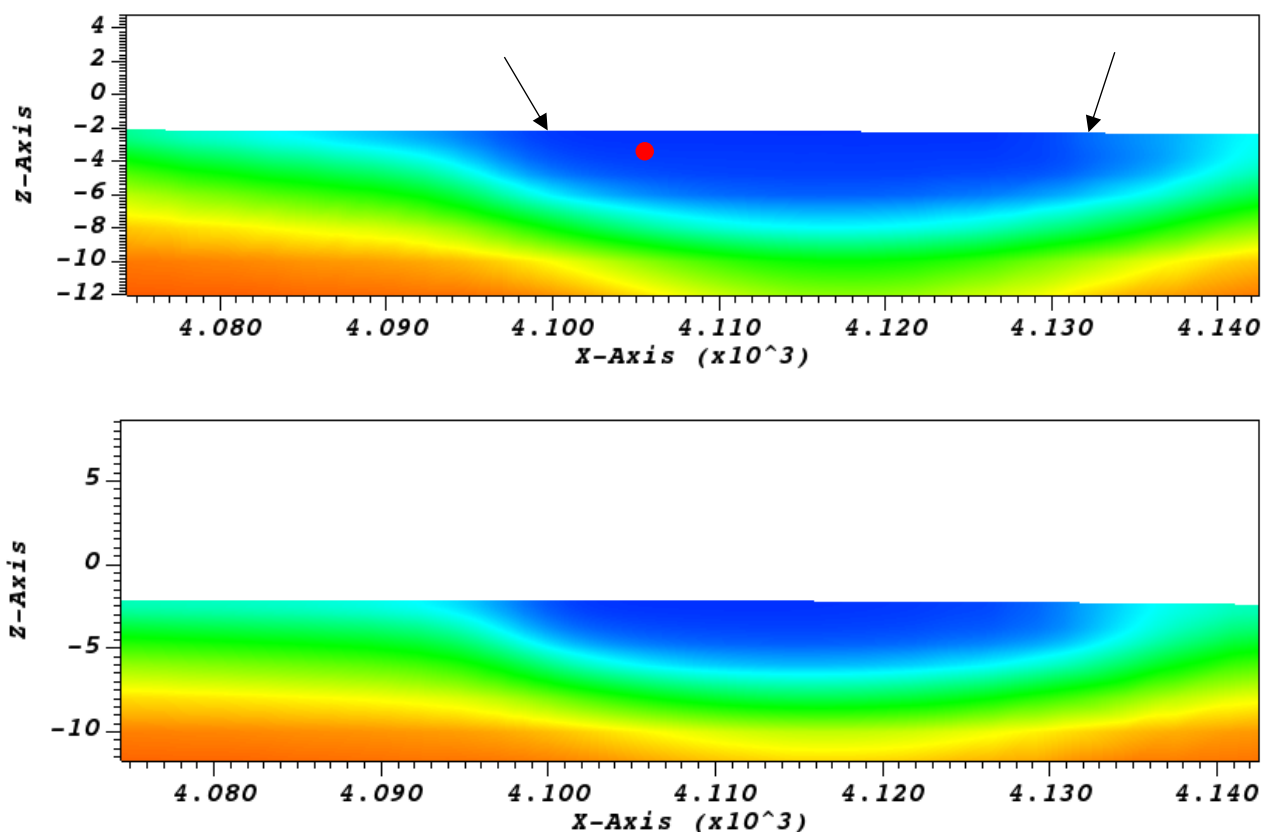
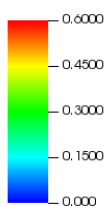


Figure 5.26 Concentration after 120 days for the continuous (above) and weekly intermittent (below) operation with the anisotropic case. Black arrows show the location of the nearby ditches and the drain is in red (not to scale).

Figures 5.27 and 5.28 show the salt concentration on the farmland surface after 10, 30, 60 and 120 days for the A and B cases with the anisotropic hydraulic conductivity. The recharge effect is well evident and involve approximately the whole sandy paleoriver. It can be observed that freshwater moved southward, i.e. towards the landside boundary, due to the natural hydraulic gradient. The effect of the ditches is also quite important.

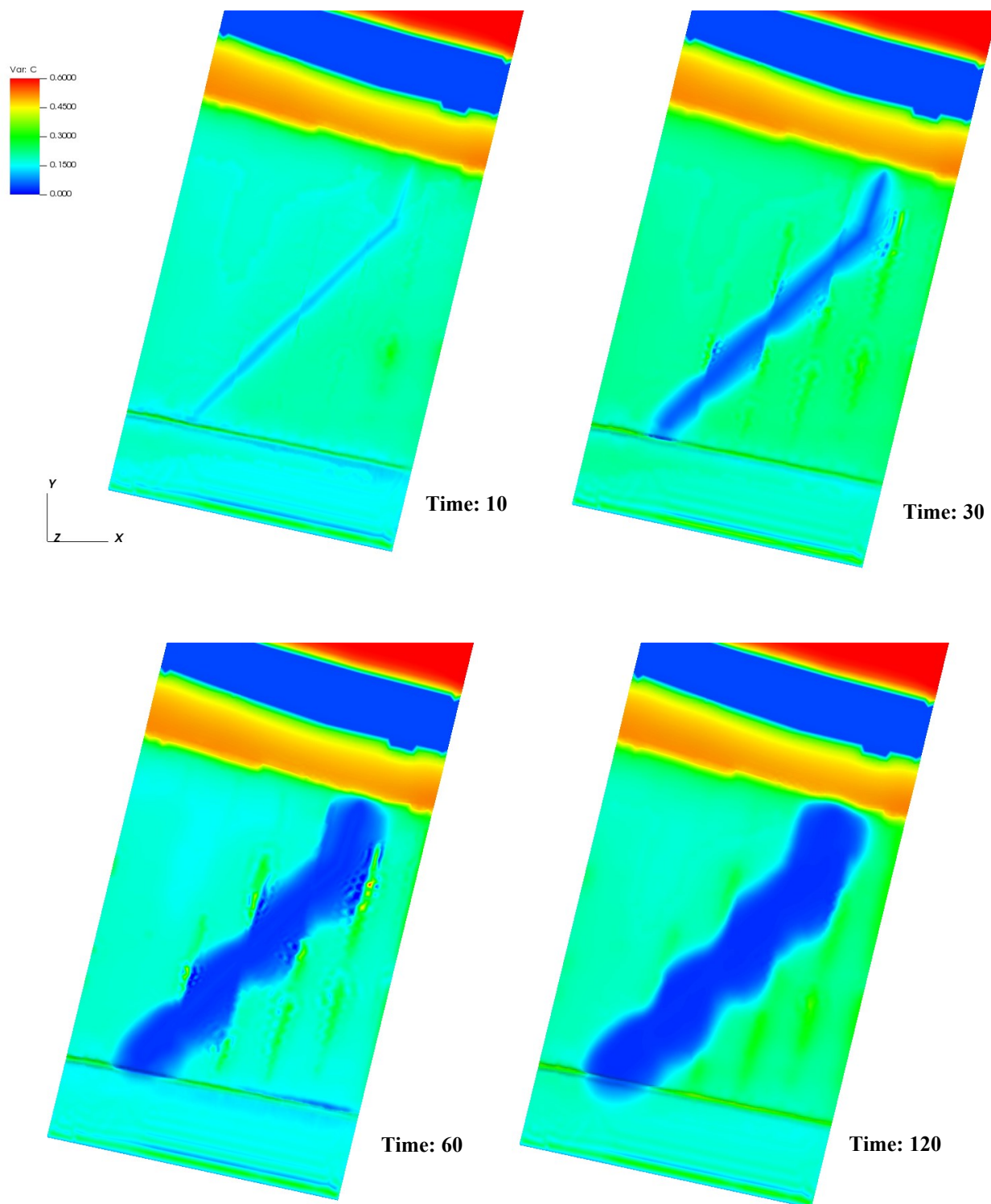


Figure 5.27 Case A, anisotropic hydraulic permeability: salt concentration after 10, 30, 60 and 120 days.



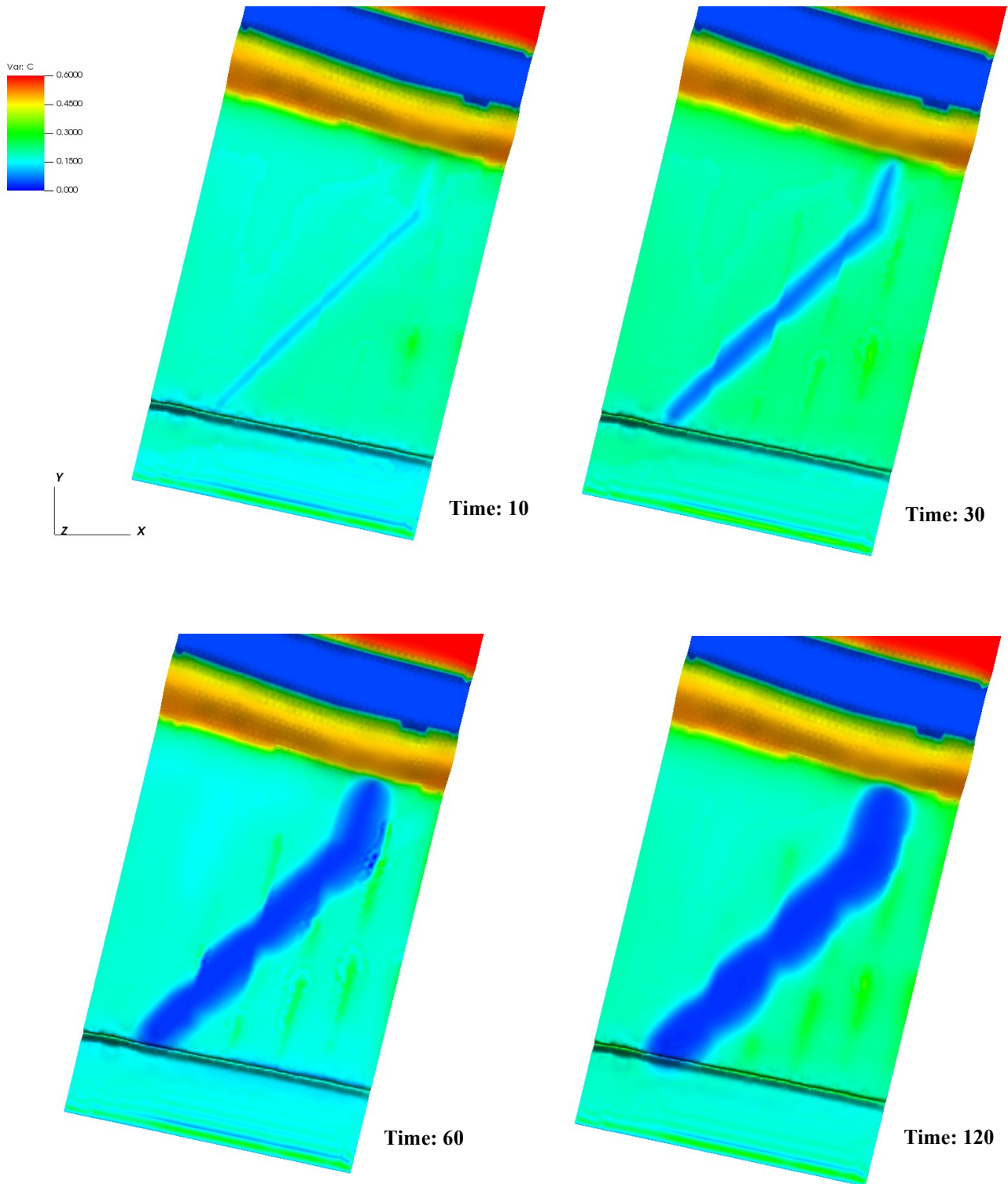


Figure 5.28 Case B, anisotropic hydraulic permeability: salt concentration after 10, 30, 60 and 120 days.

For completeness, pressure head and saturation degree (on the same vertical section in the middle of the farmland) are also shown in Figure 5.29 and 5.30 at the start and end of the drain operation, respectively, for the A case with anisotropic hydraulic conductivity. Limit values for the colour scale are chosen to appreciate the variations in the upper part of the aquifer. The drain causes a local increase of pressure head and rise of the water table. After 60 days of operation, it is evident the effect of the ditches (especially the ones close to the drain) which keep the water table at about 1 m below the ground level.

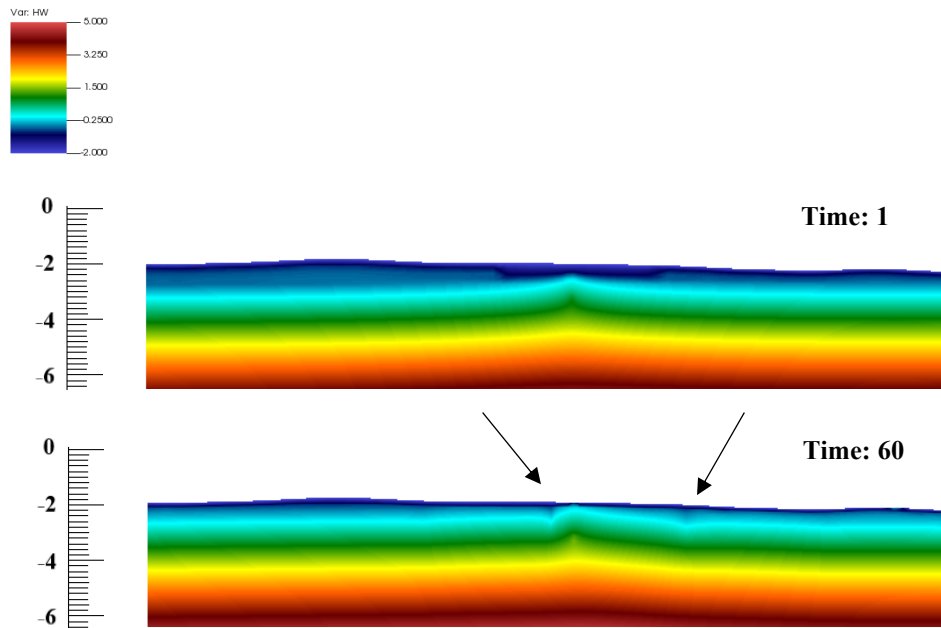


Figure 5.29 Case A, anisotropic hydraulic permeability: pressure head at the start (above) and end (below) of the drain operation. Vertical exaggeration is 5.

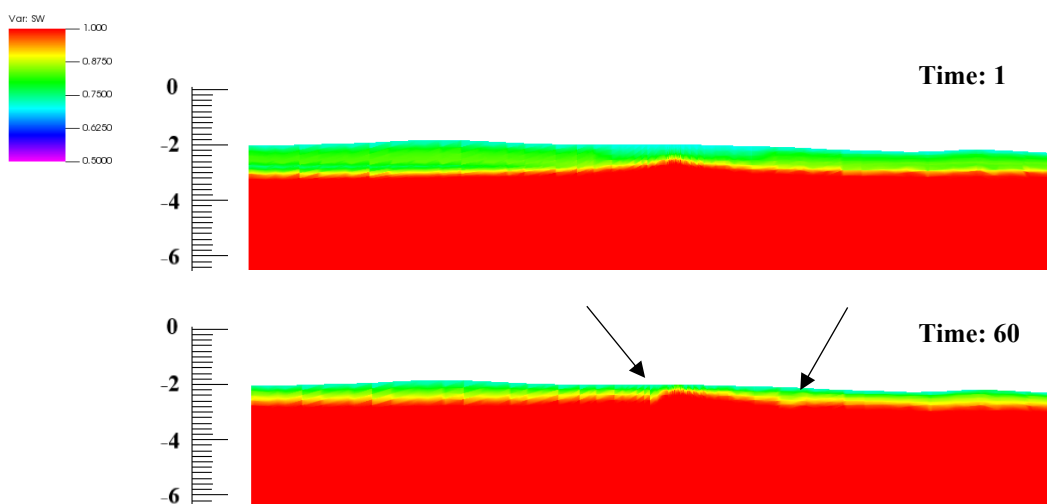


Figure 5.30 Case A, anisotropic hydraulic permeability: saturation degree at the start (above) and end (below) of the drain operation. Vertical exaggeration is 5.

## 5.4 Discussion

The 3D mesh generation was a crucial step of the model development due to the domain geometry and size. Several adjustments were made to the grid to have an appropriate mesh quality keeping an acceptable computational burden. Despite the large number of nodes and elements (more than 500'000 and 3'000'000, respectively), the mesh still presents element deformation, especially in areas of strong elevation gradients such as the main ditch and the levees, which had caused several convergence problems in the first simulations. There is also a zone between the paleochannel and the levee, close to the western boundary, where strongly deformed elements (due to the vertical discretization used) may have affected the computations. Another three-dimensional mesh generation program, like TetGen, would have been more suitable for such an irregular geometry. The large number of elements has also severely affected the choices related to the investigated simulations and the phases of data elaboration and analysis, due to the long times required. However, simulation times can widely vary (from a few hours to several days) according for instance to the imposed initial and boundary conditions, the flow and transport parameters and the applied forcing. Some limitations were also due to the GWS, which is not very user-friendly. Simulation time-steps must be decided a priori and written in the input files, without automatic time stepping, which can significantly reduce simulation time while maintaining the accuracy of the solution. Again, specific time steps for solution printing must be provided as input before the start of the simulation. This complicates the pre-processing and post-processing phases, especially when you need to analyse the system dynamics and you do not know the evolution time of a certain process or you encounter some anomalies in the solution. Moreover, numerical fluctuations due to boundary effects are also present along the lagoon and land side boundaries, but they have a limited extension and they are sufficiently far from the area of interest.

Some limitations of the model are also due to the heterogeneity of the soil, the lack of experimental data and, therefore, uncertainties of flow and transport parameters. The availability of new experimental data will be essential for the calibration of the flow and transport parameters and the development of a more robust and reliable model.

# Conclusions

---

This thesis is focused at modelling the hydrological processes, from both the quantitative and qualitative points of view, in a coastal farmland at Ca' Pasqua, in the southern part of the Venice lagoon, which is severely affected by seawater intrusion. More specifically, the aim is to carry out a preliminary assessment of the potential effects on the salt concentration of a recharge drain recently established at 1.5 m depth along a sandy paleochannel crossing the study area.


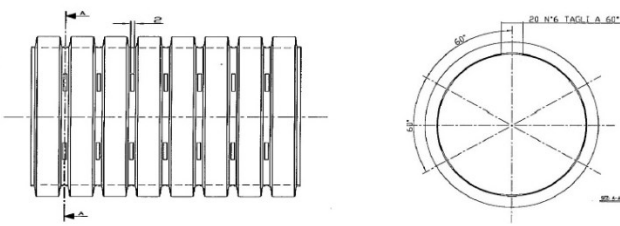
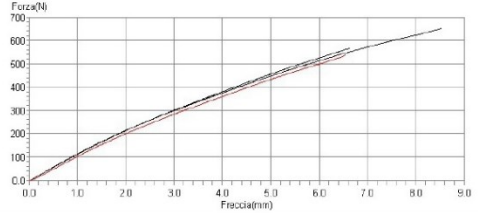
Starting from available geophysical and hydrological data, the case study was numerically simulated with a three-dimensional finite-element density-dependent flow and transport model, using the GroundWater Simulator (GWS) software. A preliminary phase with several test simulations of a simplified case study was essential to become familiar with GWS and the processes and parameters involved. A tetrahedral FE grid made of more than 500'000 nodes and 3'200'000 elements allowed to accurately reproduce the site topography (with the farmland, drainage ditches, embankments, and watercourses), the geological setting, and the approx. 200-m long recharging drain. The element size ranges from 0.25 (which almost corresponds to the drain diameter) to 4 m (at the model lateral boundaries), thus allowing an accurate model solution around the features of main interest.

The numerical simulations of the real case study allowed to investigate the effects of seasonal variations related to precipitation, evapotranspiration and the salt concentration in waterbodies bounding the farmland northward. The superficial soil of the farmland resulted to be highly affected by the effective precipitation and by the nearby channel to a minor extent, but no significant effects were observed due to the river dynamics. Subsequently, the drain was implemented with three different operation conditions for a period of 60 days. All simulations were run with isotropic and vertical anisotropic conditions for the saturated hydraulic conductivity, considering the last one more realistic. Preliminary results show that the recharge drain is an effective mitigation strategy against saltwater intrusion, reducing the salt concentration in the agricultural field as desired. Some limitations of the model are due to the heterogeneity of the soil, the lack of experimental data and, therefore, uncertainties of flow and transport parameters.

Further researches will involve flow and transport parameter calibration and the simulation of a cut-off wall established orthogonal to the recharging drain direction along a portion of the main ditch to limit the southward movement of the injected freshwater.

# Appendix

## A.1 Recharge drain datasheets

		<b>SCHEDA TECNICA PRODOTTO</b>		REV.1	
		<b>FITT Rolldrain</b>			
Ø	<b>160</b>	TIPO	<b>FITT Rolldrain</b>		
<b>MARCATURA</b>	FITT Rolldrain D. 160 300 N [linea n°] [lotto n°]				
<b>ASPETTO</b>	INTERNO	Sezione compatta, esente da bolle o cavità.			
	ESTERNO	Liscio, pulito, esente da rigature, cavità, grumi non fusi, difetti.			
<b>COLORE</b>	INTERNO	NERO			
	ESTERNO	VERDE			
<b>DIMENSIONI</b>	<b>PARAMETRO</b>	<b>U.M.</b>	<b>VALORE</b>		
	Ø ESTERNO	mm	160,0+2,9		
	Ø INTERNO	mm	min. 120		
	Lunghezza rotolo	m	min. 50		
	Tagli per passo	-	6		
	Area del taglio	cm <sup>2</sup>	0,4		
	Superficie di captazione	cm <sup>2</sup> /m	129,03		
					
			<p style="text-align: center;"><b>SCHIACCIAMENTO</b> &gt; 300 N</p>		
	<b>DATI TECNICI</b>	<b>PARAMETRO</b>	<b>U.M.</b>	<b>VALORE</b>	
Velocità		mm/min	15		
					



COMPANY WITH  
QUALITY SYSTEM  
CERTIFIED BY DNV GL  
= ISO 9001 =

## Scheda tecnica

MOD 01 PRO 13  
Rev. 00/2008  
Pagina 1

# GEODREN PPST 150



1213-CPR-3269

Geotessile nontessuto costituito da polipropilene da fiocco ad alta tenacità, stabilizzato ai raggi UV, agugliato e calandrato, con esclusione di collanti, leganti chimici o materiale riciclato post-consumatore.

Caratteristiche fisiche	Norme	Valore	U.M.	Tolleranza %	Tolleranza (unità)
Massa areica	[EN ISO 9864]	150	g/m <sup>2</sup>	+/- 10	+/- 15
Spessore	[EN ISO 9863-1] 2 kPa	1,00	mm	+/- 20	+/- 0,20
	[EN ISO 9863-1] 20 kPa	0,80	mm	+/- 20	+/- 0,16
	[EN ISO 9863-1] 200 kPa	0,60	mm	+/- 20	+/- 0,12

Caratteristiche meccaniche	Norme	Valore	U.M.	Tolleranza %	Tolleranza (unità)
Resistenza a trazione	[EN ISO 10319] MD	12,0	kN/m	- 10	- 1,2
	[EN ISO 10319] CMD	12,0	kN/m	- 10	- 1,2
Allungamento a rottura	[EN ISO 10319] MD	55	%	+/- 30	+/- 17
	[EN ISO 10319] CMD	60	%	+/- 30	+/- 18
Indice di energia	[EN ISO 10318]	3,50	kJ/m <sup>2</sup>	- 20	- 0,70
Resistenza al punzonamento statico CBR	[EN ISO 12236]	1,90	kN	- 10	- 0,19
Resistenza al punzonamento dinamico cone drop	[EN ISO 13433]	26	mm	+ 20	+ 5


Caratteristiche idrauliche	Norme	Valore	U.M.	Tolleranza %	Tolleranza (unità)
Indice di velocità	[EN ISO 11058]	100	mm/s	- 30	- 30
Capacità di flusso nel piano	[EN ISO 12958]	1,60	10-3 l/ms	- 30	- 0,48
Apertura caratteristica	[EN ISO 12956]	90	µm	+/- 30	+/- 27

Caratteristiche di durabilità					
Resistenza agli agenti atmosferici	[EN 12224]	Da coprire entro 30 giorni dall'installazione.			
Resistenza all'ossidazione	[-]	Previsione di durabilità di 25 anni in terreni naturali con 4<pH<9 e temperature del terreno <25°C in base ai risultati del metodo di prova EN ISO 13438 procedura A in accordo alla norma EN 13249:2016 e seguenti.			

I valori riportati corrispondono a valori guida ottenuti nel nostro laboratorio o presso laboratori esterni accreditati con un livello di confidenza del 95%. L'azienda si riserva la facoltà di apportare modifiche alla presente scheda tecnica senza alcun preavviso e non si assume alcuna responsabilità relativamente all'utilizzo delle informazioni in essa contenute e all'uso del prodotto.

MD = Machine Direction/Longitudinale; CMD = Cross Machine Direction/Trasversale; NA = Not Applicable/Non Applicabile

Ref.
Cod. 000058 Rev. 2 Data Rev.: 24-08-2011

Approved by CQ


Approved by UT


## A.2 Input files of GWS

```

8          ! nproc

.true.     ! solve_transport (T = solve transport equations)
.false.    ! solve_hw_variation (no gravitational term)

1 1        ! NL_scheme_FLOW,NL_scheme_TRAN (1 = Picard, 2 = Newton)
12         ! NL_itermax
2          ! NL_iconv
1.e-3     ! NL_tol

.false. .false. ! lump_massmat_FLOW,lump_massmat_TRAN (T = mass matrix for flow lumped)

1.0        ! theta
0.0        ! time0
12         ! ndeltat
1. 1. 1. 1. 1. 1.
1. 1. 1. 1. 1. 1.

.false.    ! expli
0.01       ! mintstep
0.5        ! redtsetp
2.0        ! amptsetp

0.0        ! cmw
1000.0     ! volwew

-2. 0. 0.5 !minhw,maxhw,tolhw

0.035     !epsilon_den
0.0       !epsilon_vis

```

*Param*

```

-99        ! iout
5000       ! itmax
1.d-6     ! tol
-1         ! isol
2          ! id_prec (1 = ICHOL, 2 = FSAI, 3 = ABF)
'./INPUT/prec/FSAI.lin' ! preconditioner parameters

```

---

```

-99        ! iout
5000       ! itmax
1.d-6     ! tol
-1         ! isol
1          ! id_prec_NSU (1 = NSYBFSAI)
'./INPUT/prec/NSYBFSAI.lin' ! preconditioner parameters

```

*Solver\_FLOW\_PIC (above) and solver\_TRAN (below)*

571619

1	4.031575000E+03	2.911300000E+02	-2.728000000E+00
2	4.030107000E+03	2.891700000E+02	-2.844000000E+00
3	4.032494000E+03	2.887100000E+02	-2.837000000E+00
4	4.033735000E+03	2.905800000E+02	-2.748000000E+00
5	4.032857000E+03	2.928300000E+02	-2.658000000E+00
6	4.028710000E+03	2.905500000E+02	-2.786000000E+00
7	4.029645000E+03	2.926900000E+02	-2.705000000E+00
8	4.028336000E+03	2.880900000E+02	-2.892000000E+00
9	4.030969000E+03	2.868000000E+02	-2.932000000E+00
10	4.033698000E+03	2.862500000E+02	-2.946000000E+00
11	4.034954000E+03	2.883600000E+02	-2.854000000E+00
12	4.034766000E+03	2.923000000E+02	-2.680000000E+00
13	4.035935000E+03	2.903300000E+02	-2.775000000E+00
14	4.033953000E+03	2.943000000E+02	-2.625000000E+00
15	4.031526000E+03	2.942100000E+02	-2.643000000E+00
16	4.026230000E+03	2.895000000E+02	-2.852000000E+00
17	4.026734000E+03	2.918300000E+02	-2.777000000E+00
18	4.027194000E+03	2.938600000E+02	-2.712000000E+00
19	4.029300000E+03	2.947200000E+02	-2.669000000E+00
20	4.026390000E+03	2.868900000E+02	-2.935000000E+00
21	4.029188000E+03	2.849700000E+02	-3.027000000E+00
22	4.032137000E+03	2.840700000E+02	-3.018000000E+00

*Coord*

3203288

1	1	11	11	1
26558	26860	26864	35208	
2	1	11	11	1
35208	35363	35367	26864	
3	1	11	11	1
26860	26864	35363	35208	
4	1	11	11	1
26860	27128	27129	35363	
5	1	11	11	1
35363	35544	35545	27129	
6	1	11	11	1
27128	27129	35544	35363	
7	1	11	11	1
27128	27129	27393	35544	
8	1	11	11	1
35544	35545	35752	27393	
9	1	11	11	1
27129	27393	35545	35544	
10	1	11	11	1
27128	27393	27394	35544	
11	1	11	11	1
35544	35752	35753	27394	

*Topol*



```

3                                     ! nmat

1                                     ! id_law
1                                     ! iparam
1.    1.    1.    0.                 ! rparam

1                                     ! id_law
1                                     ! iparam
1.    1.    1.    0.                 ! rparam

1                                     ! id_law
1                                     ! iparam
1.    1.    1.    0.                 ! rparam

-----

-----
id_law = 1 --> ele
-----

iparam(1) = itab
rparam(1) = fac_cms0
rparam(2) = ocr0
rparam(3) = cr
rparam(4) = tol
  
```

*Mat\_SOIL*

```

3                                     ! nmat

2                                     ! id_law
1.0  0.1  0.1  0.1  0.3  -0.5  3.0  0.1  0.5  0.8  ! rparam

2                                     ! id_law
1.0  10   10   10   0.3  -0.5  3.0  0.1  0.5  0.8  ! rparam

2                                     ! id_law
1.0  0.1  0.1  0.1  0.3  -0.5  3.0  0.1  0.5  0.8  ! rparam

-----

-----
id_law = 1 --> sat
-----

rparam( 1) : fac_k  --> multiplicative factor for k
rparam( 2) : kx    --> hydraulic conductivity in x direction
rparam( 3) : ky    --> hydraulic conductivity in y direction
rparam( 4) : kz    --> hydraulic conductivity in z direction
rparam( 5) : poros --> porosity

-----

id_law = 2 --> unsatvg
-----

rparam( 1) : fac_k  --> multiplicative factor for k
rparam( 2) : kx    --> hydraulic conductivity in x direction
rparam( 3) : ky    --> hydraulic conductivity in y direction
rparam( 4) : kz    --> hydraulic conductivity in z direction
rparam( 5) : poros --> porosity
rparam( 6) : vga   --> parameter a of Van Genuchten
rparam( 7) : vgn   --> parameter n of Van Genuchten
rparam( 8) : swr   --> residual saturation of water
rparam( 9) : swjmin --> minimum sw to compute jacobian terms
rparam(10) : swjmax --> maximum sw to compute jacobian terms
  
```

*Mat\_FLOW*

```

1                                ! nmat

1                                ! id_law
1.    1.    10.    1.    0.1    1.    ! rparam

```

```

-----
id_law = 1 --> tmat
-----

```

```

rparm( 1) : fac_aL --> multiplicative factor for aL
rparm( 2) : fac_aT --> multiplicative factor for aT
rparm( 3) : aL     --> longitudinal dispersivity
rparm( 4) : aT     --> transversal dispersivity
rparm( 5) : D0     --> molecular diffusivity
rparm( 6) : tau    --> tortuosity

```

*Mat\_TRAN*

```

1
'./INPUT/tab/depth_cms_sigeff.tab'
~
~
~

```

*Tablist\_SOIL*

-2.00000000	0.19095100
-2.00000000	0.19139370
-2.00000000	0.19402880
-2.00000000	0.19389310
-2.00000000	0.19332560
-2.00000000	0.19349140
-2.00000000	0.19281650
-2.00000000	0.19400890
-2.00000000	0.19593110
-2.00000000	0.19456540
-2.00000000	0.19108420
-2.00000000	0.18836010
-2.00000000	0.18708600
-2.00000000	0.19020480
-2.00000000	0.19042450
-2.00000000	0.19445890
-2.00000000	0.19278030
-2.00000000	0.19429760
-2.00000000	0.19626730
-2.00000000	0.19028350
-2.00000000	0.19129840
-2.00000000	0.19302770
-2.00000000	0.19266590
-2.00000000	0.19400860
-2.00000000	0.19591930
-2.00000000	0.19728750
-2.00000000	0.19560210
"ic_FLOW" [noeol] 571619L, 10289142C	"ic_TRAN" [noeol] 571619L, 10289141C

*Ic\_FLOW (to the left) and ic\_TRAN (to the right)*

```

0.00000000E+00 TIME
4371 NBC
439 440 441 442 443
444 445 446 447 456
557 558 685 686 839
840 1016 1017 1207 1208
1415 1416 1646 1895 2157
2433 2730 3040 3371 3719
4081 4460 4855 5257 5664
6072 6483 6891 7300 7712
8120 8532 8944 24552 24649
24650 24651 24652 24653 24654
24657 24763 24764 24765 24845
24846 24847 24848 24849 24850
24851 24854 24855 24960 24961
25051 25052 25053 25054 25055
25056 25057 25058 25061 25062
25063 25181 25182 25275 25276
25277 25278 25279 25280 25281
25282 25283 25285 25286 25287

1.0300000E+01 1.0300000E+01 1.0300000E+01 1.0300000E+01 8.1600000E+00
8.1600000E+00 8.1600000E+00 8.1600000E+00 8.1600000E+00 8.1600000E+00
8.1600000E+00 8.1600000E+00 8.1600000E+00 8.1600000E+00 8.1600000E+00
8.1600000E+00 8.1600000E+00 8.1600000E+00 8.1600000E+00 8.1600000E+00
8.1600000E+00 8.1600000E+00 8.1600000E+00 8.1600000E+00 8.1600000E+00
8.1600000E+00 8.1600000E+00 8.1600000E+00 8.1600000E+00 8.1600000E+00
8.1600000E+00 8.1600000E+00 8.1600000E+00 8.1600000E+00 8.1600000E+00
8.1600000E+00 8.1600000E+00 1.2360000E+01 1.2360000E+01 1.2360000E+01
1.2360000E+01 1.2360000E+01 1.2360000E+01 1.2360000E+01 1.2360000E+01
1.2360000E+01 1.2360000E+01 1.2360000E+01 1.2360000E+01 1.2360000E+01
1.2360000E+01 1.2360000E+01 1.2360000E+01 1.2360000E+01 1.2360000E+01
1.2360000E+01 1.2360000E+01 1.2360000E+01 1.2360000E+01 1.2360000E+01
1.2360000E+01 1.2360000E+01 1.2360000E+01 1.2360000E+01 1.2360000E+01
1.2360000E+01 1.2360000E+01 1.2360000E+01 1.2360000E+01 1.2360000E+01
0.10000000E+21 TIME
0 NBC

```

Start (above) and end (below) of bcdir\_FLOW

```

0.00000000E+00 TIME
0 NBC
1.20000001E+02 TIME
6679 NBC
254236 254243 254244 254646 254649
254650 254651 254652 255057 255058
255059 255060 255061 255062 255071
255072 255073 255466 255467 255468
255469 255478 255479 255480 255481
255482 255538 255885 255886 255887
255888 255894 255895 255896 255897
256296 256297 256298 256299 256300
256301 256302 256303 256304 256305
256316 256317 256318 256707 256708
256709 256710 256711 256712 256713
256714 256727 256728 256729 256730
256731 256732 256733 256734 256793
257124 257125 257126 257127 257143
257144 257145 257146 257147 257148
257149 257150 257151 257152 257153
257154 257535 257554 257555 257556
257557 257558 257559 257560 257561
257562 257935 257936 257937 257958
257959 257960 257961 258025 258026
258027 258028 258326 258327 258328
258329 258330 258331 258332 258333
258334 258414 258415 258416 258417
258418 258419 258420 258704 258705
258706 258707 258708 258709 258710
258711 258712 258713 258714 258715
258787 258788 258789 258790 258791
258792 258795 258796 258797 258798
258799 259067 259068 259069 259070
259071 259072 259073 259074 259075
259076 259077 259078 259090 259091
259092 259093 259153 259154 259155
"bcneu_FLOW" 2678L, 203528C 1,75 Top

```

Bcneu\_FLOW

3003				
5981	6396	6813	7234	7657
8073	8493	8529	8531	8909
8943	9331	9356	9721	9750
9770	10137	10149	10167	10547
10563	10583	10959	10967	11000
11371	11380	11414	11789	11799
11831	11835	11836	12202	12250
12251	12253	12617	12667	12668
12673	13036	13086	13094	13445
13446	13497	13507	13835	13849
13902	13913	14223	14294	14306
14566	14567	14599	14673	14687
14688	14930	14931	14960	15036
15052	15053	15289	15297	15310
15385	15402	15403	15623	15624
15625	15626	15636	15723	15741
15742	15957	15958	15967	16002
16048	16061	16062	16069	16070
16278	16320	16370	16380	16383
16384	16387	16396	16397	16557
16591	16636	16691	16699	16700
16701	16702	16704	16705	16712
16713	16714	16716	16722	16723
16874	16890	16904	16950	16952
17010	17018	17019	17035	17041
17044	17050	17051	17194	17203

*Bcspg\_FLOW*

0.00000000E+00	TIME				
22335	NBC				
1	2	3	4	5	
6	7	8	9	10	
11	12	13	14	15	
16	17	18	19	20	
21	22	23	24	25	
26	27	28	29	30	
31	32	33	34	35	
36	37	38	39	40	
41	42	43	44	45	
46	47	48	49	50	
51	52	53	54	55	
56	57	58	59	60	
61	62	63	64	65	
66	67	68	69	70	
71	72	73	74	75	
76	77	78	79	80	
81	82	83	84	85	
86	87	88	89	90	
91	92	93	94	95	
96	97	98	99	100	
101	102	103	104	105	

3.0541119E-05	3.0995913E-05	2.2809633E-05	8.9909137E-06	1.0495230E-05
1.7806907E-05	8.0463430E-06	1.0355294E-05	1.0810087E-05	1.6372559E-05
1.7107225E-05	1.5882781E-05	1.6162654E-05	1.6967289E-05	1.8961382E-05
9.0258978E-06	2.3439347E-05	1.0530214E-05	8.0463430E-06	1.0355294E-05
1.0810087E-05	1.6547479E-05	1.6267606E-05	1.7492050E-05	2.5363472E-05
1.8611541E-05	1.7422082E-05	1.8191732E-05	1.8506589E-05	3.0436167E-05
2.8651978E-05	4.0931397E-05	2.8896867E-05	2.9771469E-05	3.6383464E-05
3.6033623E-05	2.6028170E-05	3.2920038E-05	2.2634713E-05	3.1065881E-05
2.8686962E-05	2.9771469E-05	3.0506135E-05	3.1065881E-05	2.7952296E-05
2.7567471E-05	3.0786008E-05	3.6033623E-05	3.3864609E-05	3.4109497E-05
2.6203091E-05	3.3269879E-05	3.0925944E-05	2.1200365E-05	3.1240801E-05
3.4249434E-05	2.5328488E-05	2.4348934E-05	1.7492050E-05	1.7806907E-05
2.5888234E-05	1.6617448E-05	2.4698775E-05	1.6477511E-05	1.6302591E-05
1.6652432E-05	1.7212177E-05	2.4488870E-05	2.1375285E-05	2.5503409E-05
2.0815539E-05	2.3684236E-05	2.6308043E-05	2.8826898E-05	1.8156748E-05
2.1445253E-05	1.7352114E-05	1.6442527E-05	1.6617448E-05	2.3194458E-05
2.5783282E-05	2.3369379E-05	2.5853250E-05	1.8996366E-05	2.5363472E-05
2.3894140E-05	2.5433441E-05	2.5643345E-05	2.5958202E-05	2.6273059E-05
0.10000000E+21	TIME			
0	NBC			

*Start (above) and end (below) of bcatm\_FLOW*

```

5.000000E-01 5.000000E-01 5.000000E-01 5.000000E-01 5.000000E-01
5.000000E-01 5.000000E-01 5.000000E-01 5.000000E-01 5.000000E-01
5.000000E-01 5.000000E-01 5.000000E-01 5.000000E-01 5.000000E-01
5.000000E-01 5.000000E-01 5.000000E-01 5.000000E-01 5.000000E-01
5.000000E-01 5.000000E-01 5.000000E-01 5.000000E-01 5.000000E-01
5.000000E-01 5.000000E-01 5.000000E-01 5.000000E-01 5.000000E-01
5.000000E-01 5.000000E-01 5.000000E-01 5.000000E-01 5.000000E-01
5.000000E-01 5.000000E-01 5.000000E-01 5.000000E-01 5.000000E-01
5.000000E-01 5.000000E-01 5.000000E-01 5.000000E-01 5.000000E-01
5.000000E-01 5.000000E-01 5.000000E-01 5.000000E-01 5.000000E-01
1.000000E+00 1.000000E+00 1.000000E+00 1.000000E+00 1.000000E+00
1.000000E+00 1.000000E+00 1.000000E+00 1.000000E+00 1.000000E+00
1.000000E+00 1.000000E+00 1.000000E+00 1.000000E+00 1.000000E+00
1.000000E+00 1.000000E+00 1.000000E+00 1.000000E+00 1.000000E+00
1.000000E+00 1.000000E+00 1.000000E+00 1.000000E+00 1.000000E+00
1.000000E+00 1.000000E+00 1.000000E+00 1.000000E+00 1.000000E+00
1.000000E+00 1.000000E+00 1.000000E+00 1.000000E+00 1.000000E+00
1.000000E+00 1.000000E+00 1.000000E+00 1.000000E+00 1.000000E+00
1.000000E+00 1.000000E+00 1.000000E+00 1.000000E+00 1.000000E+00
1.000000E+00 1.000000E+00 1.000000E+00 1.000000E+00 1.000000E+00
1.000000E+00 1.000000E+00 1.000000E+00 1.000000E+00 1.000000E+00
1.800000E+01 TIME
32677 NBC
1 2 3 4 5
6 7 8 9 10
11 12 13 14 15
16 17 18 19 20
21 22 23 24 25
26 27 28 29 30
31 32 33 34 35
36 37 38 39 40
41 42 43 44 45
46 47 48 49 50
51 52 53 54 55
56 57 58 59 60
61 62 63 64 65
66 67 68 69 70
71 72 73 74 75
76 77 78 79 80
81 82 83 84 85
54123,75 3%

```

*Bcdir\_TRAN*

```

34 .true. .false. .true.

1. 48. 76. 122. 150.
162. 179. 198. 245. 262.
293. 300. 350. 364. 365.
400. 413. 441. 450. 487.
500. 515. 527. 544. 550.
563. 600. 610. 627. 650.
658. 700. 729. 730.
~
~

```

*Print\_time\_FLOW and print\_time\_TRAN*

```

10
126407
130735
132160
137137
152659
266350
288626
292004
293041
298812
~
~

```

*Format example for print\_list\_nod\_FLOW, print\_list\_nod\_TRAN and print\_list\_ele\_FLOW*

# Bibliography

---

Abarca, E., Vázquez-Suñé, E., Carrera, J., Capino, B., Gámez, D. and Batlle, F., 2006. Optimal design of measures to correct seawater intrusion. *Water Resources Research*, 42 (9), 1-14.

Abdoulhalik, A., Ahmed, A. and Hamill, G., 2017. A new physical barrier system for seawater intrusion control. *Journal of Hydrology*, 549, 416-427.

Barlow, P. M., 2003. *Groundwater in Freshwater-Saltwater Environments of the Atlantic Coast*. USGS Circular 1262, United States Geological Survey, Reston, VA.

Barlow, P. and Reichard, E., 2009. Saltwater intrusion in coastal regions of North America. *Hydrogeology Journal*, 18(1), 247-260.

Bear, J., 1979. *Hydraulics of groundwater*. New York: McGraw-Hill International Book Co.

Bevington, J., Piragnolo, D., Teatini, P., Vellidis, G. and Morari, F., 2016. On the spatial variability of soil hydraulic properties in a Holocene coastal farmland. *Geoderma*, 262, 294-305.

Chang, Q., Zheng, T., Zheng, X., Zhang, B., Sun, Q. and Walther, M., 2019. Effect of subsurface dams on saltwater intrusion and fresh groundwater discharge. *Journal of Hydrology*, 576, 508-519.

Cunico, I., 2019. Development of numerical experiments to simulate lab tests and predict field activities in the Most project. Master thesis. University of Padova.

Custodio, E. and Bruggeman, G., 1987. *Groundwater Problems In Coastal Areas*. Paris: Unesco.

Elsayed, S. and Oumeraci, H., 2018. Modelling and mitigation of storm-induced saltwater intrusion: Improvement of the resilience of coastal aquifers against marine floods by subsurface drainage. *Environmental Modelling & Software*, 100, 252-277.

Gambolati, G. and Putti, M., 2000. Saltwater contamination of a coastal Italian aquifer by a coupled finite element model of flow and transport.

Gambolati, G., Putti, M. and Paniconi, C., 1999. Three-dimensional model of coupled density-dependent flow and miscible salt transport. In: *Seawater Intrusion in Coastal Aquifers: Concepts, Methods, and Practices*, J. Bear et al. eds., Kluwer Academic, Dordrecht, Holland.

Gambolati, G., Putti, M., Teatini, P. and Gasparetto Stori, G., 2006. Subsidence due to peat oxidation and impact on drainage infrastructures in a farmland catchment south of the Venice Lagoon. *Environmental Geology*, 49 (6), 814-820.

Hu, L. and Jiao, J., 2010. Modeling the influences of land reclamation on groundwater systems: A case study in Shekou peninsula, Shenzhen, China. *Engineering Geology*, 114(3-4), 144-153.

Hussain, M., Abd-Elhamid, H., Javadi, A. and Sherif, M., 2019. Management of Seawater Intrusion in Coastal Aquifers: A Review. *Water*, 11 (12), 2467.

Manoli, G., Bonetti, S., Scudiero, E., Morari, F., Putti, M. and Teatini, P., 2015. Modeling Soil-Plant Dynamics: Assessing Simulation Accuracy by Comparison with Spatially Distributed Crop Yield Measurements. *Vadose Zone Journal*, 14 (12).

Oiro, S. and Comte, J., 2019. Drivers, patterns and velocity of saltwater intrusion in a stressed aquifer of the East African coast: Joint analysis of groundwater and geophysical data in southern Kenya. *Journal of African Earth Sciences*, 149, 334-347.

Paniconi, C., Ferraris, S., Putti, M., Pini, G. and Gambolati, G., 1994. Three-dimensional numerical codes for simulating groundwater contamination: FLOW3D, flow in saturated and unsaturated porous media. *Pollution Modeling*, 1, 149– 156.

Prusty, P. and Farooq, S., 2020. Seawater intrusion in the coastal aquifers of India - A review. *HydroResearch*, 3, 61-74.

Rizzetto, F., Tosi, L., Carbognin, L., Bonardi, M. and Teatini, P., 2003. Geomorphological setting and related hydrogeological implications of the coastal plain south of the Venice Lagoon (Italy). In: *Hydrology of the Mediterranean and Semiarid Regions*, E. Servat et al. eds., IAHS Publ. n. 278, 463-470.

Rorai, C., 2007. Simulazione numerica dell'intrusione salina negli acquiferi superficiali confinanti col margine meridionale della Laguna di Venezia. Master thesis. University of Padova.

Scudiero, E., Teatini, P., Corwin, D., Deiana, R., Berti, A. and Morari, F., 2013. Delineation of site-specific management units in a saline region at the Venice Lagoon margin, Italy, using soil

reflectance and apparent electrical conductivity. *Computers and Electronics in Agriculture*, 99, 54-64.

Talon, L., 2019. Ricarica di un acquifero salino con acqua dolce: modellazione numerica. Bachelor thesis. University of Padova.

Teatini, P., Tosi, L., Viezzoli, A., Baradello, L., Zecchin, M. and Silvestri, S., 2011. Understanding the hydrogeology of the Venice Lagoon subsurface with airborne electromagnetics. *Journal of Hydrology*, 411 (3-4), 342-354.

van Genuchten, M., 1980. A Closed-form Equation for Predicting the Hydraulic Conductivity of Unsaturated Soils. *Soil Science Society of America Journal*, 44 (5), 892-898.

Vandenbohede, A., Van Houtte, E. and Lebbe, L., 2009. Sustainable groundwater extraction in coastal areas: a Belgian example. *Environmental Geology*, 57(4), 735-747.

White, E. and Kaplan, D., 2017. Restore or retreat? saltwater intrusion and water management in coastal wetlands. *Ecosystem Health and Sustainability*, 3 (1).

Wu, H., Lu, C., Kong, J. and Werner, A., 2020. Preventing Seawater Intrusion and Enhancing Safe Extraction Using Finite-Length, Impermeable Subsurface Barriers: 3D Analysis. *Water Resources Research*, 56 (11).